

AFRL-AFOSR-UK-TR-2015-0010



**Novel Routes for Sintering of Ultra-high Temperature
Ceramics and their Properties**

***Elena Andrievskaya**

**SCIENCE AND TECHNOLOGY CENTER IN UKRAINE
METALISTIV 7A, KYIV, UKRAINE**

***FRANTSEVICH INSTITUTE FOR PROBLEMS IN MATERIALS
SCIENCE, NAS OF UKRAINE
3, KRZHYZHONOVSKY STR, KIEVE 03680 UKRAINE**

EOARD GRANT #STCU 11-8004/STCU P-513

Report Date: October 2014

Final Report from 1 November 2011 to 31 October 2014

Distribution Statement A: Approved for public release distribution is unlimited.

**Air Force Research Laboratory
Air Force Office of Scientific Research
European Office of Aerospace Research and Development
Unit 4515, APO AE 09421-4515**

REPORT DOCUMENTATION PAGE				Form Approved OMB No. 0704-0188	
Public reporting burden for this collection of information is estimated to average 1 hour per response, including the time for reviewing instructions, searching existing data sources, gathering and maintaining the data needed, and completing and reviewing the collection of information. Send comments regarding this burden estimate or any other aspect of this collection of information, including suggestions for reducing the burden, to Department of Defense, Washington Headquarters Services, Directorate for Information Operations and Reports (0704-0188), 1215 Jefferson Davis Highway, Suite 1204, Arlington, VA 22202-4302. Respondents should be aware that notwithstanding any other provision of law, no person shall be subject to any penalty for failing to comply with a collection of information if it does not display a currently valid OMB control number. PLEASE DO NOT RETURN YOUR FORM TO THE ABOVE ADDRESS.					
1. REPORT DATE (DD-MM-YYYY) 31 Oct 2014		2. REPORT TYPE Final Report		3. DATES COVERED (From – To) 1 November 2011 – 31 October 2014	
4. TITLE AND SUBTITLE Novel Routes for Sintering of Ultra-high Temperature Ceramics and their Properties				5a. CONTRACT NUMBER STCU P-513	
				5b. GRANT NUMBER STCU 11-8004	
				5c. PROGRAM ELEMENT NUMBER 61102F	
6. AUTHOR(S) *Elena Andrievskaya				5d. PROJECT NUMBER	
				5d. TASK NUMBER	
				5e. WORK UNIT NUMBER	
7. PERFORMING ORGANIZATION NAME(S) AND ADDRESS(ES) SCIENCE AND TECHNOLOGY CENTER IN UKRAINE METALISTIV 7A, KYIV, UKRAINE *FRANTSEVICH INSTITUTE FOR PROBLEMS IN MATERIALS SCIENCE NAS OF UKRAINE 3, KRZHYZHONOVSKY STR, KIEVE 03680 UKRAINE				8. PERFORMING ORGANIZATION REPORT NUMBER N/A	
9. SPONSORING/MONITORING AGENCY NAME(S) AND ADDRESS(ES) EOARD Unit 4515 APO AE 09421-4515				10. SPONSOR/MONITOR'S ACRONYM(S) AFRL/AFOSR/IOE (EOARD)	
				11. SPONSOR/MONITOR'S REPORT NUMBER(S) AFRL-AFOSR-UK-TR-2015-0010	
12. DISTRIBUTION/AVAILABILITY STATEMENT Distribution A: Approved for public release; distribution is unlimited.					
13. SUPPLEMENTARY NOTES					
14. ABSTRACT The project has been focused on phase equilibria research, development of phase diagrams of the ternary systems ZrO_2 - CeO_2 - Ln_2O_3 ($Ln=La_2O_3, Eu_2O_3, Gd_2O_3$) and some of boundary binary systems, as well as manufacturing and characterization of dense, optically transparent ceramics based on $LaYO_3$ and $Y_3Al_5O_{12}$ phases. First developed phase diagrams of the ternary systems ZrO_2 - CeO_2 - Ln_2O_3 ($Ln = La, Eu, Gd$) and binary systems ZrO_2 - Gd_2O_3 , CeO_2 - Gd_2O_3 , CeO_2 - Eu_2O_3 have been presented as a collection of isothermal and polythermal sections in the temperature range from 600 to 1500 °C. The solubility of components, extension of one, two and three phase fields and mechanisms of phase reactions have been determined. Lattice parameters for solid solutions were calculated. The results have been summarized along the rows of the systems ZrO_2 - Ln_2O_3 , CeO_2 - Ln_2O_3 and ZrO_2 - CeO_2 - Ln_2O_3 . The pyrochlore-type or defect fluorite-type phases of the formulae $Zr(Ce)_2Gd_2O_7$ when doped with scintillator Eu^{2+} represent a subject of interest for future ceramic laser matrices. The nanosize powders of doped $Nd(Yb):LaYO_3$ and $Nd:Y_3Al_5O_{12}$ phases containing various amount of dopants have been chemically prepared. Particle size distribution was narrow in the particle size range of 10-22 nm. Coarsening of particles to 300 nm and faceting of particles were carried out to allow manipulation in strong magnetic field using EPD or SC techniques. The neodymia doped garnet samples showed residual porosity less than 0.2% with good transparency of 70-72% after RCS. Neodymium dopant led to instability of the $LaYO_3$ phase. The rare earth ions such as Er^{3+} and Yb^{3+} may be used as laser dopants. The $Yb:LaYO_3$ ceramics textured under strong magnetic field has shown density of 99.0-99.2. The samples were found semi-transparent (average transparency is less than 45%), but more transparent along c-axis.					
15. SUBJECT TERMS EOARD, Materials, microstructural characterization, high temperature					
16. SECURITY CLASSIFICATION OF:			17. LIMITATION OF ABSTRACT SAR	18, NUMBER OF PAGES 62	19a. NAME OF RESPONSIBLE PERSON Matthew Snyder
a. REPORT UNCLAS	b. ABSTRACT UNCLAS	c. THIS PAGE UNCLAS			19b. TELEPHONE NUMBER (Include area code) +44 (0)1895 616420

FINAL REPORT
by EOARD 118004 (STCU P513) project

Project title: “Phase equilibria in advanced ternary oxide systems and study of optically transparent ceramic nanomaterials”

Reporting period: November 1, 2011 – October 31, 2014

Frantsevich Institute for Problems in Materials Science NAS of Ukraine

Project Manager: Prof. Elena Andrievskaya

Main goal of the project:

The proposal is aimed at study of phase equilibria, development of phase diagrams of the ternary systems $\text{ZrO}_2\text{--CeO}_2\text{--Ln}_2\text{O}_3(\text{La}_2\text{O}_3, \text{Eu}_2\text{O}_3, \text{Gd}_2\text{O}_3)$, as well as manufacturing and studying optically transparent ceramics based on lanthana-yttria perovskite (LaYO_3) yttria-alumina garnet ($\text{Y}_3\text{Al}_5\text{O}_{12}$). The sub-targets are: Study of phase equilibria and development of phase diagrams in the ternary systems $\text{ZrO}_2\text{--CeO}_2\text{--Ln}_2\text{O}_3(\text{La}_2\text{O}_3, \text{Eu}_2\text{O}_3, \text{Gd}_2\text{O}_3)$, to determine temperature intervals of phase stability, concentration dependences of lattice parameters, solubility of components, especially luminescent-active ions; synthesis of nanosize powders for various solid solutions based on LaYO_3 and $\text{Y}_3\text{Al}_5\text{O}_{12}$ in the particle size range 10-15 nm, valid for manufacturing dense nanocrystalline ceramics; study of rate controlled sintering of these powders until 99.9% of theoretical density controlling both pore-and-grain size evolution under gas atmosphere with definite oxygen partial pressure; study of optical properties for ceramics.

1. Phase equilibria in the $\text{ZrO}_2\text{--CeO}_2\text{--Ln}_2\text{O}_3(\text{La}_2\text{O}_3, \text{Eu}_2\text{O}_3, \text{Gd}_2\text{O}_3)$ systems

The phase equilibria research in the ternary $\text{ZrO}_2\text{--CeO}_2\text{--Ln}_2\text{O}_3$ systems represents basic knowledge and practical interests. The systems including zirconia, ceria, europia, dysprosia and ytterbia are of practical interest to create novel alternative oxide materials of structural and functional applications with advanced characteristics [1-16, 24-27].

For instance, doped zirconia, ceria and lanthanide oxides are widely used for thermal barrier coatings, ionic conductors in solid oxide fuel cells, catalysts etc. [17-23, 27]. Substantial potential these systems demonstrate in the nuclear energy engineering for both nuclear fuel and inert matrices to safely store nuclear wastes [26]. At present the search of ceramics matrix immobilizing plutonium is a hot topic for these materials. The inert matrix material should meet the following requirements: high cross section of neutron catching, good enough thermal stability, low thermal conductivity and low thermal expansion coefficient, lack of phase transitions. The high temperature structural ceramics with low thermal expansion is valuable in neutron reactor components. To immobilize the transuranic elements, the ceramic matrix appears to be the best choice because of high thermodynamic stability for a long life time of exploration.

The lattice of the pyrochlore-type phase ($\text{A}_2\text{B}_2\text{O}_7$), containing Zr^{4+} ions as the main cation of the compound $\text{M}_2\text{Zr}_2\text{O}_7$ (M = three and/or four charged cation) is reliable and substantiated matrix for concentrated nuclear wastes. The ordered pyrochlore phase $\text{Eu}_2\text{Zr}_2\text{O}_7$ is also perspective thermal isolator [3, 15, 24]. These properties of REO zirconates are attractive for thermal barrier coatings in gas turbines [15, 22]. Chemical composition corresponding to europium zirconate ($\text{Eu}_2\text{Zr}_2\text{O}_7$) exists as a disordered phase of fluorite type (disordered cations and vacancies) at high temperatures, meanwhile at low temperatures the ordering results in pyrochlore-type phase (where cations and vacancies are ordered). The pyrochlore type phase $\text{Eu}_2\text{Zr}_2\text{O}_7$ transforms to the defect fluorite by

ordering/disordering mechanism at relatively high temperature ~ 2100 °C. Because of similarity of physic-chemical properties of plutonia and ceria, CeO_2 is often used as a surrogate material instead of PuO_2 .

Materials based on ceria, zirconia doped with REO are perspective for bio-medical applications, energy conversion and machine-building, optical systems and catalysts because of uniqueness of its properties. Phase diagrams of the given systems are considered physicochemical background for such materials like solid electrolytes in fuel cells, catalyst's carriers, refractory ceramics, barrier coatings etc. Solid solutions based on ceria represent the most prospective electrolyte materials operating at moderate temperatures, because their ionic conductivity and sensitivity to oxygen partial pressure is much higher than that for yttria stabilized ZrO_2 (YSZ). Thermal barrier coatings with double ceramic layer: CeO_2 and 8YSZ, 8YSZ and $\text{Ln}_2\text{Zr}_2\text{O}_7$ - the pyrochlore type phase - demonstrate high melting temperature, lack of phase transitions at room and elevated operation temperatures, low thermal conductivity, chemical inertness, thermal expansion corresponding to that of metal substrate, good adhesion to substrate and low sintering rate, porous microstructure. Additions of low-valence dopants, such as Ln^{3+} and Y^{3+} , solid solutions of the system CeO_2 - ZrO_2 allow suppression of undesirable segregation of ions in the phase based on ceria zirconia in so called ceramic carriers of catalysts, which sustainably operate at moderate temperatures for a long time [8-12].

Methodology

In accordance with the plan, the samples for phase equilibria in the ternary ZrO_2 - CeO_2 - Ln_2O_3 system and binary CeO_2 - Ln_2O_3 , ZrO_2 - Ln_2O_3 systems in the full range of concentrations. As input components the zirconyl-nitrate $\text{ZrO}(\text{NO}_3)_2$ and cerium nitrate $\text{Ce}(\text{NO}_3)_3 \cdot 6\text{H}_2\text{O}$ of "pure" grade, nitric acid "pure for analysis", La_2O_3 , Eu_2O_3 and Gd_2O_3 with content of the main component not less than 99.99 %.

Samples were prepared with the concentration step of 1-5 mol. % from nitrate solutions followed by evaporation and thermal decomposition of nitrates until oxides followed by firing at 1200 °C for 2 hours. The powders were pressed into tablets of 5 mm in diameter and 4 mm in height under pressure of 10 MPa. For studying the systems ZrO_2 - CeO_2 - Ln_2O_3 the samples of the compositions along the sections: ZrO_2 - (50 mol. % CeO_2 - 50 mol. % Ln_2O_3), ZrO_2 - (90 mol. % CeO_2 - 10 mol. % Ln_2O_3), ZrO_2 - (10 mol. % CeO_2 - 90 mol. % Ln_2O_3), CeO_2 - (69 mol. % ZrO_2 - 31 mol. % Ln_2O_3) and some iso-concentrates were taken for consideration.

Accordingly to the plan, the annealing of samples for the phase diagram research in the ternary ZrO_2 - CeO_2 - Ln_2O_3 system has been carried out at 1100 °C and in the binary CeO_2 - Ln_2O_3 , ZrO_2 - Ln_2O_3 systems at 1100 and 1500 °C.

Phase equilibria in the systems ZrO_2 - CeO_2 - Ln_2O_3 , were studied at 1100 °C using thermal treatment in the H23U5T furnace in air. The samples were heated from room temperature to given one with the rate of 3.5 degr/min. The annealing regime is non-stop. The periodical control of the homogenization completeness was provided. Then samples were grinded again pressed and placed into furnace for annealing. The period was not less than 150 hours. Cooling down was quite slow. Total duration of this unique experiment in the ZrO_2 - CeO_2 - Ln_2O_3 systems and boundary binary systems at 1100 °C was about **13000 hours**.

To study the phase equilibria in the ZrO_2 - Gd_2O_3 system at melting temperatures, the samples with concentration step of 1-10 mol. % were prepared by traditional ceramic method, mechanical mixing of input oxides. The powders were mixed in agate mortar. Powders were consolidated into discs of 20 mm in diameter and of 15 mm in height using steel mold under pressure of 10 MPa. Melting was carried out in the optical furnace. Crystallization in the radial - symmetrical temperature field optical furnace have own specific features. The heat source in the optical furnace is concentrated luminous flux. The power density flux of light energy in the focal zone has Gauss distribution. When placing the material in the focal zone the relatively flat shallow melt pool is

formed. Its size gradually increases, until energy losses such as heat conductivity through the pool bottom, light irradiation from the pool surface would become equal to falling energy. After reaching equilibrium, the size of bath is stabilized. With decreasing power density of the falling energy flow, the process of crystallization has begun. The melt crystallizes in the direction from the boundary to the center of the melt pool in the center. The last drop of melt solidifies in the center of the focal zone. The shape of received ingot surface depends on the ratio of the density of the melt and the solid phase properties at crystallization temperature.

Due to features of bulk alloys melting, samples for phase equilibria study were prepared by the method of sequential deposition of layers in the focal zone optical furnace. Thus there is a consistent increase of ingot thickness and texture formation under high (several hundred degrees per millimeter), recurrent temperature gradients in the direction from the bottom surface of the melt pool to its upper surface. The samples melted, cooled followed by annealed at 1500 °C were studied by XRD, petrography and electron microscopy methods. Phase composition of the samples has been determined with the aid of XRD and LRSA methods. The XRD used the powder method of sampling at room temperature ($\text{CuK}\alpha$ irradiation). The recording scanning rate was 1-4 deg/min in the diapason of 2θ angles from 15 to 80°. The periods of crystalline lattices were calculated by the less square method of using LATTIC code with an accuracy below 0.0004 nm for cubic phase.

The crystal-optic characteristics of the phases obtained were determined under polarized microscope “MIH-8”. The refraction indexes were measured in immersion liquids (solution of arsenic tribromide in methylene iodide or alloys of sulfur with selenium) with accuracy ± 0.02 .

Microstructures were studied on polished surfaces of the samples annealed and melted using local x-ray spectral analysis, on the microscope SUPERPROBE-733 (JEOL, Japan, Palo Alto, CA) in both back scattered electrons (BEI) and secondary electrons (SEI). The composition of the sample has been controlled with the aid of spectral and chemical analysis.

1.1. Phase equilibria in the ZrO_2 — CeO_2 — La_2O_3 systems

Isothermal section of the phase diagram of the ZrO_2 - CeO_2 - La_2O_3 system at 1100 °C

The phase diagram of the ZrO_2 - CeO_2 - La_2O_3 system at high temperatures has been previously studied in our recent work. Present research is focused on phase equilibria in this system at low temperatures, in particular, at 1100 °C. The isothermal section of the ternary phase diagram of the system ZrO_2 - CeO_2 - La_2O_3 at 1100 °C has been developed and presented here in Fig. 1.1. The chemical and phase composition of the samples annealed at 1100 °C, lattice parameters for the equilibrium phases at given temperature are presented in the Fig. 1.2.

In the ZrO_2 - CeO_2 - La_2O_3 system at 1100 °C there had been find five fields of solid solutions based on monoclinic (M) and tetragonal (T) ZrO_2 , hexagonal (A) La_2O_3 , cubic form of fluorite type (F) CeO_2 and an ordered phase of pyrochlore type $\text{La}_2\text{Zr}_2\text{O}_7$ (Py). New phases were not found in this system. To determine boundaries of the phase fields the concentration dependence of lattice parameters for elementary cells of the phases (Fig. 1.2). These results were confirmed by microscopy and XRD data (Figs 1.3-1.7 and Tables 1.1, 1.2).

Using parameters of elementary cells of the pyrochlore phase in the three-phase samples, as well as XRD data in combination with SEM gave coordinates for configurative points of the tie-line triangles (Py+T+F), (Py+T+M) i (Py+F+A) (Table. 1.1). In the field with high concentration of ZrO_2 the solid solutions based on monoclinic and tetragonal ZrO_2 were found. No substantial solubility of CeO_2 and La_2O_3 in the M- ZrO_2 was determined. The boundary of the homogeneity field of the solid solution based on M- ZrO_2 at 1100 °C passes close to the composition of 99 mol % ZrO_2 -0.5 mol % CeO_2 -0.5 mol % La_2O_3 . The narrow field of the solid solutions based on T- ZrO_2 is prolated along the boundary binary system ZrO_2 - CeO_2 (2-18 mol % CeO_2). The solubility of La_2O_3 in T- ZrO_2 is not high achieving ~ 1 mol %, confirmed by XRD.

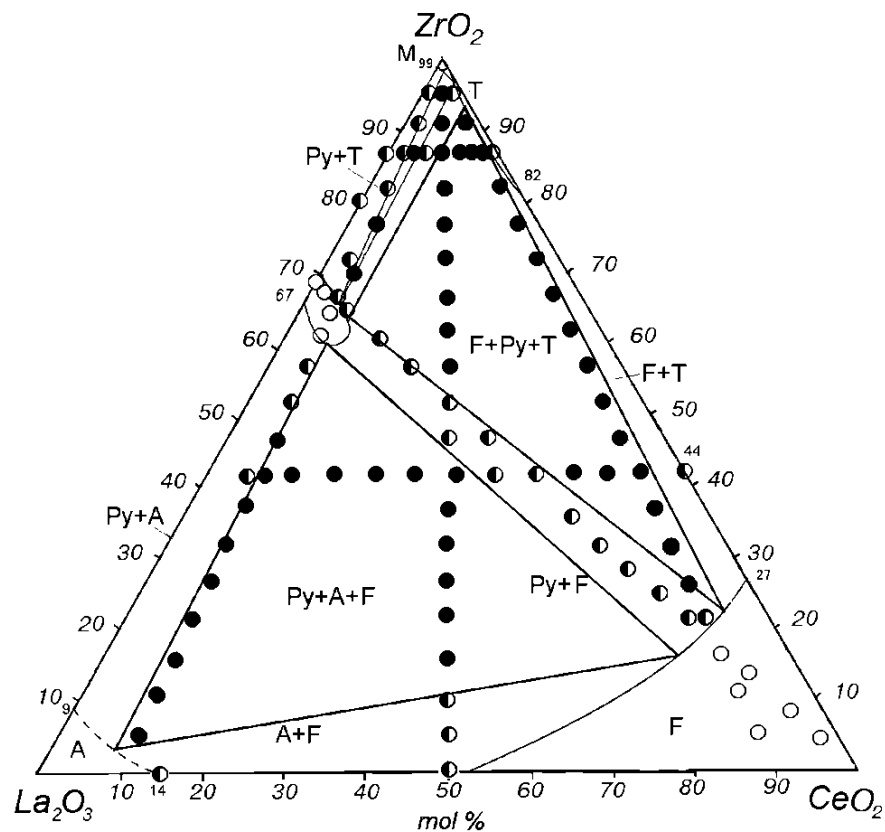


Fig. 1.1 - Isothermal cross section of the ternary diagram of the $\text{ZrO}_2\text{-CeO}_2\text{-La}_2\text{O}_3$ system at temperature 1100 °C (○ – one-phase, ◐ - two-phase, ● – three-phase).

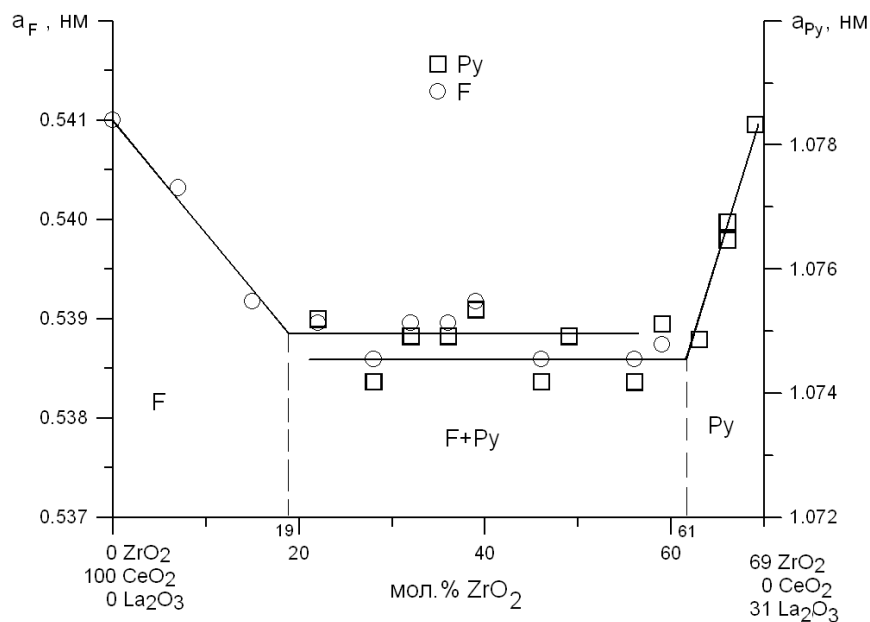


Fig. 1.2 - Concentration dependences of the lattice parameters of the solid solutions F (○) and Py (□) by the cross section CeO_2 - (69 mol. % ZrO_2 - 31 mol. % La_2O_3) in the system $\text{ZrO}_2\text{-CeO}_2\text{-La}_2\text{O}_3$ after annealing at 1100 °C.

Table 1.1 Coordinates of the tie-line triangle in the $\text{ZrO}_2\text{-CeO}_2\text{-La}_2\text{O}_3$ system corresponding to three-phase equilibrium in this system at 1100 °C

Phase field	Coordinates of the tie-line triangle, mol %									
	M		T		Py		F		A	
	ZrO ₂	CeO ₂	ZrO ₂	CeO ₂	ZrO ₂	CeO ₂	ZrO ₂	CeO ₂	ZrO ₂	CeO ₂
Py+T+M	99.0	0.5	96.5	3.0	66.0	4.0	-	-	-	-
F+Py+T	-	-	93.0	6.0	64.0	7.0	24.0	73.0	-	-
Py+A+F	-	-	-	-	60.0	6.0	16.0	70.0	3.0	8.0

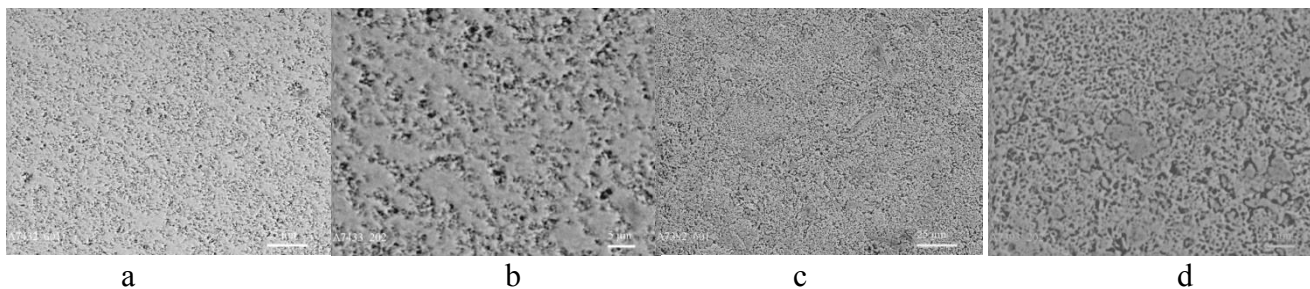


Fig 1.3-Microstructure of the F phase in the system $\text{ZrO}_2\text{-CeO}_2\text{-La}_2\text{O}_3$ after annealing at 1100 °C:

- a) 3 mol% ZrO_2 – 95% mol CeO_2 – 2mol % La_2O_3 , <F>, BEI, $\times 600$;
- b) 3 mol% ZrO_2 – 95% mol CeO_2 – 2mol % La_2O_3 , <F>, BEI, $\times 2000$;
- c) 11 mol % ZrO_2 – 80.5 mol % CeO_2 – 8.5mol % La_2O_3 , <F>, BEI, $\times 600$;
- d) 11 mol % ZrO_2 – 80.5 mol % CeO_2 – 8.5mol % La_2O_3 , <F>, BEI, $\times 2000$;

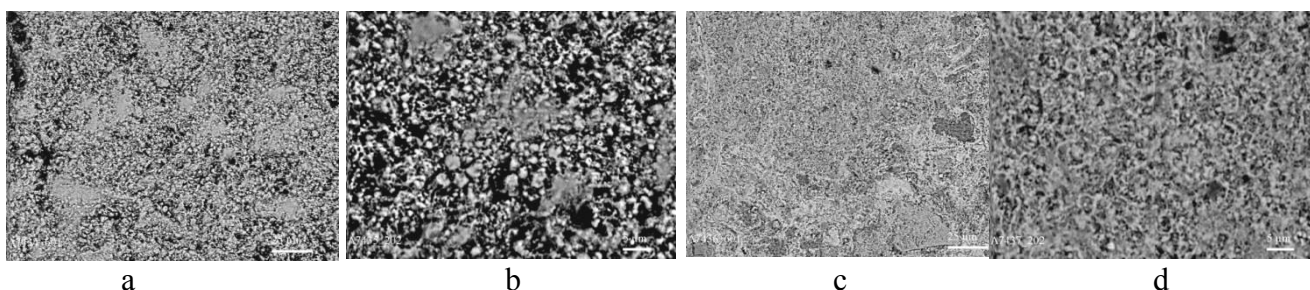


Fig 1.4-Microstructure of the three phase samples (Py+F+A*) of the system $\text{ZrO}_2\text{-CeO}_2\text{-La}_2\text{O}_3$ annealed at 1100 °C:

- a) 42 mol% ZrO_2 - 24 mol% CeO_2 - 34 mol% La_2O_3 , tr, BEI, $\times 600$;
 - b) 42 mol% ZrO_2 - 24 mol% CeO_2 - 34 mol% La_2O_3 , Py+F+A* tr., BEI, $\times 2000$;
 - c) 42 mol% ZrO_2 - 30 mol% CeO_2 - 28 mol% La_2O_3 , Py+F+A* tr., BEI, $\times 600$;
 - d) 42 mol% ZrO_2 - 30 mol% CeO_2 - 28 mol% La_2O_3 , Py+F+A* tr., BEI, $\times 2000$;
- light grains – <F-CeO₂>, gray – <A-La₂O₃>, dark – $\text{La}_2\text{Zr}_2\text{O}_7$, black – pores.

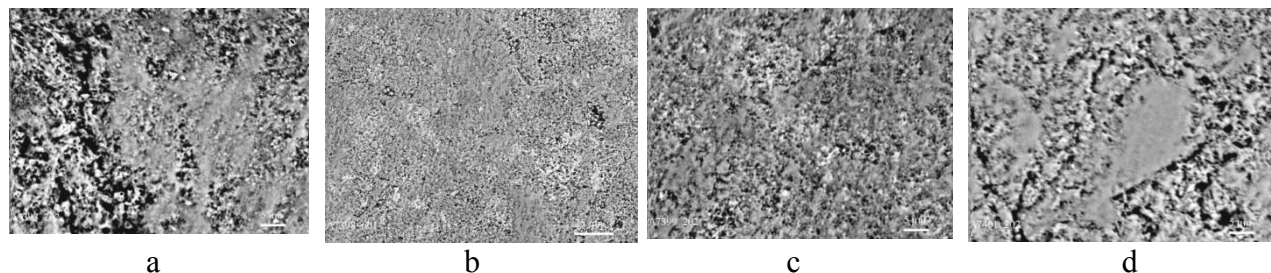


Fig. 1.5-Microstructure of the samples in the system $\text{ZrO}_2\text{-CeO}_2\text{-La}_2\text{O}_3$ after annealing at 1100 °C:

- a) 82 mol% ZrO_2 - 1 mol% CeO_2 - 17 mol% La_2O_3 , Py+M \uparrow , BEI, $\times 2000$;
 - c) 91 mol% ZrO_2 - 1 mol% CeO_2 - 8 mol% La_2O_3 , Py+M, BEI, $\times 600$;
 - d) 91 mol% ZrO_2 - 1 mol% CeO_2 - 8 mol% La_2O_3 , Py+M, BEI, $\times 2000$;
- gray grains - $\text{La}_2\text{Zr}_2\text{O}_7$, dark grains - <M-ZrO₂>, black – pores.

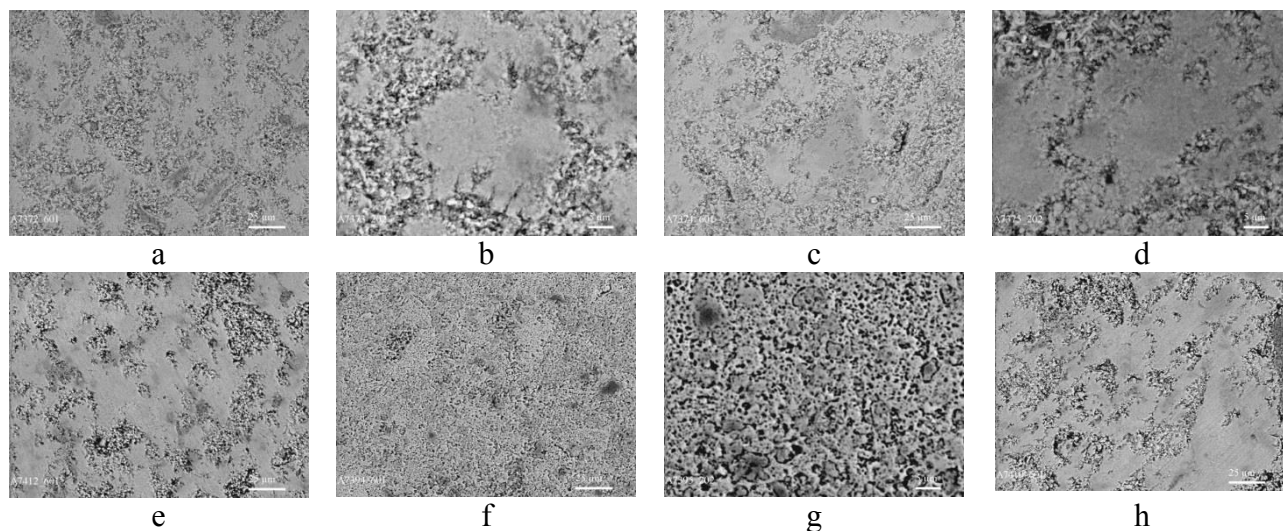


Fig 1.6-Microstructures of the samples of the system $\text{ZrO}_2\text{-CeO}_2\text{-La}_2\text{O}_3$ after annealing at 1100 °C:

- a) 47 mol% ZrO_2 - 26.5 mol% CeO_2 - 26.5 mol% La_2O_3 , F+Py, BEI, $\times 600$;
 - b) 47 mol% ZrO_2 - 26.5 mol% CeO_2 - 26.5 mol% La_2O_3 , F+Py, BEI, $\times 2000$;
 - c) 52 mol% ZrO_2 - 24 mol% CeO_2 - 24 mol% La_2O_3 , F+Py, BEI, $\times 600$;
 - d) 52 mol% ZrO_2 - 24 mol% CeO_2 - 24 mol% La_2O_3 , F+Py, BEI, $\times 2000$;
 - e) 16 mol% ZrO_2 - 76 mol% CeO_2 - 8 mol% La_2O_3 , F- CeO_2 +Py tr., BEI, $\times 600$;
 - f) 16 mol% ZrO_2 - 76 mol% CeO_2 - 8 mol% La_2O_3 , F- CeO_2 +Py tr., BEI, $\times 2000$;
 - g) 59 mol% ZrO_2 - 14 mol% CeO_2 - 27 mol% La_2O_3 , BEI, Py+F tr., $\times 600$;
 - h) 59 mol% ZrO_2 - 14 mol% CeO_2 - 27 mol% La_2O_3 , Py+F tr., BEI, $\times 2000$;
- light grains – $\langle \text{F-CeO}_2 \rangle$, dark grains – $\text{La}_2\text{Zr}_2\text{O}_7$, black – pores.

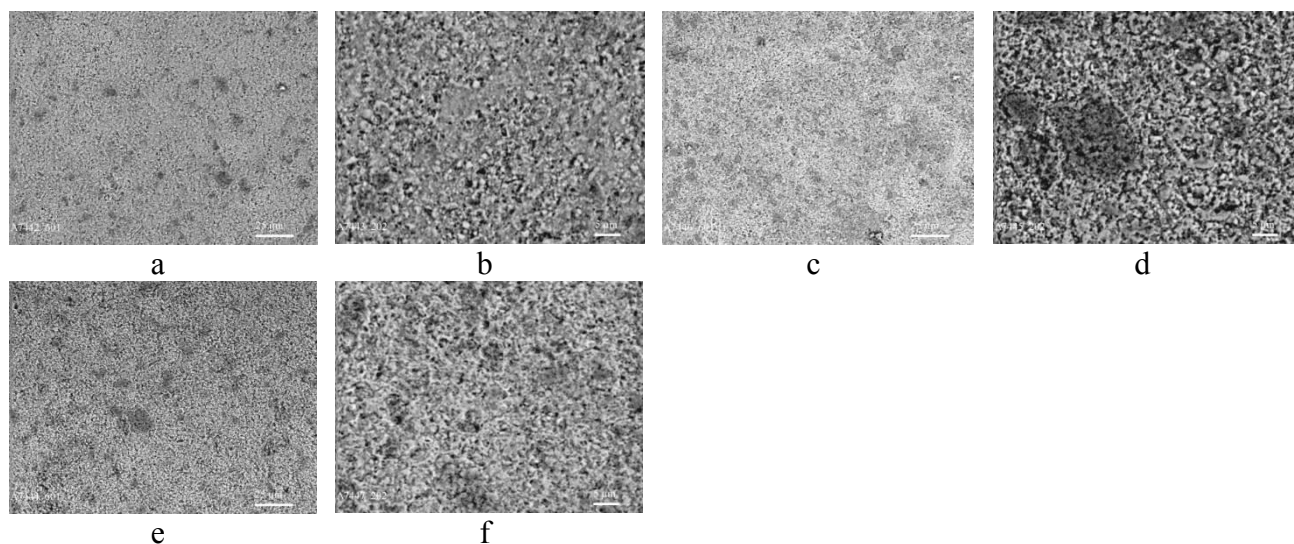


Fig. 1.7-Microstructures of the samples in the system $\text{ZrO}_2\text{-CeO}_2\text{-La}_2\text{O}_3$ after annealing at 1100 °C:

- a) 42 mol% ZrO_2 - 44 mol% CeO_2 - 14 mol% La_2O_3 , Py+F+T* tr, BEI, $\times 600$;
 - b) 42 mol% ZrO_2 - 44 mol% CeO_2 - 14 mol% La_2O_3 , Py+F+T* tr, BEI, $\times 2000$;
 - c) 42 mol% ZrO_2 - 48 mol% CeO_2 - 10 mol% La_2O_3 , Py+F+T**tr, BEI, $\times 600$;
 - d) 42 mol% ZrO_2 - 48 mol% CeO_2 - 10 mol% La_2O_3 , Py+F+T**tr, BEI, $\times 2000$;
 - e) 42 mol% ZrO_2 - 54 mol% CeO_2 - 4 mol% La_2O_3 , F+T**tr \uparrow +Py tr \downarrow , BEI, $\times 600$;
 - f) 42 mol% ZrO_2 - 54 mol% CeO_2 - 4 mol% La_2O_3 , F+T**tr \uparrow +Py tr \downarrow , BEI, $\times 2000$;
- light grains – $\langle \text{F-CeO}_2 \rangle$, gray – $\text{La}_2\text{Zr}_2\text{O}_7$, dark – $\langle \text{T-ZrO}_2 \rangle$ tr, black – pores.

Table 1.2 Phase composition and lattice parameters of the phases in the $\text{ZrO}_2\text{-CeO}_2\text{-La}_2\text{O}_3$ system after annealing at 1100 °C for 12780 hours. (XRD data)

Chemical composition, mol %			Phase composition and lattice parameters of elementary cells, a (nm) by XRD data
ZrO_2	CeO_2	La_2O_3	
1	2	3	4
<u>Περεπίζ ZrO_2 - (50 mol % CeO_2 - 50 mol % La_2O_3)</u>			
32	34	34	$\langle F \rangle$ basis (0.5152) + Py (1.0829) + $\langle A \rangle$ tr
37	31.5	31.5	$\langle F \rangle \downarrow$ + Py basis. (1.0820) + $\langle A \rangle$ tr
47	26.5	26.5	Py (1.0785) + $\langle F \rangle$ tr (0.5393)
52	24	24	Py basis (1.0760) + $\langle F \rangle$ tr \downarrow (0.5380)
57	21.5	21.5	Py basis (1.0749) + $\langle F \rangle$ tr (0.5366) + $\langle T \rangle^{**}$ tr
62	19	19	Py (1.0738) + $\langle F \rangle$ tr \downarrow (0.5356) + $\langle T \rangle^{**}$ tr
72	14	14	Py (1.0749) + $\langle F \rangle$ tr + $\langle T \rangle^{**}$ \uparrow
77	11.5	11.5	Py (1.0752) + $\langle F \rangle$ tr (0.5324) + $\langle T \rangle^{**}$
82	9	9	Py (1.0737) + $\langle F \rangle$ (0.5245) + $\langle T \rangle^{**}$ \uparrow
87	6.5	6.5	Py (1.0752) + $\langle T \rangle^{**}$ + $\langle F \rangle$ tr \downarrow (0.5238)
91	4.5	4.5	Py \downarrow (1.0752) + $\langle T \rangle^{*}$ \uparrow + $\langle F \rangle$ tr $\downarrow \downarrow$ (0.5230)
96	2	2	$\langle M \rangle$ basis + $\langle T \rangle^{*}$ + Py \downarrow (1.0765)
<u>Section ZrO_2 - (90 mol % CeO_2 - 10 mol % La_2O_3)</u>			
0	90	10	$\langle F \rangle$ (0.5443)
5.4	85	9.6	$\langle F \rangle$
11	80.5	8.5	$\langle F \rangle$ (0.5423)
16	76	8	$\langle F \rangle$ (0.5397)
21	71	8	$\langle F \rangle$ (0.5369) + Py tr (1.0738)
26	67	7	$\langle F \rangle$ basis (0.5357) + Py (1.0714)
32	62	6	$\langle F \rangle$ basis (0.5349) + Py tr (1.0702) + $\langle T \rangle^{**}$ tr
37	57	6	$\langle F \rangle$ basis (0.5341) + Py tr (1.0699) + $\langle T \rangle^{*}$ tr
47	47	6	$\langle F \rangle$ basis (0.5341) + Py tr (1.0699) + $\langle T \rangle^{*}$ tr
52	43	5	$\langle F \rangle$ basis (0.5341) + $\langle T \rangle^{**}$ + Py tr $\downarrow \downarrow$
57	39	4	$\langle F \rangle$ basis (0.5346) + $\langle T \rangle^{*}$ \uparrow + Py tr (1.0693)
62	34	4	$\langle F \rangle$ (0.5341) + $\langle T \rangle^{**}$ + Py (1.0682)
67	30	3	$\langle F \rangle$ (0.5342) + $\langle T \rangle^{**}$ + Py (1.0683)
72	25	3	$\langle F \rangle$ (0.5333) + $\langle T \rangle^{*}$ \uparrow + Py (1.0665)
76	21	3	$\langle T \rangle^{*}$ \uparrow + $\langle F \rangle$ (0.5351) + Py (1.0701)
81	17	2	$\langle T \rangle^{*}$ + $\langle F \rangle \downarrow$ (0.5350) + Py (1.0699)
91	8	1	$\langle T \rangle^{*}$ basis + $\langle F \rangle \downarrow$ (0.5341) + Py \uparrow (1.0682)
96	3	1	$\langle T \rangle^{*}$ + Py tr \downarrow (1.0760)
100	0	0	$\langle M \rangle$
<u>Section ZrO_2 - (10 mol % CeO_2 - 90 mol % La_2O_3)</u>			
62	3	35	Py (1.0794)
67	2	31	Py (1.0761) + $\langle M \rangle$ tr
72	2	26	Py (1.0752) + $\langle M \rangle$ tr \uparrow
77	2	21	Py (1.0772) + $\langle M \rangle \uparrow$ + $\langle T \rangle^{**}$ tr
82	1	17	Py (1.0772) + $\langle M \rangle \uparrow$
86	1	13	Py + $\langle M \rangle$
91	1	8	Py + $\langle M \rangle$
95.7	0.3	4	Py \downarrow (1.0763) + $\langle M \rangle \uparrow$

Section CeO₂- (69 mol % ZrO₂-31 mol % La₂O₃)

69	0	31	Py (1.078338)
68	1	31	Py
66	3	31	Py (1.076476)
66	4	30	Py basis (1.0768) + <T>*tr
63	9	28	Py (1.0749) + <F>tr
59	14	27	Py (1.0751) + <F>tr (0.5389)
56	19	25	Py (1.0742) + <F>↑ (0.5392)
49	29	22	Py (1.0749) + <F>↑
46	34	20	Py (1.0742) + <F> (0.5386)
39	44	17	Py↓ (1.0754) + <F> (0.5392)
36	49	15	Py↓ (1.0749) + <F> (0.53896)
32	54	14	Py↓ (1.0749) + <F> (0.53896)
28	59	13	Py tr↓ (1.0742) + <F>↑ (0.5391)
22	69	9	Py tr↓↓ (1.0752) + <F>↑ (0.53896)
15	79	6	<F> (0.5392)
7	90	3	<F> (0.5403)
3	95	2	<F>
0	100	0	<F> (0.5409)

Iso-concentration line 42 mol % ZrO₂

42	24	34	Py (1.0886) + <F> (0.5437) + <A>*tr (a = 0.6557; c = 0.3835)
42	30	28	Py↓ (1.0831) + <F> (0.5414) + <A>*tr (a = 0.6568; c = 0.3828)
42	35	23	Py↓ (1.0785) + <F> (0.5396)
42	40	18	Py (1.0785) + <F> (0.5391)
42	44	14	<F> (0.5374) + Py (1.0749) + <T>*tr
42	48	10	<F> (0.5368) + Py (1.0737) + <T>**tr
42	54	4	<F> (0.5358) + <T>**tr↑ + Py tr↓ (1.0716)
42	58	0	<F>basis (0.5367) + <T>**

Iso-concentration line 86 mol % ZrO₂

86	0	14	<M>+Py
86	1	13	<M> + Py (1.0772)
86	2	12	<M> + Py (1.0772)
86	3	11	<M> + Py (1.0766)
86	5	9	<T>**↑ + Py (1.0763)
86	9	5	<T>**↑ + Py↓ (1.0752) + <F>tr↑
86	11	3	<T>** + Py↓ (1.0725) + <F>↑
86	12	2	<T>** + <F>↑ + Py↓ (1.0714)
86	13	1	<T>** + <F>
86	14	0	<T>*

* Under given conditions (T=1100 °C, 12780 hours., in air) the tetragonal phase T-ZrO₂ and hexagonal phase A-La₂O₃ cannot be stabilized on quenching. Instead of them the monoclinic phase M-ZrO₂ and hexagonal phase La(OH)₃ have been determined instead;

** the partial stabilization of the T- and A- phases has been established.

Legend: <A> – solid solutions based on hexagonal La₂O₃; <T> – solid solutions based on tetragonal modification of ZrO₂; <M> – solid solutions based on monoclinic HfO₂; <F> – solid solutions based on cubic modifications of the fluorite-type CeO₂; Py – ordered phase La₂Zr₂O₇ of the pyrochlore type. Other notations: basis – the main phase, tr – traces of a phase, ↑ – phase amount increases, ↓ – amount decreases.

The boundary of the homogeneity field of the solid solution based on T-ZrO₂ at 1100 °C passes near the compositions: 96 mol % ZrO₂-3 mol % CeO₂-1 mol % La₂O₃ – two-phase (T+Py tr), 91 mol % ZrO₂-8 mol % CeO₂-1 mol % La₂O₃ – three-phase (T basis+F+Py), 86 mol % ZrO₂-13 mol % CeO₂-1 mol % La₂O₃ – two-phase (T+F). Note, solid solutions based on T-form of ZrO₂ at 1100 °C, similarly to those obtained at 1500 °C cannot be stabilize on cooling or even on quenching. On XRD patterns, obtained at room temperatures we found the traces of the M-ZrO₂ lines. Partial stabilization of the T-phase in several composition has been revealed (Table 1.2). Microstructure studies allow findings of phase transitions, such as polysynthetic twinning.

Solid solution based on lanthanum zirconate at 1100 °C co-exists in equilibrium with all phases, existing in the system ZrO₂-CeO₂-La₂O₃, and forms solid solutions of substitution type in the binary systems. The maximum solubility of ceria (to 8 mol % CeO₂) in La₂Zr₂O₇ is observed on the cross-section of CeO₂ – (69 mol % ZrO₂ – 31 mol % La₂O₃), similarly to the sections at 1500, 1450, 1250 °C. The boundary of the homogeneity field of the La₂Zr₂O₇ phase in equilibrium with T-ZrO₂ and A-La₂O₃ at 1100 °C demonstrates substantial extension along the binary system ZrO₂-La₂O₃.

The isothermal cross-section in the sub-section of the ZrO₂-La₂Zr₂O₇-CeO₂ system at 1100 °C is characterized by two three-phase fields (Py+F+T) and (Py+T+M). The boundaries of the three-phase fields are determined by samples located along the iso-concentration line 86 mol % ZrO₂. The microstructures of the samples, characterizing three-phase field (Py+F+T) in the zirconia-rich sub-system, are presented in Fig. 1.7 a-f. In the samples, containing 42 mol % ZrO₂-44 mol % CeO₂-14 mol % La₂O₃, 42 mol % ZrO₂-48 mol % CeO₂-10 mol % La₂O₃, 42 mol % ZrO₂-54 mol % CeO₂-4 mol % La₂O₃, three phases are clearly detected: gray – anisotropic (T), light – isotropic (F) with inclusions of dark-gray phase (Py). The results of x-ray microspectral analysis confirm three phase co-existence.

The maximal extension demonstrates the homogeneity field of the solid solution based on F-CeO₂. The boundary of the F-phase is curved to the CeO₂ corner and passes along the boundary binary systems ZrO₂-CeO₂ (73-100 mol % CeO₂) and CeO₂-La₂O₃ (50-100 mol % CeO₂). The specific microstructures of the F-phase are presented in Fig. 1.3 a-d.

Extension of the F-phase is determined by x-ray diffraction patterns of the following samples: 16 mol % ZrO₂-76 mol % CeO₂-8 mol % - one-phase (F), 21 mol % ZrO₂-71 mol % CeO₂-8 mol % La₂O₃, La₂O₃ 22 mol % ZrO₂-69 mol % CeO₂-9 mol % La₂O₃ – two-phase (F+Py). The boundary solubility of the F-phase along the section CeO₂ - (69 mol % ZrO₂ – 31 mol % La₂O₃) achieves 19 mol % ZrO₂-72 mol % CeO₂-9 mol % La₂O₃. The lattice parameters in this row changes from $a=0.5409$ nm for pure CeO₂ to $a=0.5389$ nm for two-phase samples, which includes 22 mol % ZrO₂-69 mol % CeO₂-9 mol % La₂O₃ (Fig. 1.5).

The fluorite-type phase exists in two-phase (A+F), (T+F), (Py+F) and three-phase (Py+F+T), (Py+A+F) fields. The isothermal section of the partial sub-system La₂O₃-La₂Zr₂O₇-CeO₂ at 1100 °C crosses one three-phase (Py+A+F) and three two-phase (Py+F, Py+A, A+F) fields. The specific microstructures corresponding to two-phase field on phase diagram (Py+F), shown in Fig. 1.6 a-j. In the samples containing 47 mol % ZrO₂-26.5 mol % CeO₂-26.5 mol % La₂O₃, 52 mol % ZrO₂-24 mol % CeO₂-24 mol % La₂O₃, 16 mol % ZrO₂-76 mol % CeO₂-8 mol % La₂O₃, 59 mol % ZrO₂-14 mol % CeO₂-27 mol % La₂O₃, 56 mol % ZrO₂-14 mol % CeO₂-27 mol % La₂O₃, 49 mol % ZrO₂-29 mol % CeO₂-22 mol % La₂O₃, two structural components differ by contrast: light-gray isotropic phase — F with inclusions of other dark isotropic phase — Py. In the sub-system with low amount of ZrO₂, the homogeneity fields of the solid solutions based on F-CeO₂, A-La₂O₃ and phase Py dominate.

Thus, in the present research we first time studied phase equilibria in the systems of ZrO₂-CeO₂-La₂O₃ and CeO₂-La₂O₃ in the whole interval of concentrations and at temperatures 1450, 1250, 1100 °C. The elements of the phase diagram have been developed for the binary system CeO₂-La₂O₃ and isothermal sections of the ternary ZrO₂-CeO₂-La₂O₃ system at given temperatures.

Formation of the finite-solubility solid solutions based on input components was revealed in the binary and ternary diagrams. Phase equilibria in the system at temperatures 1500, 1450, 1250 and 1100 °C look similar, however, substantial differences are observed, which are defined by constitution of the boundary binary system and features of the phase formation in the ternary system. In opposite to constitution of isothermal section at 1450, 1250 °C the section of the ZrO_2 - CeO_2 - La_2O_3 system at 1100 °C consists of (Py+T+F, Py+F+A, Py+T+M) three phase fields and six two-phase fields (Py+A, Py+T, Py+F, Py+M, F+T, A+F). From the given isothermal sections at various temperatures, the extension of the homogeneity and two-phase fields shortens, and the extension of the three-phase fields gradually widens, number of the phase fields increases due to tetragonal – monoclinic transformation in zirconia.

The diagram of the system ZrO_2 - CeO_2 - La_2O_3 at 1100 °C has been studied in details in the zirconia-rich field, but the lanthana-rich part of the diagram requires more efforts to be completely studied.

1.2. Phase equilibria in the ZrO_2 — CeO_2 — Eu_2O_3 system

The system ZrO_2 - CeO_2 - Eu_2O_3 is one of the most interesting and prospective ternary system. Development of new generation materials requires phase equilibria research, phase relationships and stability in this system at various temperatures.

Phase relations in the boundary binary systems ZrO_2 - CeO_2 , ZrO_2 - Eu_2O_3 were studied incompletely [24], and phase equilibria data about the CeO_2 - Eu_2O_3 system is contradictory [25-35].

Zirconia reaction with ceria has been studied in [36-79]. The diagram of the ZrO_2 - CeO_2 system has been developed in [11, 36-38] (Fig. 1.8). Several discrepancies, however, were found in the phase diagrams proposed as at temperatures below 1100 °C with uncertain coordinates for tetragonal to monoclinic eutectoid and $\text{Ce}_2\text{Zr}_3\text{O}_{10}$ (Φ) phase, as above 1600 °C because of partial transformation of CeO_2 to Ce_2O_3 .

In the low-temperature area (≤ 1500 °C), the state diagrams of the ZrO_2 - CeO_2 system includes the following phases: monoclinic M- ZrO_2 in the range from 0 to 1 mol % CeO_2 at 1100 °C, tetragonal T- ZrO_2 in the range from 0 to 18 mol % CeO_2 at 1500, 1450 °C and from 2 to 18 mol % CeO_2 at 1100 °C and cubic phase of the fluorite type structure F- CeO_2 in the interval from 56 to 100 mol % CeO_2 at 1500 °C, from 60 to 100 mol % CeO_2 at 1450 °C and from 73 to 100 mol % CeO_2 at 1100 °C. The wide two-phase field (F+T) has been revealed in the concentration range from 18 to 56 mol % CeO_2 at 1500 °C, from 18 to 60 mol % CeO_2 at 1450 °C and two heterogenic fields at 1100 °C: wide two-phase fields (F+T) in the concentration range from 18 to 73 mol % CeO_2 and narrow two-phase field (M+T) in the concentration range from 1 to 2 mol % CeO_2 . The tetragonal modification of ZrO_2 cannot be quenched, the monoclinic phase M- ZrO_2 was always indicated instead [36-39].

The system ZrO_2 - Eu_2O_3 has been studied using various methods for sample manufacturing, techniques for phase composition research and their properties' studies [63, 80-98]. This phase diagram was studied most completely in [24, 96, 97]. The reaction of zirconia with europia was studied in details in the wide temperature range of 1250-2700 °C, and the full diagram was studied for the system ZrO_2 - Eu_2O_3 (Fig. 1.9).

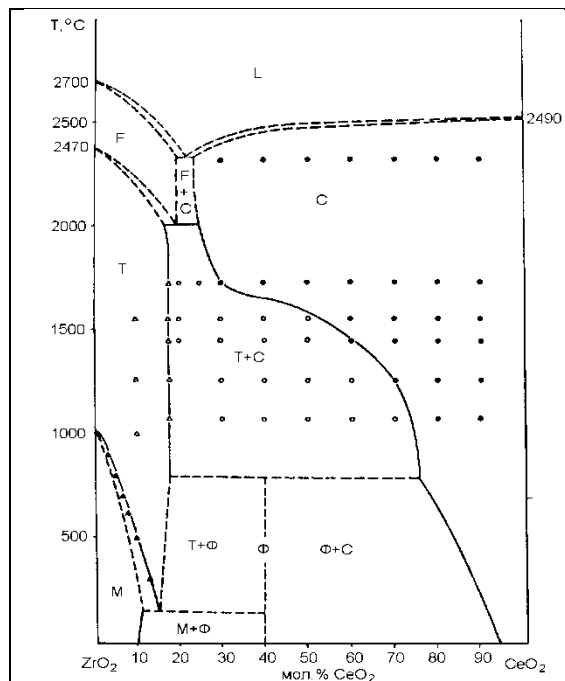


Fig. 1.8 – Phase diagrams of the binary system $\text{ZrO}_2\text{-CeO}_2$ [38]

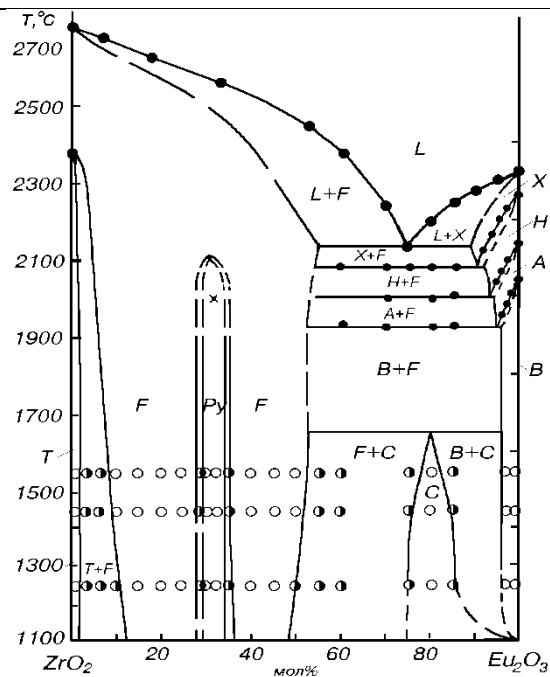


Fig. 1.9 – Phase diagram of the binary system $\text{ZrO}_2\text{-Eu}_2\text{O}_3$ (● - thermal analysis in air using solar energy; ○ - one-phase, ◐ - two-phase samples) [24]

The liquidus surface of the $\text{ZrO}_2\text{-Eu}_2\text{O}_3$ system is characterized by eutectic reaction $L \rightleftharpoons F + X$ (2130 °C, 26 mol % ZrO_2). Additives of europium oxide to zirconia decrease melt temperatures and phase transition points in ZrO_2 . Dissolution of 1 mol% Eu_2O_3 in ZrO_2 is enough to stabilize cubic solid solution of fluorite type at 1250 °C. of Eu_2O_3 in T- ZrO_2 is about ~ 1 mol % Eu_2O_3 (1250 °C) becomes wider to 2 mol % at higher temperature of 1550 °C.

The two phase field (T + F) shrinks with temperature decrease: from 1÷13 mol% Eu_2O_3 at 1250 °C to 2÷8 mol% Eu_2O_3 at 1550 °C. Existence of intermediate phase $\text{Eu}_2\text{Zr}_2\text{O}_7$ with pyrochlore-type structure and lattice period $a = 1.0540 \pm 0.0005$ nm (in the composition 66.7 mol% ZrO_2 at 1550 °C) and refraction index $2.07 < n < 2.10$. The homogeneity field of the pyrochlore phase at 1250 and 1550 °C is located in the range 30÷35 mol% Eu_2O_3 and 30÷34 mol % Eu_2O_3 , respectively. The solubility gap splits the field of the fluorite type solid solutions in the considered here temperature and concentration range, which is from 1250 to 1550 °C and 13÷25 and 37÷45, 8÷28 and 36÷52 mol% Eu_2O_3 , respectively. Lattice parameters (a) increase from 0.5159 to 0.5225 nm and from 0.5286 to 0.5335 nm at 1550 °C. The refraction index of the isotropic F-phase $n = 2.07$ (for composition 45 mol% Eu_2O_3 , 1550 °C). There are two-phase (F + Py) fields separating the homogeneity fields of one pyrochlore field and two fluorite field.

In the europia-rich phase field, the phase relations are complicated much by polymorphism of Eu_2O_3 . Dissolving of zirconia in europia leads to stabilization of cubic europia and increases its temperature range of existence. When temperature increased, the size of homogeneity field of C- Eu_2O_3 phase decreases from 25÷15 mol% ZrO_2 (1250 °C) to 21÷19 mol % ZrO_2 (1550 °C), and boundaries of two-phase fields (F + C) and (B + C) widen from 55÷25 and 15÷2 mol% ZrO_2 (1250 °C) to 48÷21 and 19÷4 mol% ZrO_2 (1550 °C), respectively.

Solid solutions based on tetragonal (T) and cubic of fluorite structure (F) ZrO_2 , cubic form (C, X), monoclinic (B), hexagonal (A, H) modifications of Eu_2O_3 , and ordered intermediate phase $\text{Eu}_2\text{Zr}_2\text{O}_7$ of pyrochlore type (Py), as well as two-phase fields T+F, F+Py, B+C, F+C, F+(B, A, H, X) were found and studied.

Boundaries of the homogeneity field for the B-type Eu_2O_3 solid solutions are not wider than 2 mol % ZrO_2 (1250) i 4 mol % ZrO_2 (1550 °C). Boundary solubility of ZrO_2 in polymorphs B-, A-

, H- i X- Eu_2O_3 achieves 6, 7, 8 and 10 mol% ZrO_2 . Temperatures of eutectoid transformations have been determined as 1920, 2000, 2080 ± 20 °C.

In the system $\text{ZrO}_2\text{-Eu}_2\text{O}_3$, the following phases were found at 1500 °C: B- Eu_2O_3 in the interval from 0 to 3 mol% ZrO_2 , C- Eu_2O_3 in the range from 17 to 20 mol% ZrO_2 , F- ZrO_2 in the interval from 45 to 63 mol% ZrO_2 and from 72 to 90 mol% ZrO_2 , $\text{Eu}_2\text{Zr}_2\text{O}_7$ in the interval from 65 to 70 mol% ZrO_2 , T- ZrO_2 in the interval from 98 to 100 mol% ZrO_2 . The two-phase fields were determined: (B + C) in the range 3 to 17 mol% ZrO_2 , (C + F) in the range 20-45 mol% ZrO_2 , (F + Py) - from 63 to 65 mol% ZrO_2 and from 70 to 72 mol% ZrO_2 and (F + T) in the concentration range 90÷98 mol % ZrO_2 .

The system $\text{CeO}_2\text{-Eu}_2\text{O}_3$ has been studied incompletely. No phase diagrams were published yet. There is very limited information about some phases and their properties [25-35]. With the aid of XRD analysis at room temperature the reaction between CeO_2 and Eu_2O_3 has been studied [28, 35]. Samples have been prepared at 1200 °C by solid phase sintering in air of pure oxides obtained by nitrate decomposition at 500 °C. Two types of solid solutions with cubic structures (CaF₂-type and Th_2O_3 -type) inherent in pure oxides [35] exist in this system. Phase reactions in the system $\text{CeO}_2\text{-Eu}_2\text{O}_3$ were studied in [26, 29-33]. It was shown that the cubic solid solutions of the fluorite type (F- CeO_2) are formed at temperature 1400 °C in the range from pure CeO_2 to 40 mol% Eu_2O_3 and from 40 to 100 mol% Eu_2O_3 (C- Eu_2O_3). Lattice parameters of cubic solid solutions vary from $a = 5.411$ nm for pure CeO_2 to $a = 5.441$ nm in composition, which contains 40 mol% Eu_2O_3 and (45 mol% Eu_2O_3) to $a = 10.868$ nm (100 mol% Eu_2O_3). Existence of two-phase field in the given system has not been found [26]. The thermal expansion coefficient $\alpha_a \cdot 10^6$ (0-1400°C) of solid solutions $\text{Ce}_{1-x}\text{Eu}_x\text{O}_{2-x/2}$ increases 9.89; 11.44; 11.6; 13.17 in the row $x = 0.90$; 0.55; 0.45; 0.1, respectively [26].

Some characteristics formed in the given system are shown in the Table. 1.3-1.5.

Table 1.3 – Dielectric constants (ϵ_∞) of materials $\text{Ce}_{0.8}\text{Ln}_{0.2}\text{O}_{2-\delta}$ (Ln = Gd, Eu) [31]

Composition	ϵ_∞ 300 °C	ϵ_∞ 400 °C	ϵ_∞ 500 °C	ϵ_∞ 550 °C
$\text{Ce}_{0.8}\text{Gd}_{0.2}\text{O}_{2-\delta}$	5,44	12,29	16,74	20,05
$\text{Ce}_{0.8}\text{Eu}_{0.2}\text{O}_{2-\delta}$	6,09	7,91	13,12	19,64

Table 1.4 – Conductivity and its activation energy for the solid solutions $\text{Ce}_{0.8}\text{Ln}_{0.2}\text{O}_{2-\delta}$ (Ln = Gd, Eu) by the data [33]

Composition	E_a , (eV) (480-550 °C)	σ_{gi} (Sm/sm) at 550 °C	σ_{gb} (Sm/sm) at 550 °C	σ (Sm/sm) при 550 °C
$\text{Ce}_{0.8}\text{Gd}_{0.2}\text{O}_{2-\delta}$	1,07	$5,8 \cdot 10^{-4}$	$7,3 \cdot 10^{-4}$	$1,8 \cdot 10^{-4}$
$\text{Ce}_{0.8}\text{Eu}_{0.2}\text{O}_{2-\delta}$	0,91	$3,45 \cdot 10^{-4}$	$4,4 \cdot 10^{-4}$	$1,39 \cdot 10^{-4}$

Table 1.5 – Thermal expansion coefficient for pure CeO_2 and one doped with Ln^{3+} [34]

Composition	Thermal expansion coefficient $\alpha_a \cdot 10^6$ (0-1200 °C)
CeO_2	12.68
$\text{Ce}_{0.5}\text{La}_{0.5}\text{O}_{1.75}$	10.48
$\text{Ce}_{0.5}\text{Nd}_{0.5}\text{O}_{1.75}$	11.87
$\text{Ce}_{0.5}\text{Sm}_{0.5}\text{O}_{1.75}$	12.10
$\text{Ce}_{0.5}\text{Eu}_{0.5}\text{O}_{1.75}$	12.61
$\text{Ce}_{0.5}\text{Gd}_{0.5}\text{O}_{1.75}$	12.47
$\text{Ce}_{0.5}\text{Dy}_{0.5}\text{O}_{1.75}$	11.77
$\text{Ce}_{0.5}\text{Ho}_{0.5}\text{O}_{1.75}$	11.95
$\text{Ce}_{0.5}\text{Er}_{0.5}\text{O}_{1.75}$	12.29
$\text{Ce}_{0.5}\text{Yb}_{0.5}\text{O}_{1.75}$	12.32
$\text{Ce}_{0.5}\text{Lu}_{0.5}\text{O}_{1.75}$	12.45

First, phase equilibria in the ternary $\text{ZrO}_2\text{-CeO}_2\text{-Eu}_2\text{O}_3$ system at temperature 1500 °C and binary $\text{CeO}_2\text{-Eu}_2\text{O}_3$ system at temperatures 1500, 1100 and 600 °C have been studied in the whole interval of concentrations. The following samples have been prepared along the six sections: ZrO_2 - (50 mol % CeO_2 - 50 mol % Eu_2O_3), ZrO_2 - (10 mol % CeO_2 - 90 mol % Eu_2O_3), ZrO_2 - (30 mol % CeO_2 - 70 mol % Eu_2O_3), ZrO_2 - (70 mol % CeO_2 - 30 mol % Eu_2O_3), CeO_2 - (67 mol % ZrO_2 - 33 mol % Eu_2O_3), Eu_2O_3 - (60 mol % ZrO_2 - 40 mol % CeO_2) and iso-concentration lines: 20 mol % ZrO_2 , 45 mol % ZrO_2 and 85 mol % ZrO_2 .

Thermal treatment of samples of the ternary $\text{ZrO}_2\text{-CeO}_2\text{-Eu}_2\text{O}_3$ system at 1500 °C was carried out in two stages: in the furnace with heating elements H23U5T at 1100 °C for 452 h and in the furnace with MoSi_2 heating elements at 1500 °C for 150 h in air.

Annealing of samples of the binary $\text{CeO}_2\text{-Eu}_2\text{O}_3$ system was carried out at 1500 °C (for 170 h), 1100 °C (16800 h), 600 °C (33061 h). Similarly, to study phase equilibria in the $\text{CeO}_2\text{-Eu}_2\text{O}_3$ system at 1500 °C firing of samples was carried out in two stages: in the furnace with heating elements H23U5T at 1100 °C for 17 h and in the furnace with MoSi_2 heating elements at 1500 °C for 170 h in air.

The system $\text{CeO}_2\text{-Eu}_2\text{O}_3$

Solid state reactions of CeO_2 (fluorite type, F) and Eu_2O_3 (monoclinic, B) has shown, that in the system $\text{CeO}_2\text{-Eu}_2\text{O}_3$ at temperature 1500 °C three solid solutions formed: two cubic F- CeO_2 and C- Eu_2O_3 , and one monoclinic B- Eu_2O_3 , corresponding to pure components (Fig. 1.10). Temperature decrease to 600 °C results in decrease of the phase fields number. The monoclinic phase B - Eu_2O_3 is not stable below 1000 °C [25].

The chemical and phase compositions of the samples, annealed at 1500, 1100 and 600 °C, lattice parameters of equilibrium phases, are listed in the Tables 1.6-1.8. The boundaries of the homogeneity fields for solid solutions based on F- CeO_2 , C- Eu_2O_3 and B- Eu_2O_3 at 1500 °C are determined by compositions 20-25 mol% Eu_2O_3 , 80-85 mol% Eu_2O_3 and 0.5-99 mol % Eu_2O_3 (Table 1.6). At 1100 °C the boundaries of homogeneity fields for the phases F- CeO_2 and C- Eu_2O_3 are determined by compositions 20÷25 mol% Eu_2O_3 and 90÷99 mol% Eu_2O_3 , respectively (Table 1.7). When temperature decreasing to 600 °C, the homogeneity fields of the solid solutions based on F- CeO_2 and C- Eu_2O_3 becomes gradually narrower. The boundaries of them at 600 °C are determined by configuration points of 10÷15 mol% Eu_2O_3 and 97÷98 mol% Eu_2O_3 , respectively (Table 1.8). Variation of lattice parameter against chemical composition (concentration of Eu_2O_3) of the F- CeO_2 solid solution is shown in Fig. 1.11.

From these data we have concluded, that the solubility of Eu_2O_3 in the F- CeO_2 solid solution achieves 20 mol % at 1500, 1100 °C and 10 mol% at 600 °C. The lattice parameter increases from $a=0.5409$ nm in pure CeO_2 to $a=0.5425$ nm in boundary solid solution (1500, 1100 °C) and $a=0.5422$ nm (600 °C) for the sample containing 15 mol% Eu_2O_3 . The XRD and petrography research coincide with electron microscopy observations and measurements. Typical microstructures of the phases formed in the $\text{CeO}_2\text{-Eu}_2\text{O}_3$ system at temperatures 1500, 1100, 600 °C are shown in Figs. 1.12-1.13. The microstructures of two phase samples (B + C) annealed at 1500 °C are presented in Fig. 1.12 a-d. In the samples containing 4 mol% CeO_2 -96 mol% Eu_2O_3 and 5 mol% CeO_2 -95 mol% Eu_2O_3 two structural components were found as different by contrast (Fig. 1.12 a). The light phase is a matrix of the monoclinic B europia by the data of microdiffraction analysis.

Another phase looks like dark inclusions can be identified as cubic (C) modification of Eu_2O_3 , which has been confirmed by the XRD analysis (Table. 1.6) and petrography. The absolutely dark, opaque and anisotropic grains of monoclinic B phase have been observed on reflection, which is a matrix filled with randomly distributed small-to-medium inclusions of light,

isotropic, transparent C-Eu₂O₃ phase. When the ceria content increasing the amount of isotropic transparent C-phase growing.

Table 1.6 - Chemical and phase composition, parameters of elementary cells of the system CeO₂-Eu₂O₃ after annealing at 1500 °C for 170 hours. (XRD data, petrography and electron microscopy)

Chemical composition, mol. %		Phase composition	Parameters of elementary cells, nm ($a \pm 0.0002$)					
CeO ₂	Eu ₂ O ₃		<F>	<C>				
			<i>a</i>	<i>a</i>	<i>a</i>	<i>b</i>	<i>c</i>	β
1	2	3	4	5	6	7	8	9
0	100		-	-	1.4328	0.3579	0.8636	92.30
1	99	 basis + <C>	-	1.0854	1.6388	0.3626	0.8644	97.11
2	98	 basis + <C>↑	-	1.0841	1.4146	0.3596	0.8711	87.80
3	97	 basis + <C>↑	-	1.0839	1.4404	0.3573	0.8892	89.36
4	96	 basis + <C>	-	1.0841	1.5552	0.3596	0.8667	93.88
5	95	 + <C>	-	1.0837	1.5601	0.3668	0.8727	101.2
10	90	<C> basis↑ + 	-	1.0855	1.7250	0.3647	0.8810	99.60
15	85	<C> + tr	-	1.0844	-	-	-	-
20	80	<C>	-	1.0856	-	-	-	-
25	75	<C>	-	1.0863	-	-	-	-
30	70	<C> basis + <F> tr	-	1.0853	-	-	-	-
35	65	<C> basis + <F> tr	-	1.0863	-	-	-	-
40	60	<C> basis + <F> tr	-	1.0856	-	-	-	-
45	55	<C> basis + <F>↑	0.5423	1.0863	-	-	-	-
50	50	<C> basis + <F>↑	0.5423	1.0860	-	-	-	-
55	45	<C> + <F>↑	0.5423	1.0845	-	-	-	-
60	40	<C>↓ + <F>↑	0.5425	1.0867	-	-	-	-
65	35	<F> basis + <C>↓	0.5410	1.0820	-	-	-	-
70	30	<F> basis + <C> tr↓	0.5424	1.0847	-	-	-	-
75	25	<F> + <C> tr	0.5423	-	-	-	-	-
80	20	<F> basis	0.5425	-	-	-	-	-
85	15	<F>	0.5423	-	-	-	-	-
90	10	<F>	0.5418	-	-	-	-	-
95	5	<F>	0.5413	-	-	-	-	-
0	100	<F>	0.5409	-	-	-	-	-

Phase identifier: – solid solution based on monoclinic Eu₂O₃; <C> – solid solutions based on cubic modification of Eu₂O₃; <F> – solid solutions of cubic phase with fluorite-type of CeO₂. Other conditions: basis – phase dominating in the compositions, tr – phase traces, ↑ – increasing, ↓ – decrease.

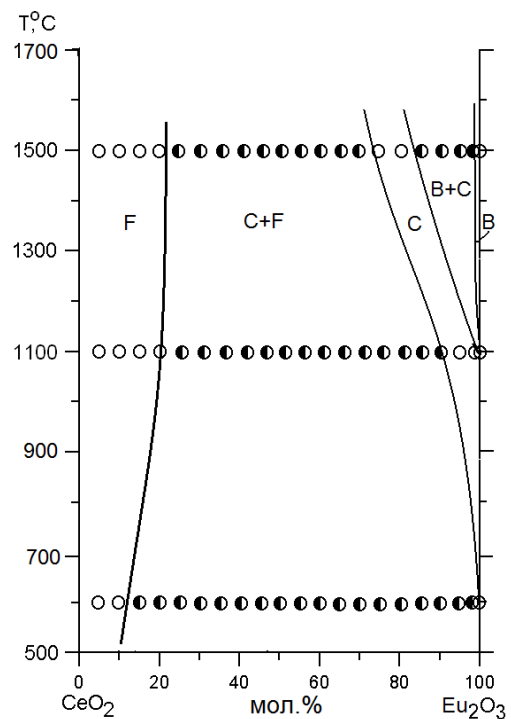
Table 1.7 - Chemical and phase composition, parameters of elementary cells of the system CeO₂-Eu₂O₃ after annealing at 1100 °C for 15960 hours. (XRD data, petrography and electron microscopy)

Chemical composition, mol. %		Phase composition and lattice parameters by XRD data, nm	Parameters of elementary cells, nm ($a \pm 0.0002$)	
CeO ₂	Eu ₂ O ₃		<F>	<C>
			<i>a</i>	<i>a</i>
1	2	3	4	5
0	100	<B-Eu ₂ O ₃ > ($a = 1.4882$, $b = 0.3562$, $c = 0.8960$, $\gamma = 90.2562$)	-	-
1	99	<C-Eu ₂ O ₃ > basis + <B-Eu ₂ O ₃ > tr.	-	1.0840
2	98	<C-Eu ₂ O ₃ >	-	1.0844
3	97	<C-Eu ₂ O ₃ >	-	1.0843
4	96	<C-Eu ₂ O ₃ >	-	1.0838
5	95	<C-Eu ₂ O ₃ >	-	1.0843
10	90	<C-Eu ₂ O ₃ > basis + <F-CeO ₂ > tr.	-	1.0846
15	85	<C-Eu ₂ O ₃ > basis + <F-CeO ₂ > tr.	-	1.0843
20	80	<C-Eu ₂ O ₃ > + <F-CeO ₂ > tr.	-	1.0842
25	75	<C-Eu ₂ O ₃ > basis + <F-CeO ₂ > ↑	-	1.0847
30	70	<C-Eu ₂ O ₃ > basis + <F-CeO ₂ > ↑	-	1.0840
35	65	<C-Eu ₂ O ₃ > + <F-CeO ₂ >	-	1.0845
40	60	<C-Eu ₂ O ₃ > + <F-CeO ₂ >	0.5431	1.0857
45	55	<C-Eu ₂ O ₃ > basis + <F-CeO ₂ > ↑	0.5431	1.0857
50	50	<C-Eu ₂ O ₃ > ↓ + <F-CeO ₂ >	0.5430	1.0868
55	45	<C-Eu ₂ O ₃ > ↓ + <F-CeO ₂ > ↑	0.5431	1.0861
60	40	<C-Eu ₂ O ₃ > ↓ + <F-CeO ₂ > ↑	0.5424	1.0864
65	35	<F-CeO ₂ > ↑ + <C-Eu ₂ O ₃ > ↓↓	0.5434	1.0867
70	30	<F-CeO ₂ > basis + <C-Eu ₂ O ₃ > ↓↓	0.5425	1.0861
75	25	<F-CeO ₂ > + <C-Eu ₂ O ₃ > tr.	0.5427	-
80	20	<F-CeO ₂ > basis	0.5425	-
85	15	<F-CeO ₂ >	0.5422	
90	10	<F-CeO ₂ >	0.5420	
95	5	<F-CeO ₂ >	0.5412	
0	100	<F-CeO ₂ >	0.5409	

Table 1.8 - Chemical and phase composition, parameters of elementary cells of the system CeO_2 - Eu_2O_3 after annealing at 600 °C for 33061 hours. (XRD data, petrography and electron microscopy)

Chemical composition, mol. %		Phase composition	Parameters of elementary cells, nm (<i>a</i> ± 0.0002)	
CeO ₂	Eu ₂ O ₃		<F>	<C>
			<i>a</i>	<i>a</i>
1	2	3	4	5
0	100	<C-Eu ₂ O ₃ >	-	1.0837
1	99	<C-Eu ₂ O ₃ >	-	1.0838
2	98	<C-Eu ₂ O ₃ >	-	1.0821
3	97	<C-Eu ₂ O ₃ > basis + <F-CeO ₂ > tr	-	1.0846
4	96	<C-Eu ₂ O ₃ > + <F-CeO ₂ > tr	-	1.0847
5	95	<C-Eu ₂ O ₃ > basis + <F-CeO ₂ > tr незнач.	-	1.0840
10	90	<C-Eu ₂ O ₃ > + <F-CeO ₂ > tr	-	1.0840
15	85	<C-Eu ₂ O ₃ > basis + <F-CeO ₂ > tr	0.5420	1.0840
20	80	<C-Eu ₂ O ₃ > + <F-CeO ₂ > tr ↑	0.5422	1.0844
25	75	<C-Eu ₂ O ₃ > basis + <F-CeO ₂ > tr	-	1.0833
30	70	<C-Eu ₂ O ₃ > basis + <F-CeO ₂ >	0.5420	1.0840
35	65	<C-Eu ₂ O ₃ > + <F-CeO ₂ >	0.5416	1.0828
40	60	<C-Eu ₂ O ₃ > ↓ + <F-CeO ₂ > ↑	0.5416	1.0842
45	55	<C-Eu ₂ O ₃ > basis + <F-CeO ₂ >	0.5414	1.0840
50	50	<C-Eu ₂ O ₃ > ↓ + <F-CeO ₂ >	0.5416	1.0829
55	45	<C-Eu ₂ O ₃ > ↓ + <F-CeO ₂ > ↑	0.5410	1.0821
60	40	<C-Eu ₂ O ₃ > ↓ + <F-CeO ₂ > ↑	0.5414	1.0829
65	35	<F-CeO ₂ > ↑ + <C-Eu ₂ O ₃ > ↓↓	0.5415	1.0827
70	30	<F-CeO ₂ > + <C-Eu ₂ O ₃ >	0.5416	1.0832
75	25	<F-CeO ₂ > basis + <C-Eu ₂ O ₃ > tr	0.5411	1.0821
80	20	<F-CeO ₂ > basis + <C-Eu ₂ O ₃ > tr ↓↓	0.5414	1.0828
85	15	<F-CeO ₂ > basis + <C-Eu ₂ O ₃ > tr ↓↓↓	0.5422	1.0820
90	10	<F-CeO ₂ > basis	0.5410	-
95	5	<F-CeO ₂ >	0.5410	-
0	100	<F-CeO ₂ >	0.5409	-

Phase identifier: $\langle \text{B} \rangle$ – solid solution based on monoclinic Eu_2O_3 ; $\langle \text{C} \rangle$ – solid solutions based on cubic modification of Eu_2O_3 ; $\langle \text{F} \rangle$ – solid solutions of cubic phase with fluorite-type of CeO_2 . Other conditions: basis – phase dominating in the compositions, tr – phase traces, ↑ – increasing, ↓ – decrease.



(○ – one-phase, ● – two-phase samples)

Fig. 1.10 – Phase diagram in the system CeO_2 - Eu_2O_3 at 600-1500 $^\circ\text{C}$

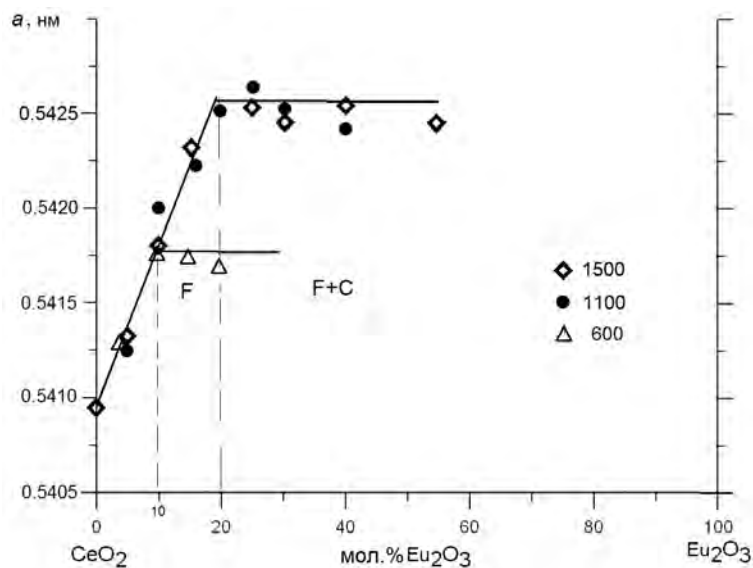


Fig. 1.11 – Concentration dependence of elementary lattice parameters of the solid solutions based on F- CeO_2 in the system CeO_2 - Eu_2O_3 after annealing at (◇) 1500 $^\circ\text{C}$, (●) 1100 $^\circ\text{C}$ and (△) 600 $^\circ\text{C}$

The grain size of solid solutions of fluorite type F- CeO_2 grows from 41 to 81 nm. These data are presented in Table 1.9.

Table 1.9 – Particle size of the solid solution F- CeO_2 in the system CeO_2 - Eu_2O_3 in the temperature interval 600-1500 $^\circ\text{C}$

Composition of the solid solution	Particle size, nm		
	1500 $^\circ\text{C}$	1100 $^\circ\text{C}$	600 $^\circ\text{C}$
$\text{Ce}_{0.95}\text{Eu}_{0.05}\text{O}_{1.95}$	54	65	81
$\text{Ce}_{0.9}\text{Eu}_{0.1}\text{O}_{1.925}$	44	65	81
$\text{Ce}_{0.85}\text{Eu}_{0.15}\text{O}_{1.9}$	41	54	54

In the samples containing from 10 to 15 mol% CeO_2 , the cubic modification of europia becomes basis (Fig. 1.12 d). In the Fig. 1.12 d the fractography clearly shows fragile type of fracture in the microstructure of C- Eu_2O_3 including multiple pores. Fine grain structure of the one phase field (C- Eu_2O_3) is presented in Fig. 1.12 e-f. Further increasing of ceria content in the sample, results in rude relief on the polished surface and sharp edges (Fig. 1.12 f). The traces of cubic phase with fluorite-type cerium oxide appear in the sample containing 30 mol% CeO_2 -70 mol% Eu_2O_3 . By the data of back scattered electron microscopy (BEI), two phases were revealed (C- Eu_2O_3 + F- CeO_2), different by morphology and surface contrast. The oriented light gray stripes related to the solid solutions (C- Eu_2O_3) and fine grain dark grains of near spherical shape (F- CeO_2) (Fig. 1.12 g, h). By the data of petrography in the reflected light, the main part of microstructure includes isotropic dark phase of europia with light isotropic inclusions of F- CeO_2 . It's worth paying attention, that the color of the phase under electron microscope and petrography microscope are strongly different.

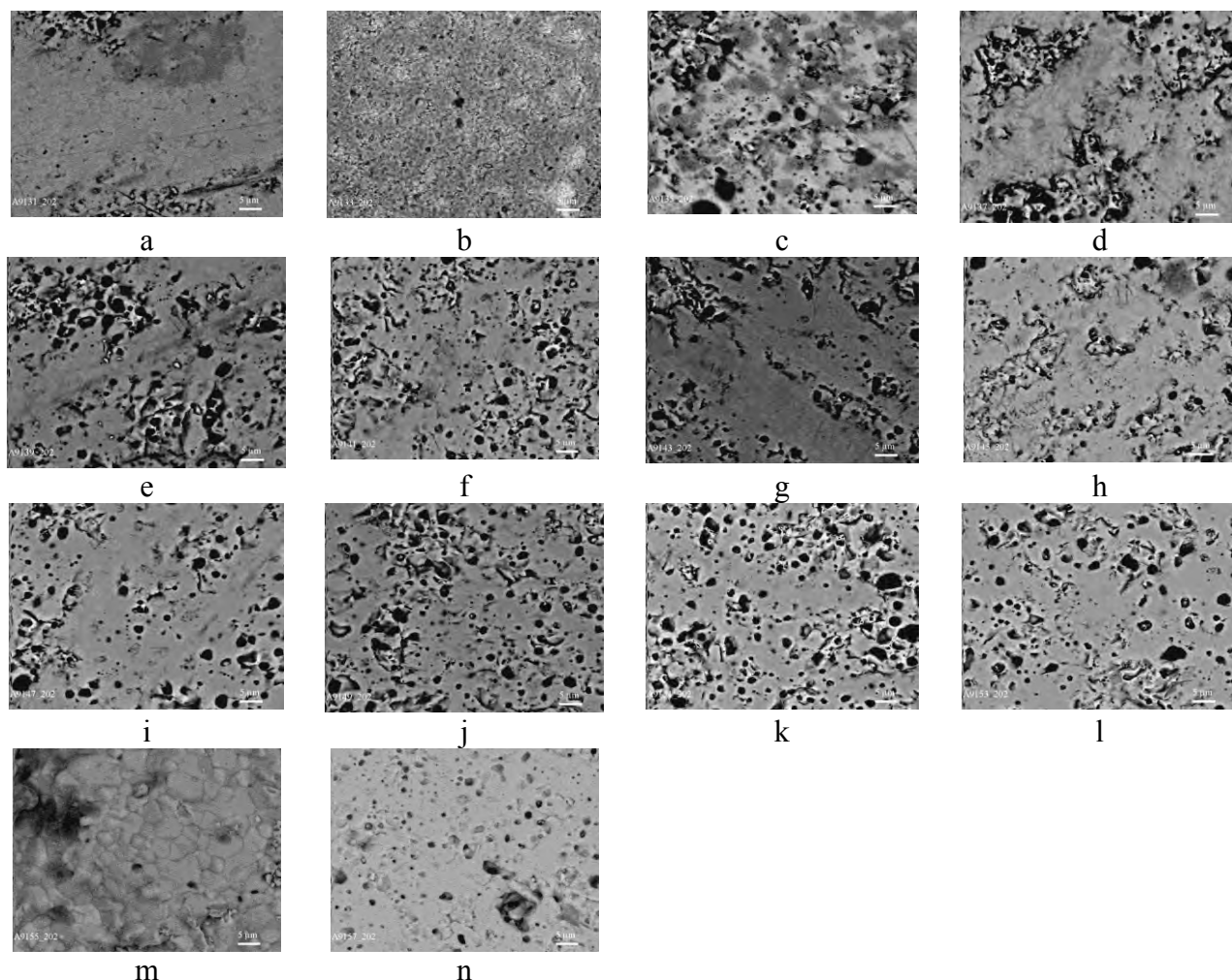


Fig 1.12 - Microstructure of samples in the $\text{CeO}_2\text{-Eu}_2\text{O}_3$ system after annealing at 1500 °C:

- a) 4 mol % CeO_2 -96 mol % Eu_2O_3 , $\langle\text{B-Eu}_2\text{O}_3\rangle$ basis + $\langle\text{C-Eu}_2\text{O}_3\rangle$, BEI, $\times 2000$;
light phase - $\langle\text{B-Eu}_2\text{O}_3\rangle$, gray phase (inclusions) - $\langle\text{C-Eu}_2\text{O}_3\rangle$, black – pores;
- b) 5 mol % CeO_2 -95 mol % Eu_2O_3 , $\langle\text{B-Eu}_2\text{O}_3\rangle$ + $\langle\text{C-Eu}_2\text{O}_3\rangle$, BEI, $\times 2000$;
- c) 10 mol % CeO_2 -90 mol % Eu_2O_3 , $\langle\text{C-Eu}_2\text{O}_3\rangle$ basis + $\langle\text{B-Eu}_2\text{O}_3\rangle$, BEI, $\times 2000$;
- d) 15 mol % CeO_2 -85 mol % Eu_2O_3 , $\langle\text{C-Eu}_2\text{O}_3\rangle$ basis + $\langle\text{B-Eu}_2\text{O}_3\rangle$ tr., BEI, $\times 2000$;
- e) 20 mol % CeO_2 -80 mol % Eu_2O_3 , $\langle\text{C-Eu}_2\text{O}_3\rangle$, BEI, $\times 2000$;
- f) 25 mol % CeO_2 -75 mol % Eu_2O_3 , $\langle\text{C-Eu}_2\text{O}_3\rangle$, BEI, $\times 2000$;
- g) 30 mol % CeO_2 -70 mol % Eu_2O_3 , $\langle\text{C-Eu}_2\text{O}_3\rangle$ basis + $\langle\text{F-CeO}_2\rangle$ tr., BEI, $\times 2000$;
light phase (texture) - $\langle\text{C-Eu}_2\text{O}_3\rangle$, dark phase - $\langle\text{F-CeO}_2\rangle$, black – pores;
- h) 35 mol % CeO_2 -65 mol % Eu_2O_3 , $\langle\text{C-Eu}_2\text{O}_3\rangle$ + $\langle\text{F-CeO}_2\rangle$, BEI, $\times 2000$;
light phase - $\langle\text{C-Eu}_2\text{O}_3\rangle$, dark gray phases (inclusions) - $\langle\text{F-CeO}_2\rangle$, black – pores;
- i) 40 mol % CeO_2 -60 mol % Eu_2O_3 , $\langle\text{C-Eu}_2\text{O}_3\rangle$ basis + $\langle\text{F-CeO}_2\rangle$ tr., BEI, $\times 2000$;
- j) 45 mol % CeO_2 -55 mol % Eu_2O_3 , $\langle\text{C-Eu}_2\text{O}_3\rangle$ basis + $\langle\text{F-CeO}_2\rangle$ \uparrow , BEI, $\times 2000$;
- k) 50 mol % CeO_2 -50 mol % Eu_2O_3 , $\langle\text{C-Eu}_2\text{O}_3\rangle$ basis + $\langle\text{F-CeO}_2\rangle$ tr. \uparrow , BEI, $\times 2000$;
- l) 55 mol % CeO_2 -45 mol % Eu_2O_3 , $\langle\text{C-Eu}_2\text{O}_3\rangle$ basis + $\langle\text{F-CeO}_2\rangle$ tr. \uparrow , BEI, $\times 2000$;
- m) 60 mol % CeO_2 -40 mol % Eu_2O_3 , $\langle\text{C-Eu}_2\text{O}_3\rangle$ \downarrow + $\langle\text{F-CeO}_2\rangle$ \uparrow , BEI, $\times 2000$;
grains on fracture - $\langle\text{F-CeO}_2\rangle$;
- n) 65 mol % CeO_2 -35 mol % Eu_2O_3 , $\langle\text{F-CeO}_2\rangle$ basis + $\langle\text{C-Eu}_2\text{O}_3\rangle$ \downarrow , BEI, $\times 2000$;
light phase - $\langle\text{C-Eu}_2\text{O}_3\rangle$, dark phase and grains on fractures - $\langle\text{F-CeO}_2\rangle$, black – pores;

The microstructure research data are confirmed by the XRD results (Table. 1. 6). Increase in ceria concentration from 35 to 55 mol% CeO_2 in two-phase samples (C + F) results in the porosity

increase and complication of a relief of the surface, and inhomogeneous phase distribution (Fig. 1.12 h-l). The microstructure of two phase sample containing 60 mol % CeO₂-40 mol% Eu₂O₃ is developing as polyhedral grains of F-CeO₂ of 0.8-9.2 μm in size (Fig. 1.12 m). In the two-phase samples, containing 65-75 mol% CeO₂, the cubic modifications of F-CeO₂ represents the matrix phase (Table. 1.6). Two phases are clearly seen on microstructure: the grains of ceria look like inclusions on the fracture surfaces (Fig. 1.12 n). Note, the higher is the ceria content, the finer become grains of the F-phase.

The size of homogeneity field of the B-Eu₂O₃ solid solution at temperature 1100 °C remains quite small (< 1 mol%). The substitution of ions Eu³⁺ (r = 0.0985 nm) by smaller size ions Ce⁴⁺ (r = 0.090 nm) did not lead to stabilization of the B-Eu₂O₃ and solubility at 1500 °C was not increased. The same sterical factor explains larger expansion of the F-CeO₂ phase field as compared to B-phase field, which remains unchanged in the temperature range 1500-1100 °C of about 20 mol% (Fig. 1.10).

The specificity of the B-Eu₂O₃ microstructure concerns non-isometric grains from 0.42 μm to 6.7 μm long and groups of agglomerates are shown in Fig. 1.13 a. In the sample 1 mol% CeO₂-99 mol% Eu₂O₃, the fine grain two phase structure is observed, where gray phase is the main component - cubic C-Eu₂O₃ confirmed by XRD and petrography data (Table. 1.7). The monoclinic phase of B-Eu₂O₃ looks like rare light inclusions (Figs. 1.13 b). In the one-phase samples containing from 2 to 5 mol% CeO₂ and annealed at 1100 °C, the fine grain structure of C-Eu₂O₃ solid solutions was reported (Figs. 1.13 e-k). The two-phase field (C-Eu₂O₃ + F-CeO₂) exists in the concentration range 10-75 mol% CeO₂ at 1100 °C. In the petrography data, two cubic phases were revealed. The main phase is isotropic C-form of REO, but starting from 25 mol% CeO₂ the amount of another isotropic phase, which is F-CeO₂, starts growing (Fig. 1.13 f). In the samples containing 20 mol% CeO₂-80 mol% Eu₂O₃ and 25 mol% CeO₂-75 mol% Eu₂O₃, the fine grain structure is characterized by oriented stripes-like grains, the chain of grains, which probably belong to another phase and have 4.17-12.5 μm (Fig. 1.13 i,j). Further increasing of ceria content gives much coarser microstructure and porous grains appear (Fig. 1.13 k,l). In the sample containing 40 mol% CeO₂-60 mol% Eu₂O₃, two types of grains found: dark gray grains with smooth surface (F-CeO₂) and light gray grains with rough porous surface (C-Eu₂O₃). The microstructure of samples of the CeO₂-Eu₂O₃ system in the field with high content of ceria after annealing at 1100 °C is shown in Fig. 1.14. In the sample containing 80 mol% CeO₂, two phases are clearly seen. The matrix phase is F-CeO₂ solid solution, but amount of another phase C-Eu₂O₃ decreases (Fig. 1.14 g,h). Further increase of CeO₂ content happens in the solid solution (F-CeO₂) just changing surface morphology. The samples containing 90-95 mol% CeO₂ show fine grain microstructure, which includes grains and agglomerates. (Fig. 1.14 k,l).

The microstructure of some samples of the CeO₂-Eu₂O₃ system as-annealed at 600 °C were studied but no shown here. In spite of extremely durable isothermal exposure for 33061 hours at 600 °C, dense sintered samples were not obtained. Microstructure has been studied using polished and non-polished samples. As a result, the samples are substantially different by morphology and texture as compared to the samples obtained under higher temperatures (1100, 1500 °C). In the samples containing 1 mol% CeO₂-99 mol% Eu₂O₃ and 2 mol% CeO₂-98 mol% Eu₂O₃, one isotropic phase yellowish and porous C-Eu₂O₃ exists by petrography data and confirmed by XRD data and electron microscopy (Table. 1.8). The polyhedral grains of cubic modification (C) of europia are the plate-shape of different size (0.8-11.7 μ). Grain growth occurs by recrystallization in the solid phase. The traces of another isotropic phase <F-CeO₂> but with higher refraction index than for <C-Eu₂O₃> have been found in the sample 3 mol% CeO₂-97 mol% Eu₂O₃. In the electron microscopy images, the matrix phase of light color grains <C-Eu₂O₃> includes dark-phase grains of <F-CeO₂>.

The microstructures of two-phase samples containing from 4 to 45 mol% CeO₂ are representative for <C-Eu₂O₃>, where this phase is the main one. Further increase of ceria in the composition corresponds to decreasing of <C-Eu₂O₃> grains and increasing of <F-CeO₂> grains. In

the samples containing 75-85 mol % CeO_2 , the main phase becomes $\langle\text{F-CeO}_2\rangle$ (Table. 1.8). The boundary solubility of Eu_2O_3 in cubic phase F-CeO_2 at temperature 600 °C achieves 10 mol%. The lattice parameters increases from $a=0.5409$ nm for pure CeO_2 to $a=0.5418$ nm (600 °C) in boundary solid solution.

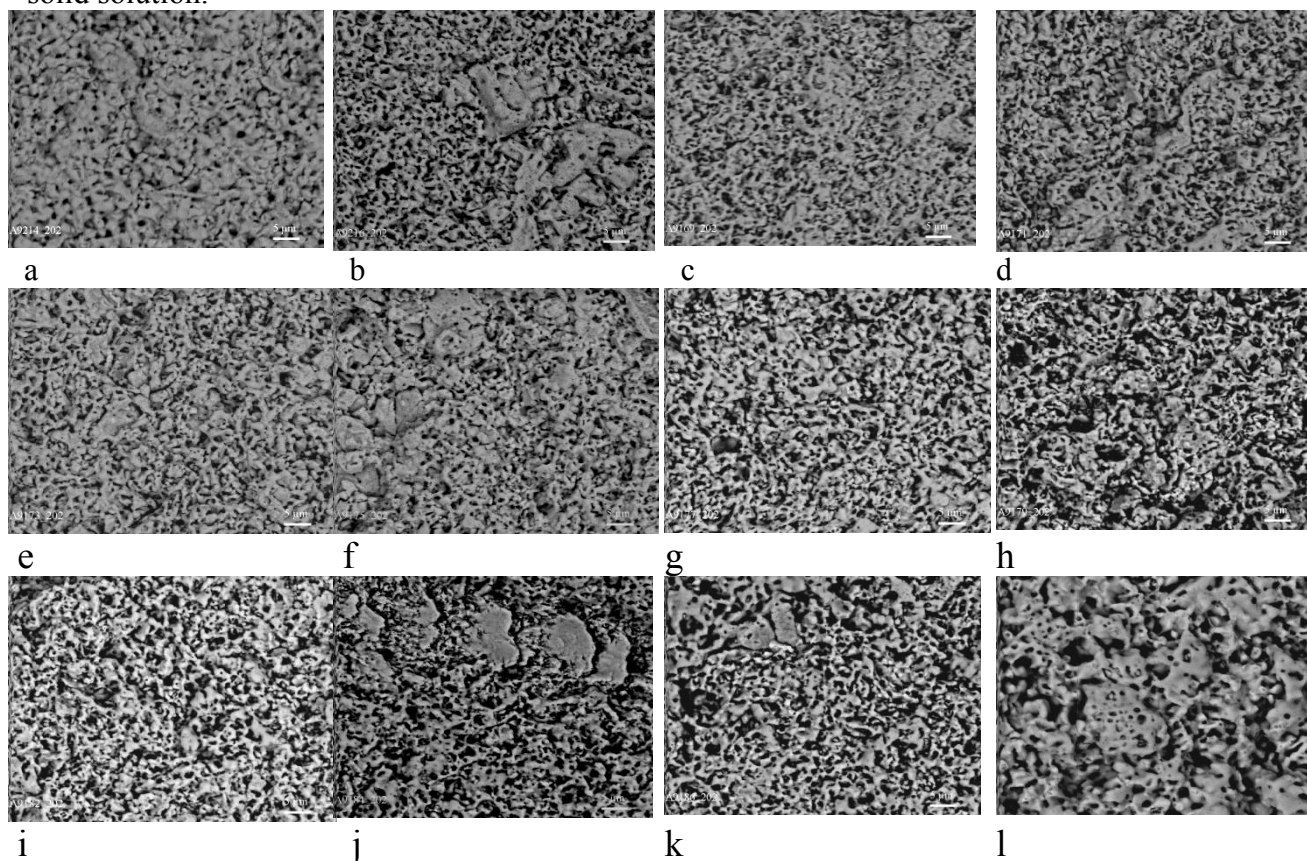


Fig 1.13 - Microstructure of the samples of the system $\text{CeO}_2\text{-Eu}_2\text{O}_3$ in the field with high amount of europia after annealing at 1100 °C:

- a) 100 mol % Eu_2O_3 , $\langle\text{B-Eu}_2\text{O}_3\rangle$, BEI, $\times 2000$; gray - $\langle\text{C-Eu}_2\text{O}_3\rangle$;
 - b) 1 mol% CeO_2 -99 mol% Eu_2O_3 , $\langle\text{C-Eu}_2\text{O}_3\rangle$ basis + $\langle\text{B-Eu}_2\text{O}_3\rangle$ tr. I, BEI, $\times 2000$;
 - c) 2 mol% CeO_2 -98 mol% Eu_2O_3 , $\langle\text{C-Eu}_2\text{O}_3\rangle$, BEI, $\times 2000$;
 - d) 3 mol% CeO_2 -97 mol% Eu_2O_3 , $\langle\text{C-Eu}_2\text{O}_3\rangle$, BEI, $\times 2000$;
 - e) 4 mol% CeO_2 -96 mol% Eu_2O_3 , $\langle\text{C-Eu}_2\text{O}_3\rangle$, BEI, $\times 2000$;
 - f) 5 mol% CeO_2 -95 mol% Eu_2O_3 , $\langle\text{C-Eu}_2\text{O}_3\rangle$, BEI, $\times 2000$;
 - g) 10 mol% CeO_2 -90 mol% Eu_2O_3 , $\langle\text{C-Eu}_2\text{O}_3\rangle$ basis + $\langle\text{F-CeO}_2\rangle$ tr., BEI, $\times 2000$;
 - h) 15 mol% CeO_2 -85 mol% Eu_2O_3 , $\langle\text{C-Eu}_2\text{O}_3\rangle$ basis + $\langle\text{F-CeO}_2\rangle$, BEI, $\times 2000$;
 - i) 20 mol% CeO_2 -80 mol% Eu_2O_3 , $\langle\text{C-Eu}_2\text{O}_3\rangle$ basis + $\langle\text{F-CeO}_2\rangle$, BEI, $\times 2000$;
 - j) 25 mol% CeO_2 -75 mol% Eu_2O_3 , $\langle\text{C-Eu}_2\text{O}_3\rangle$ basis + $\langle\text{F-CeO}_2\rangle$ \uparrow , BEI, $\times 2000$;
 - k) 30 mol% CeO_2 -70 mol% Eu_2O_3 , $\langle\text{C-Eu}_2\text{O}_3\rangle$ basis + $\langle\text{F-CeO}_2\rangle$, BEI, $\times 2000$;
 - l) 35 mol% CeO_2 -65 mol% Eu_2O_3 , $\langle\text{C-Eu}_2\text{O}_3\rangle$ + $\langle\text{F-CeO}_2\rangle$, BEI, $\times 2000$;
- light phase - $\langle\text{C-Eu}_2\text{O}_3\rangle$, dark gray phase - $\langle\text{F-CeO}_2\rangle$, black – pores;

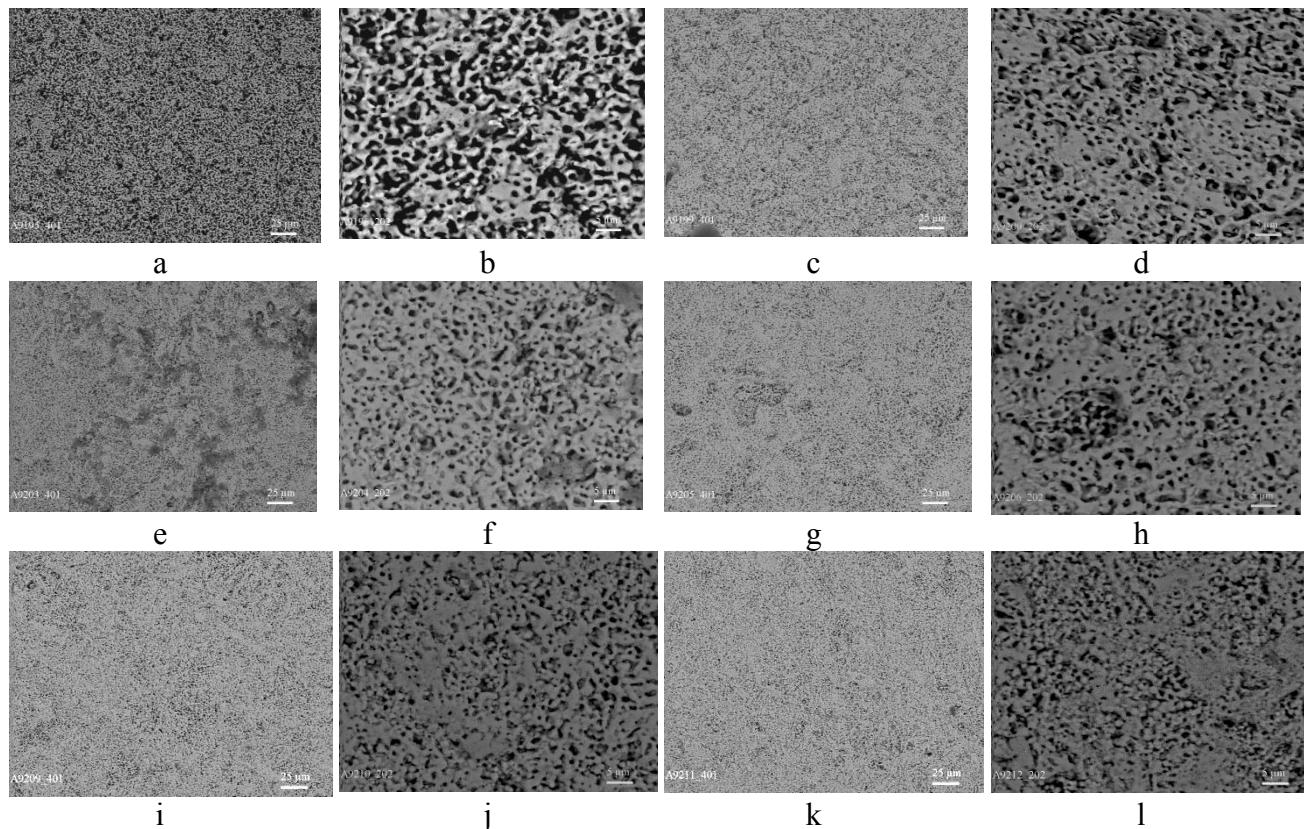


Fig. 1.14 - Microstructure of samples in the $\text{CeO}_2\text{-Eu}_2\text{O}_3$ system in the field of high ceria content after annealing at 1100 °C:

- a) 55 mol % CeO_2 -45 mol % Eu_2O_3 , $\langle\text{C-Eu}_2\text{O}_3\rangle \downarrow + \langle\text{F-CeO}_2\rangle \text{ tr. } \uparrow$, BEI, $\times 400$;
- b) 55 mol % CeO_2 -45 mol % Eu_2O_3 , $\langle\text{C-Eu}_2\text{O}_3\rangle \downarrow + \langle\text{F-CeO}_2\rangle \text{ tr. } \uparrow$, BEI, $\times 2000$;
- c) 65 mol % CeO_2 -35 mol % Eu_2O_3 , $\langle\text{F-CeO}_2\rangle$ basis $\uparrow + \langle\text{C-Eu}_2\text{O}_3\rangle \downarrow\downarrow$, BEI, $\times 400$;
- d) 65 mol % CeO_2 -35 mol % Eu_2O_3 , $\langle\text{F-CeO}_2\rangle$ basis $\uparrow + \langle\text{C-Eu}_2\text{O}_3\rangle \downarrow\downarrow$, BEI, $\times 2000$;
- e) 75 mol % CeO_2 -25 mol % Eu_2O_3 , $\langle\text{F-CeO}_2\rangle + \langle\text{C-Eu}_2\text{O}_3\rangle$, BEI, $\times 400$;
- f) 75 mol % CeO_2 -25 mol % Eu_2O_3 , $\langle\text{F-CeO}_2\rangle + \langle\text{C-Eu}_2\text{O}_3\rangle$, BEI, $\times 2000$;
- g) 80 mol % CeO_2 -20 mol % Eu_2O_3 , $\langle\text{F-CeO}_2\rangle + \langle\text{C-Eu}_2\text{O}_3\rangle \downarrow$, BEI, $\times 400$;
- h) 80 mol % CeO_2 -20 mol % Eu_2O_3 , $\langle\text{F-CeO}_2\rangle + \langle\text{C-Eu}_2\text{O}_3\rangle \downarrow$, BEI, $\times 2000$;
- i) 90 mol % CeO_2 -10 mol % Eu_2O_3 , $\langle\text{F-CeO}_2\rangle$, BEI, $\times 400$;
- j) 90 mol % CeO_2 -10 mol % Eu_2O_3 , $\langle\text{F-CeO}_2\rangle$, BEI, $\times 2000$;
- k) 95 mol % CeO_2 -5 mol % Eu_2O_3 , $\langle\text{F-CeO}_2\rangle$, BEI, $\times 400$;
- l) 95 mol % CeO_2 -5 mol % Eu_2O_3 , $\langle\text{F-CeO}_2\rangle$, BEI, $\times 2000$.

Isothermal section of the phase diagram in the $\text{ZrO}_2\text{-CeO}_2\text{-Eu}_2\text{O}_3$ system at temperature of 1500 °C

In the ternary system $\text{ZrO}_2\text{-CeO}_2\text{-Eu}_2\text{O}_3$ at 1500 °C, no new phases were found. The character of phase equilibria in this system is completely determined by constitution of boundary binary system. At 1500 °C in the $\text{ZrO}_2\text{-CeO}_2\text{-Eu}_2\text{O}_3$ system the following one-phase fields of solid solutions have been established: tetragonal (T) and cubic (F) of fluorite type ZrO_2 , monoclinic (B) and cubic (C) modifications of Eu_2O_3 , cubic phase of fluorite-type (F) CeO_2 and the ordered pyrochlore-type phase of $\text{Eu}_2\text{Zr}_2\text{O}_7$ (Py).

Obtained results allowed developing a isothermal section for the $\text{ZrO}_2\text{-CeO}_2\text{-Eu}_2\text{O}_3$ system at 1500 °C (Fig. 1.15). The input chemical compositions and phase compositions of the samples

annealed at 1500 °C, lattice parameters of equilibrium phases at given temperatures, are presented in Table 1.10.

Table 1.10 – Chemical and phase composition, lattice parameters of phases in the ZrO₂-CeO₂-Eu₂O₃ system after annealing at 1500 °C, 150 hour. (XRD, petrography and microscopy data)

Chemical composition, mol. %			Phase compositions and parameters of elementary cells, nm ($a \pm 0.0002$)
ZrO ₂	CeO ₂	Eu ₂ O ₃	
1	2	3	4
<u>Section ZrO₂ - (50 mol % CeO₂ - 50 mol % Eu₂O₃)</u>			
5	47.5	47.5	<F-CeO ₂ > ($a = 0.5432$) + <C-Eu ₂ O ₃ > ($a = 1.0864$)
10	45	45	<F-CeO ₂ > ($a = 0.5397$) + <C-Eu ₂ O ₃ > ($a = 1.0794$)
15	42.5	42.5	<F-CeO ₂ > ($a = 0.5409$) + <C-Eu ₂ O ₃ > ($a = 1.0827$)
20	40	40	<F-CeO ₂ > ($a = 0.5392$) + <C-Eu ₂ O ₃ > ($a = 1.0807$)
25	37.5	37.5	<F-CeO ₂ > ($a = 0.5411$) + <C-Eu ₂ O ₃ > ($a = 1.0827$)
30	35	35	<F-CeO ₂ > ($a = 0.5370$) + <C-Eu ₂ O ₃ > ($a = 1.0743$)
35	32.5	32.5	<F-CeO ₂ > ($a = 0.5350$) + <C-Eu ₂ O ₃ > ($a = 1.0805$) + Py tr
40	30	30	<F-CeO ₂ > + <C-Eu ₂ O ₃ > ($a = 1.0894$) + Py
45	27.5	27.5	<F-CeO ₂ > + <C-Eu ₂ O ₃ > + Py
50	25	25	<F-CeO ₂ > + <C-Eu ₂ O ₃ > + Py
55	22.5	22.5	<F-CeO ₂ > + Py + <C-Eu ₂ O ₃ > tr
60	20	20	<F-CeO ₂ > + Py
65	17.5	17.5	<F-ZrO ₂ > + Py + <T-ZrO ₂ >*tr
70	15	15	<F-ZrO ₂ > basis + Py + <T-ZrO ₂ >*tr
75	12.5	12.5	<F-ZrO ₂ > basis + Py + <T-ZrO ₂ >* tr
80	10	10	Py basis + <T-ZrO ₂ >*↑
85	7.5	7.5	<F-ZrO ₂ > basis + <T-ZrO ₂ >*↑ + Py
90	5	5	<F-ZrO ₂ > + <T-ZrO ₂ >* basis↑
95	2.5	2.5	<F-ZrO ₂ > + <T-ZrO ₂ >* basis↑↑
96	2	2	<F-ZrO ₂ > + <T-ZrO ₂ >* basis↑↑
97	1.5	1.5	<T-ZrO ₂ >* basis + <F-ZrO ₂ >
98	1	1	<T-ZrO ₂ >* basis + <F-ZrO ₂ >↓
99	0.5	0.5	<T-ZrO ₂ >*
<u>Section CeO₂ - (67 mol % ZrO₂ - 33 mol % Eu₂O₃)</u>			
66	1	33	Py (Eu ₂ Zr ₂ O ₇)
65	2	33	Py + <F-ZrO ₂ >
64	3	33	Py + <F-ZrO ₂ >
64	4	32	Py + <F-ZrO ₂ >
63	5	32	Py + <F-ZrO ₂ > + <C-Eu ₂ O ₃ > tr
60	10	30	Py + <F-CeO ₂ > + <C-Eu ₂ O ₃ > tr
57	15	28	Py + <F-CeO ₂ > + <C-Eu ₂ O ₃ >
53	20	27	<F-CeO ₂ > + Py + <C-Eu ₂ O ₃ >
47	30	23	<F-CeO ₂ > + Py + <C-Eu ₂ O ₃ >
44	35	21	<F-CeO ₂ > + Py + <C-Eu ₂ O ₃ >
40	40	20	<F-CeO ₂ > + Py + <C-Eu ₂ O ₃ >
37	45	18	<F-CeO ₂ > ($a = 0.5319$) + Py + <C-Eu ₂ O ₃ >
34	50	16	<F-CeO ₂ > ($a = 0.5322$) + <C-Eu ₂ O ₃ >
30	55	15	<F-CeO ₂ > ($a = 0.5336$) + <C-Eu ₂ O ₃ >
26	60	14	<F-CeO ₂ > ($a = 0.5356$) + <C-Eu ₂ O ₃ >
23	65	12	<F-CeO ₂ > ($a = 0.5368$) + <C-Eu ₂ O ₃ >
20	70	10	<F-CeO ₂ > ($a = 0.5369$) + <C-Eu ₂ O ₃ > tr
17	75	8	<F-CeO ₂ > ($a = 0.5374$) + <C-Eu ₂ O ₃ > tr
13.5	80	6.5	<F-CeO ₂ > ($a = 0.5374$)
10	85	5	<F-CeO ₂ > ($a = 0.5386$)

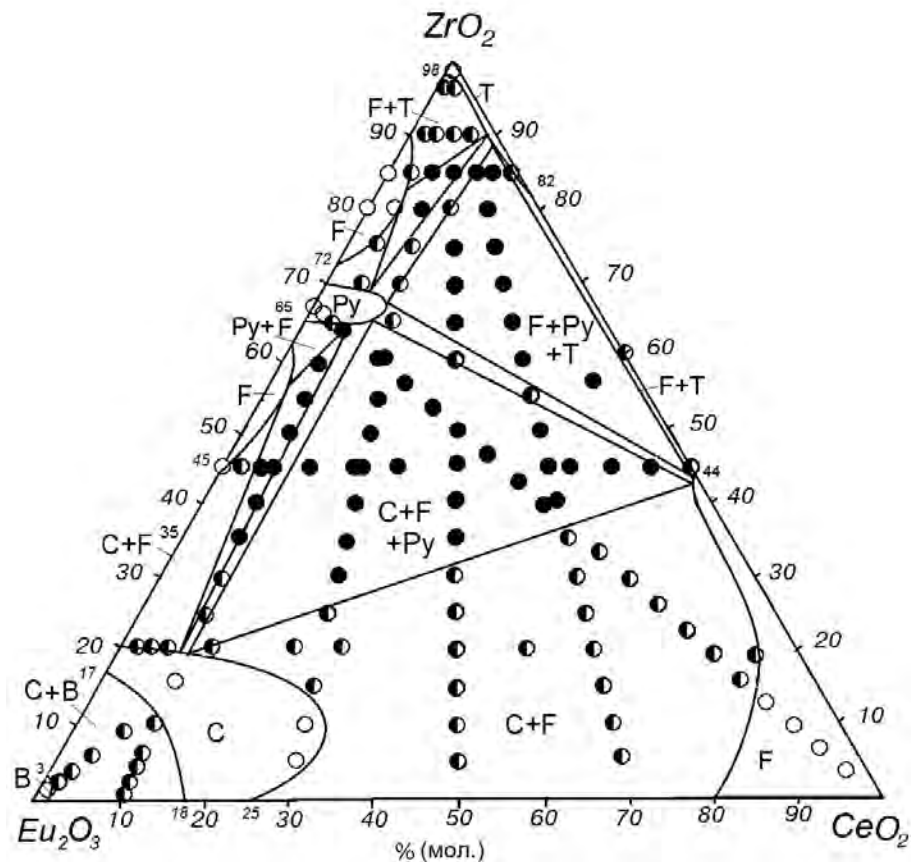
1	2	3	4
7	90	3	$\langle \text{F-CeO}_2 \rangle$ ($a = 0.5390$)
3	95	2	$\langle \text{F-CeO}_2 \rangle$ ($a = 0.5397$)
<u>Section ZrO_2 - (30 mol % CeO_2 - 70 mol % Eu_2O_3)</u>			
5	29	66	$\langle \text{C-Eu}_2\text{O}_3 \rangle$ basis ($a = 1.0849$)
10	27	63	$\langle \text{C-Eu}_2\text{O}_3 \rangle$ basis ($a = 1.0819$)
15	25.5	59.5	$\langle \text{C-Eu}_2\text{O}_3 \rangle$ basis ($a = 1.0802$) + $\langle \text{F-CeO}_2 \rangle$
25	22	53	$\langle \text{C-Eu}_2\text{O}_3 \rangle$ ($a = 1.0737$) + $\langle \text{F-CeO}_2 \rangle$
30	21	49	$\langle \text{C-Eu}_2\text{O}_3 \rangle \downarrow$ ($a = 1.0738$) + $\langle \text{F-CeO}_2 \rangle \uparrow$ + Py tr
40	18	42	$\langle \text{C-Eu}_2\text{O}_3 \rangle \downarrow$ ($a = 1.0672$) + $\langle \text{F-CeO}_2 \rangle \uparrow \uparrow$ + Py tr
45	16.5	38.5	$\langle \text{C-Eu}_2\text{O}_3 \rangle \downarrow$ ($a = 1.0657$) + $\langle \text{F-CeO}_2 \rangle \uparrow \uparrow$ + Py tr
50	15	35	$\langle \text{C-Eu}_2\text{O}_3 \rangle \downarrow$ ($a = 1.0621$) + $\langle \text{F-CeO}_2 \rangle \uparrow \uparrow$ + Py
55	13.5	31.5	$\langle \text{C-Eu}_2\text{O}_3 \rangle \downarrow$ ($a = 1.0580$) + $\langle \text{F-CeO}_2 \rangle \uparrow \uparrow$ + Py
65	10	25	$\langle \text{F-CeO}_2 \rangle$ + Py \uparrow
70	9	21	Py $\uparrow \uparrow$ + $\langle \text{T-ZrO}_2 \rangle$
75	8.5	16.5	Py basis + $\langle \text{T-ZrO}_2 \rangle$
80	6	14	$\langle \text{F-ZrO}_2 \rangle$ + Py + $\langle \text{T-ZrO}_2 \rangle$
85	5.5	9.5	$\langle \text{F-ZrO}_2 \rangle$ + $\langle \text{T-ZrO}_2 \rangle^*$ + Py tr
90	3	7	$\langle \text{F-ZrO}_2 \rangle$ + $\langle \text{T-ZrO}_2 \rangle^*$
<u>Section ZrO_2 - (70 mol % CeO_2 - 30 mol % Eu_2O_3)</u>			
5	66	29	$\langle \text{F-CeO}_2 \rangle$ basis + $\langle \text{C-Eu}_2\text{O}_3 \rangle$ tr
10	63	27	$\langle \text{F-CeO}_2 \rangle$ basis + $\langle \text{C-Eu}_2\text{O}_3 \rangle$ tr
15	59.5	25.5	$\langle \text{F-CeO}_2 \rangle$ basis + $\langle \text{C-Eu}_2\text{O}_3 \rangle$
25	53	22	$\langle \text{F-CeO}_2 \rangle$ basis + $\langle \text{C-Eu}_2\text{O}_3 \rangle$
30	49	21	$\langle \text{F-CeO}_2 \rangle$ basis + $\langle \text{C-Eu}_2\text{O}_3 \rangle$ tr
40	42	18	$\langle \text{F-CeO}_2 \rangle$ basis + $\langle \text{C-Eu}_2\text{O}_3 \rangle$ tr + Py
45	38.5	16.5	Py basis + $\langle \text{F-CeO}_2 \rangle$ + $\langle \text{C-Eu}_2\text{O}_3 \rangle$ tr
50	35	15	Py basis + $\langle \text{F-CeO}_2 \rangle$ + $\langle \text{C-Eu}_2\text{O}_3 \rangle$ tr
55	31.5	13.5	Py basis + $\langle \text{F-CeO}_2 \rangle$
65	25	10	Py + $\langle \text{F-CeO}_2 \rangle$ + $\langle \text{T-ZrO}_2 \rangle^*$ tr
70	21	9	Py + $\langle \text{F-CeO}_2 \rangle$ + $\langle \text{T-ZrO}_2 \rangle^*$ tr
75	16.5	8.5	Py + $\langle \text{F-CeO}_2 \rangle$ + $\langle \text{T-ZrO}_2 \rangle^*$ tr
80	14	6	Py + $\langle \text{F-CeO}_2 \rangle$ basis + $\langle \text{T-ZrO}_2 \rangle^*$ tr
85	9.5	5.5	$\langle \text{F-CeO}_2 \rangle$ + $\langle \text{T-ZrO}_2 \rangle^*$ \uparrow + Py
90	7	3	$\langle \text{F-ZrO}_2 \rangle \downarrow$ + $\langle \text{T-ZrO}_2 \rangle^* \uparrow \uparrow$
<u>Section ZrO_2 - (10 mol % CeO_2 - 90 mol % Eu_2O_3)</u>			
2	10	88	$\langle \text{C-Eu}_2\text{O}_3 \rangle$ ($a = 1.0847$) + $\langle \text{B-Eu}_2\text{O}_3 \rangle$
3	10	87	$\langle \text{C-Eu}_2\text{O}_3 \rangle$ basis ($a = 1.0844$) + $\langle \text{B-Eu}_2\text{O}_3 \rangle$
4	9.5	86.5	$\langle \text{C-Eu}_2\text{O}_3 \rangle$ basis ($a = 1.0847$) + $\langle \text{B-Eu}_2\text{O}_3 \rangle$
5	9.5	85.5	$\langle \text{C-Eu}_2\text{O}_3 \rangle$ basis ($a = 1.0829$) + $\langle \text{B-Eu}_2\text{O}_3 \rangle$
10	9.5	80.5	$\langle \text{C-Eu}_2\text{O}_3 \rangle$ basis ($a = 1.0831$) + $\langle \text{B-Eu}_2\text{O}_3 \rangle$ tr \downarrow
15	9	76	$\langle \text{C-Eu}_2\text{O}_3 \rangle$ ($a = 1.0806$)
25	8.5	66.5	$\langle \text{C-Eu}_2\text{O}_3 \rangle$ ($a = 1.0786$) + Py
30	8	62	$\langle \text{C-Eu}_2\text{O}_3 \rangle$ ($a = 1.0763$) + Py \uparrow
35	8	57	$\langle \text{C-Eu}_2\text{O}_3 \rangle \downarrow$ ($a = 1.0812$) + $\langle \text{F-ZrO}_2 \rangle \uparrow$ + Py
40	7	53	$\langle \text{C-Eu}_2\text{O}_3 \rangle \downarrow$ + $\langle \text{F-ZrO}_2 \rangle$ + Py
45	6.5	48.5	$\langle \text{C-Eu}_2\text{O}_3 \rangle$ tr $\downarrow \downarrow$ + $\langle \text{F-ZrO}_2 \rangle$ + Py
50	6	44	$\langle \text{C-Eu}_2\text{O}_3 \rangle$ tr $\downarrow \downarrow$ + $\langle \text{F-ZrO}_2 \rangle$ + Py
55	5.5	39.5	$\langle \text{C-Eu}_2\text{O}_3 \rangle$ tr $\downarrow \downarrow$ + $\langle \text{F-ZrO}_2 \rangle$ + Py
60	5	35	$\langle \text{C-Eu}_2\text{O}_3 \rangle$ tr $\downarrow \downarrow$ + $\langle \text{F-ZrO}_2 \rangle$ + Py
70	4	26	$\langle \text{F-ZrO}_2 \rangle$ + Py
75	3	22	$\langle \text{F-ZrO}_2 \rangle$ + Py
80	2.5	17.5	$\langle \text{F-ZrO}_2 \rangle$
85	1.5	13.5	$\langle \text{F-ZrO}_2 \rangle$ basis + $\langle \text{T-ZrO}_2 \rangle^*$

1	2	3	4
90	1.5	8.5	$\langle \text{T-ZrO}_2 \rangle^* + \langle \text{F-ZrO}_2 \rangle$
			<u>Section Eu_2O_3- (60 mol % ZrO_2 - 40 mol % CeO_2)</u>
60	40	0	$\langle \text{T-ZrO}_2 \rangle^{**} + \langle \text{F-CeO}_2 \rangle$
57	38	5	$\langle \text{F-CeO}_2 \rangle + \text{Py} + \langle \text{T-ZrO}_2 \rangle$
53.5	36.5	10	$\langle \text{F-CeO}_2 \rangle + \text{Py}$
39.5	25.5	35	$\langle \text{F-CeO}_2 \rangle + \langle \text{C-Eu}_2\text{O}_3 \rangle + \text{Py}$
36	24	40	$\langle \text{F-CeO}_2 \rangle + \langle \text{C-Eu}_2\text{O}_3 \rangle + \text{Py}$
9.5	5.5	85	$\langle \text{B-Eu}_2\text{O}_3 \rangle + \langle \text{C-Eu}_2\text{O}_3 \rangle$
6	4	90	$\langle \text{B-Eu}_2\text{O}_3 \rangle + \langle \text{C-Eu}_2\text{O}_3 \rangle$
3	2	95	$\langle \text{B-Eu}_2\text{O}_3 \rangle + \langle \text{C-Eu}_2\text{O}_3 \rangle$
2.5	1.5	96	$\langle \text{B-Eu}_2\text{O}_3 \rangle + \langle \text{C-Eu}_2\text{O}_3 \rangle$
2	1	97	$\langle \text{B-Eu}_2\text{O}_3 \rangle + \langle \text{C-Eu}_2\text{O}_3 \rangle$
1.5	0.5	98	$\langle \text{B-Eu}_2\text{O}_3 \rangle + \langle \text{C-Eu}_2\text{O}_3 \rangle \downarrow$
0.5	0.5	99	$\langle \text{B-Eu}_2\text{O}_3 \rangle + \langle \text{C-Eu}_2\text{O}_3 \rangle \text{ tr } \downarrow \downarrow$
			<u>Iso-concentration line 20 mol % ZrO_2</u>
20	1	79	$\langle \text{C-Eu}_2\text{O}_3 \rangle + \langle \text{F-ZrO}_2 \rangle$
20	2	78	$\langle \text{C-Eu}_2\text{O}_3 \rangle + \langle \text{F-ZrO}_2 \rangle$
20	3	77	$\langle \text{C-Eu}_2\text{O}_3 \rangle \text{ basis} + \langle \text{F-ZrO}_2 \rangle$
20	4	76	$\langle \text{C-Eu}_2\text{O}_3 \rangle + \langle \text{F-ZrO}_2 \rangle$
20	10	70	$\langle \text{C-Eu}_2\text{O}_3 \rangle + \langle \text{F-CeO}_2 \rangle$
20	20	60	$\langle \text{C-Eu}_2\text{O}_3 \rangle + \langle \text{F-CeO}_2 \rangle$
20	25	55	$\langle \text{C-Eu}_2\text{O}_3 \rangle + \langle \text{F-CeO}_2 \rangle$
20	30	50	$\langle \text{C-Eu}_2\text{O}_3 \rangle + \langle \text{F-CeO}_2 \rangle \text{ basis}$
20	35	45	$\langle \text{C-Eu}_2\text{O}_3 \rangle + \langle \text{F-CeO}_2 \rangle$
20	45	35	$\langle \text{C-Eu}_2\text{O}_3 \rangle + \langle \text{F-CeO}_2 \rangle$
20	55	25	$\langle \text{C-Eu}_2\text{O}_3 \rangle + \langle \text{F-CeO}_2 \rangle$
20	65	15	$\langle \text{C-Eu}_2\text{O}_3 \rangle + \langle \text{F-CeO}_2 \rangle$
20	75	5	$\langle \text{C-Eu}_2\text{O}_3 \rangle + \langle \text{F-CeO}_2 \rangle$
20	80	0	$\langle \text{F-CeO}_2 \rangle$
			<u>Iso-concentration line 45 mol % ZrO_2</u>
45	1	54	-
45	2	53	$\langle \text{F-ZrO}_2 \rangle + \langle \text{C-Eu}_2\text{O}_3 \rangle$
45	3	62	$\langle \text{F-ZrO}_2 \rangle + \langle \text{C-Eu}_2\text{O}_3 \rangle$
45	4	51	$\langle \text{F-ZrO}_2 \rangle + \langle \text{C-Eu}_2\text{O}_3 \rangle$
45	5	50	$\langle \text{F-ZrO}_2 \rangle + \langle \text{C-Eu}_2\text{O}_3 \rangle + \text{Py tr}$
45	20	35	$\langle \text{F-CeO}_2 \rangle + \langle \text{C-Eu}_2\text{O}_3 \rangle \text{ tr} + \text{Py tr}$
45	45	10	$\langle \text{F-CeO}_2 \rangle + \langle \text{C-Eu}_2\text{O}_3 \rangle \text{ tr} + \text{Py tr}$
45	50	5	$\langle \text{F-CeO}_2 \rangle + \langle \text{C-Eu}_2\text{O}_3 \rangle \text{ tr} + \text{Py tr}$
45	55	0	$\langle \text{F-ZrO}_2 \rangle + \langle \text{T-ZrO}_2 \rangle^*$
			<u>Iso-concentration line 85 mol % ZrO_2</u>
85	0	15	$\langle \text{F-ZrO}_2 \rangle$
85	11	4	$\langle \text{F-CeO}_2 \rangle + \langle \text{T-ZrO}_2 \rangle^* + \text{Py tr}$
85	12	3	$\langle \text{F-CeO}_2 \rangle + \langle \text{T-ZrO}_2 \rangle^* + \text{Py tr}$
85	13	2	$\langle \text{F-CeO}_2 \rangle \downarrow + \langle \text{T-ZrO}_2 \rangle^{**\uparrow} + \text{Py tr} \downarrow$
85	14	1	$\langle \text{F-CeO}_2 \rangle \downarrow \downarrow + \langle \text{T-ZrO}_2 \rangle^{**} \text{ basis} \uparrow$
85	15	0	$\langle \text{T-ZrO}_2 \rangle^{**}$

* Under given conditions ($T=1500^\circ\text{C}$, 150 hours, in air, slow cooling) tetragonal phase T-ZrO_2 is not stable, The monoclinic phase M-ZrO_2 is stable instead;

** Partial stabilization of T-ZrO_2 observed.

To determine the coordinates of the boundaries for the phase fields the concentration dependences of the lattice parameters were calculated (Fig. 1.16-1.18).



(○ – one-phase, ◐ - two-phase, ● – three-phase)

Fig. 1.15 – Isothermal cross section of the phase diagram $\text{ZrO}_2\text{-CeO}_2\text{-Eu}_2\text{O}_3$ at temperature 1500 °C Using the calculated lattice parameters of the pyrochlore phase Py in the ternary fields, and data of XRD and electron microscopy, the coordinates of configurative points for Py-phase – tops of tie-line triangles (Py+T+F-CeO₂), (Py+T+F-ZrO₂), (Py+C+F-ZrO₂) and (Py+C+F-CeO₂) were determined (Table. 1.11).

Table 1.11 - Coordinates of the tie-line triangles in the system $\text{ZrO}_2\text{-CeO}_2\text{-Eu}_2\text{O}_3$ after annealing at 1500 °C

Phase field	Coordinates of the tie-line triangles, mol. %									
	T		Py		F-CeO ₂		F-ZrO ₂		C	
	ZrO ₂	CeO ₂	ZrO ₂	CeO ₂	ZrO ₂	CeO ₂	ZrO ₂	CeO ₂	ZrO ₂	CeO ₂
Py+T+F-CeO ₂	88	10	67	7	43	56	-	-	-	-
Py+T+F-ZrO ₂	90	8	68	5	-	-	83	3	-	-
Py+C+F-ZrO ₂	-	-	65	5	-	-	57	2	19	6
Py+C+F-CeO ₂	-	-	66	10	42	56	-	-	19	8

The typical microstructures of the samples which are in the different phase fields of the diagram of the $\text{ZrO}_2\text{-CeO}_2\text{-Eu}_2\text{O}_3$ system at 1500 °C are plotted on the Fig. 1.19,1.20.

Seven homogeneity fields of solid solutions were determined at 1500 °C: T- and F-form of ZrO_2 , F-CeO₂, C- and B-Eu₂O₃, as well as intermediate europium zirconate $\text{Eu}_2\text{Zr}_2\text{O}_7$ (Py). The phase equilibria in this system were shown to describe reactions in solid state only.

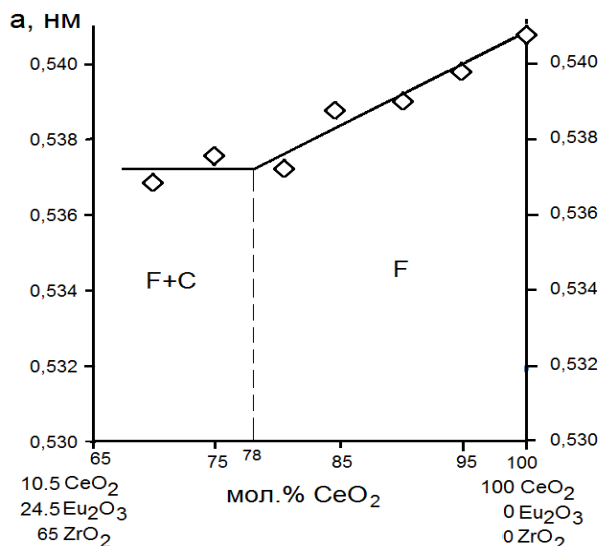


Fig. 1.16 – Concentration dependence of lattice parameter for solid solutions of fluorite type (F-CeO₂, ◇) by the section CeO₂ - (67 mol % ZrO₂ - 33 mol % Eu₂O₃) in the system ZrO₂-CeO₂- Eu₂O₃ after annealing at 1500 °C

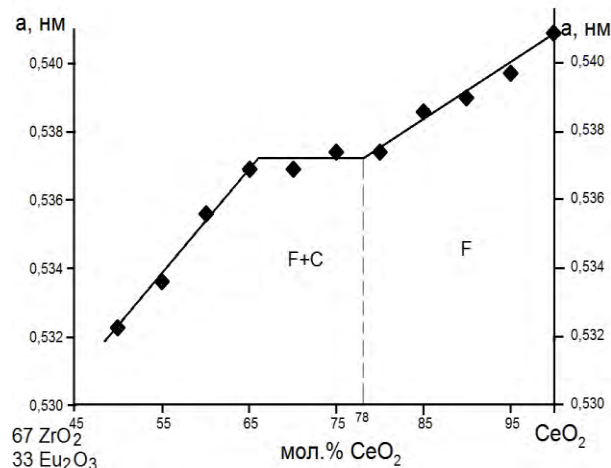


Fig. 1.16a - Concentration dependence of lattice parameter for solid solutions of fluorite type (F-CeO₂, ◆) by the section of CeO₂ - (67 mol % ZrO₂ - 33 mol % Eu₂O₃) in the system ZrO₂-CeO₂- Eu₂O₃ after annealing at 1500 °C

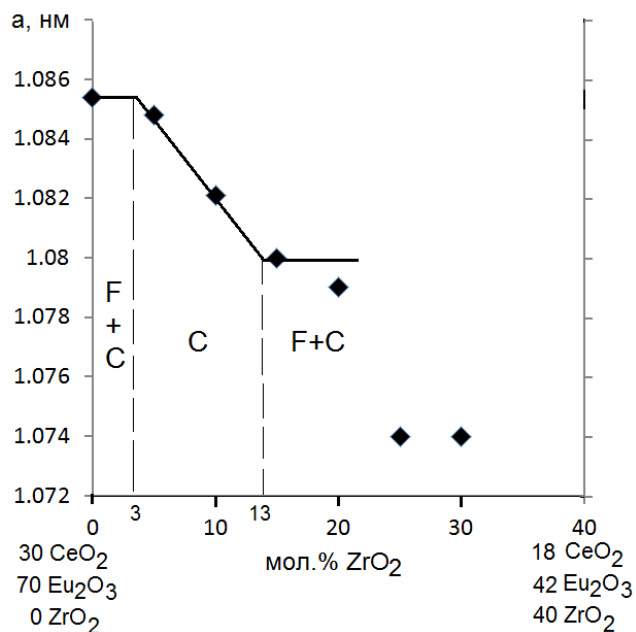


Fig. 1.17 - Concentration dependence of lattice parameter for solid solutions of the C type of REO (C-Eu₂O₃, ◆) by section ZrO₂ - (30 mol % CeO₂ - 70 mol % Eu₂O₃) in the system ZrO₂-CeO₂-Eu₂O₃ after annealing at 1500 °C

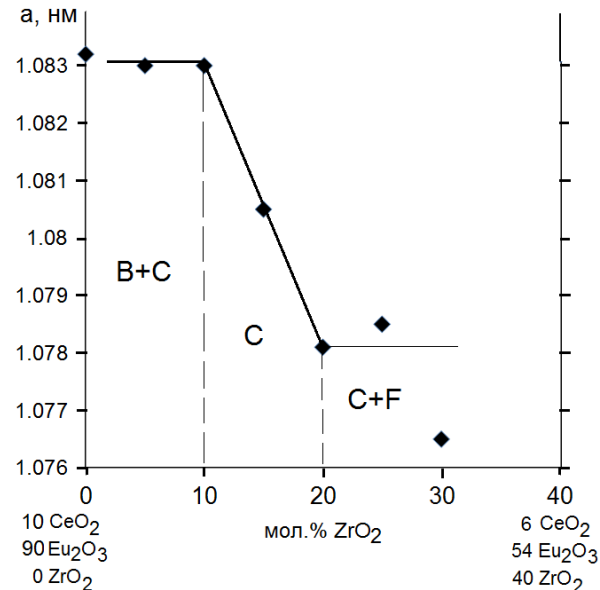


Fig. 1.18 - Concentration dependence of lattice parameter for solid solutions of C type REO (C-Eu₂O₃, ◆) by the section of ZrO₂ - (10 mol % CeO₂ - 90 mol % Eu₂O₃) in the system ZrO₂-CeO₂-Eu₂O₃ after annealing at 1500 °C

In the area of high zirconia content, the solid solutions based on tetragonal modification of ZrO₂, cubic pyrochlore-type phase Eu₂Zr₂O₇ and cubic fluorite-type phases based on zirconia and ceria. The narrow field of tetragonal zirconia solid solutions is drawn out the boundary binary system ZrO₂-CeO₂ (0-18 mol% CeO₂). The solubility of Eu₂O₃ in the T-ZrO₂ is limited, about 1 mol %, which is confirmed by XRD data. The boundary of the homogeneity field of the solid solution based on tetragonal T-ZrO₂ at 1500 °C goes close to the following samples: 98 mol%

ZrO₂-1 mol % CeO₂-1 mol % Eu₂O₃, 90 mol % ZrO₂-7 mol % CeO₂-3 mol % Eu₂O₃, 85 mol % ZrO₂-14 mol % CeO₂-1 mol % Eu₂O₃ – two-phase (T + F), 85 mol % ZrO₂-9.5 mol % CeO₂-5.5 mol % Eu₂O₃ – three-phase (T+F+Py). In the ternary system, ceria and europia dissolve in the tetragonal zirconia approximately in the same amount as in the boundary binary systems ZrO₂-Eu₂O₃ and ZrO₂-CeO₂. It is worth noting, that the solid solutions based on T- ZrO₂ cannot be fixed on quenching at any cooling rates. The x-ray diffraction patterns recorded at room temperatures show lines, attributed to M-ZrO₂. Для ряду складів спостерігали The partial stabilization of T-phase has been observed in a number of samples (Table. 1.10). Fully stabilized tetragonal phase T- ZrO₂ was found in the two and three phase samples along the section ZrO₂ - (70 mol % CeO₂ - 30 mol % Eu₂O₃) or in the samples containing 70 mol % ZrO₂-9 mol % CeO₂-21 mol % Eu₂O₃, 75 mol % ZrO₂-8.5 mol % CeO₂-16.5 mol % Eu₂O₃, 80 mol % ZrO₂-6 mol % CeO₂-14 mol % Eu₂O₃.

Petrography allows revealing the phase transitions due to polysynthetic twinning. Microstructure of the solid solutions based on T* - zirconia for sample containing 99 mol % ZrO₂-0.5 mol % CeO₂-0.5 mol % Eu₂O₃ is identified as smooth component. The solid solution based on europium zirconate at 1500 °C is in equilibrium with all phases existing in the system ZrO₂-CeO₂-Eu₂O₃, excluding monoclinic B-europia. The field of solid solutions based on pyrochlore phase Py is directed to the side of boundary binary system ZrO₂-CeO₂. The maximum solubility of ceria in Eu₂Zr₂O₇ achieves 7 mol % CeO₂ (Table 1.10) along the iso-concentration line of 67 mol % ZrO₂, because the ion size is Ce⁴⁺ (*r*=0.090 nm), which is intermediate between ion sizes of Eu³⁺ (*r*=0.0985 nm) and Zr⁴⁺ (*r*=0.079 nm) [24]. The microstructure of solid solution based on the pyrochlore-type phase consists of randomly oriented grains, which is not typical for this phase (Fig. 1.19 a). The microstructure of the one-phase sample containing 66 mol % ZrO₂-1 mol % CeO₂-33 mol % Eu₂O₃ is presented by fine (0.8-10.8 μm) polyhedral grains clearly faceted (Fig. 1.19 a). The micro-x-ray spectral analysis showed, that the sample is one-phase, all elements (Zr, Eu) are uniformly distributes along the surface. This coincides with XRD data to confirm the solid solution formation based on ordered phase Eu₂Zr₂O₇ (Py) (Table. 1.10). The microstructures of the samples characterizing the two-phase field (Py + F-ZrO₂) are presented in the Fig. 1.19 b-d, 1.20 a-d. In the samples, containing 65 mol % ZrO₂-2 mol % CeO₂-33 mol % Eu₂O₃, 64 mol % ZrO₂-3 mol % CeO₂-33 mol % Eu₂O₃ i 64 mol % ZrO₂-4 mol % CeO₂-32 mol % Eu₂O₃ one can find two structural components, different by contrast (Fig. 1.19 b-d). The light phase is mainly represented by grains of 2.5-15.8 μm in size (Fig. 1.19 c), the dark phase – by grains of 1.7-2.1 μm in size (Fig. 1.19 b). In accordance with micro-x-ray spectral analysis data the dark phase contains zirconia only and, therefore, it could be F-ZrO₂ phase, while the gray phase was enriched with europium and zirconium. It could be identified as pyrochlore-type Eu₂Zr₂O₇ (Py) phase, which has been proved by XRD and petrography. An increase of ZrO₂ amount leads to increase of the pyrochlore phase volume and changes in morphology of grains. When ceria concentration increased, on the definite microsections of the sample 64 mol % ZrO₂-4 mol % CeO₂-32 mol % Eu₂O₃ it becomes obviously seen the refining of grains, increasing of fragility and development of crack network inside the grains (Fig. 1.19 d). In accordance with petrography data, the isotropic phases of two types were observed: the isotropic matrix phase of pyrochlore (Py) coexists with the second phase of fluorite-type (F), which is substantially less. By the cross section of CeO₂ - (67 mol % ZrO₂ – 33 mol % Eu₂O₃) in the samples containing 2-4 mol % CeO₂ one clearly finds two-phase finegrain structure, consisting of isotropic phase of pyrochlore type and locally dispersed particles of the second isotropic fluorite-type phase. The character of the two-phase microstructure (Py + F-ZrO₂), containing 70 mol % ZrO₂-4 mol % CeO₂-26 mol % Eu₂O₃, 75 mol % ZrO₂-3 mol % CeO₂-22 mol % Eu₂O₃ by the cross section ZrO₂ - (10 mol % CeO₂ - 90 mol % Eu₂O₃) substantially differs by morphology and properties (Fig. 1.20 a-d). The structure in these samples is developing as a porous and dense smooth fragments of the surfaces, where gray, smooth one belongs to <F-ZrO₂>, and gray, porous one belongs to pyrochlore Eu₂Zr₂O₇ (Py).

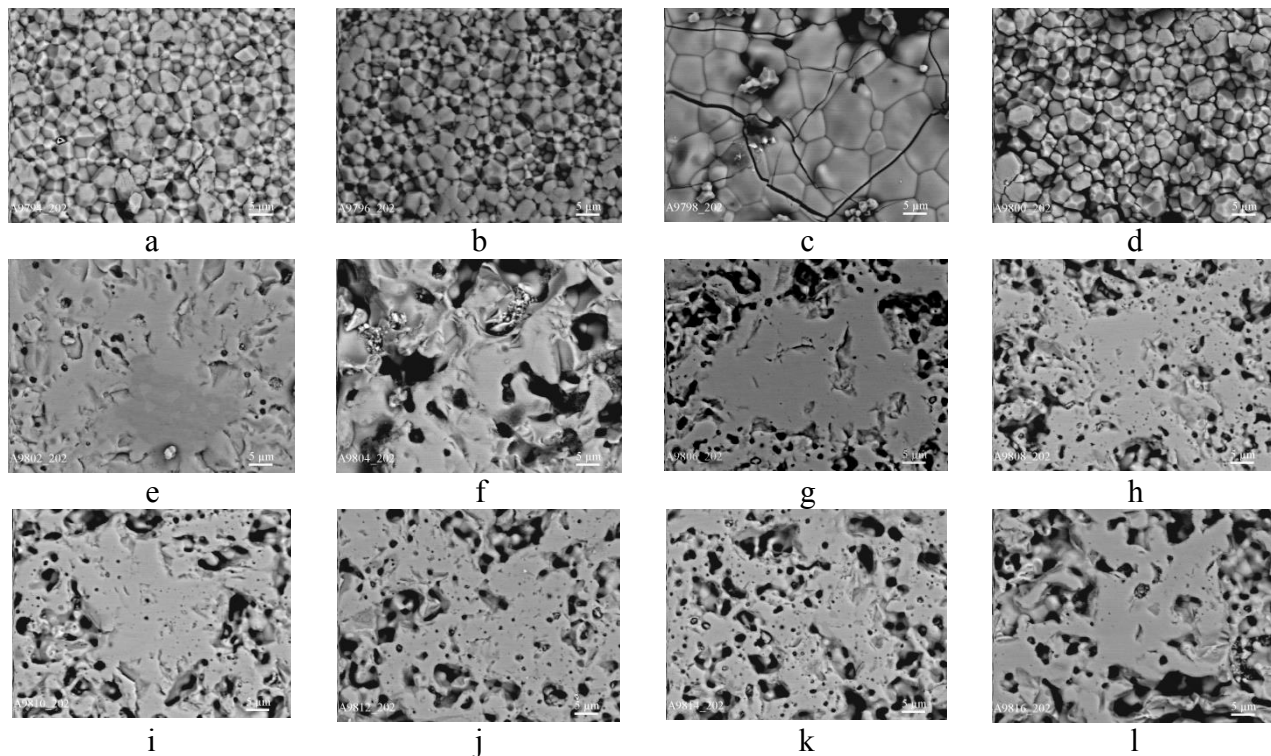


Fig. 1.19 – Microstructure of the samples in the system $\text{ZrO}_2\text{-CeO}_2\text{-Eu}_2\text{O}_3$ along the cross-section CeO_2 - (67 mol % ZrO_2 - 33 mol % Eu_2O_3) after annealing at 1500 °C:

- a) 66 mol % ZrO_2 -1 mol % CeO_2 -33 mol % Eu_2O_3 , Py ($\text{Eu}_2\text{Zr}_2\text{O}_7$), BEI, $\times 2000$;
- b) 65 mol % ZrO_2 -2 mol % CeO_2 -33 mol % Eu_2O_3 , Py + $\langle\text{F-ZrO}_2\rangle$, BEI, $\times 2000$;
gray gains - $\text{Eu}_2\text{Zr}_2\text{O}_7$ (Py), dark grains - $\langle\text{F-ZrO}_2\rangle$;
- c) 64 mol % ZrO_2 -3 mol % CeO_2 -33 mol % Eu_2O_3 , Py + $\langle\text{F-ZrO}_2\rangle$, BEI, $\times 2000$;
grains - $\text{Eu}_2\text{Zr}_2\text{O}_7$ (Py), gray phase – Py, dark phase - $\langle\text{F-ZrO}_2\rangle$, black – pores;
- d) 64 mol % ZrO_2 -4 mol % CeO_2 -32 mol % Eu_2O_3 , Py + $\langle\text{F-ZrO}_2\rangle$, BEI, $\times 2000$;
- e) 63 mol % ZrO_2 -5 mol % CeO_2 -32 mol % Eu_2O_3 , Py basis + $\langle\text{F-ZrO}_2\rangle$ + $\langle\text{C-Eu}_2\text{O}_3\rangle$ tr., BEI, $\times 2000$;
light gray (matrix) - $\text{Eu}_2\text{Zr}_2\text{O}_7$ (Py), dark gray (inclusions) - $\langle\text{F-ZrO}_2\rangle$, light phase (small inclusions in dark matrix) - $\langle\text{C-Eu}_2\text{O}_3\rangle$ tr., black – pores;
- f) 60 mol % ZrO_2 -10 mol % CeO_2 -30 mol % Eu_2O_3 , Py + $\langle\text{F-CeO}_2\rangle$ + $\langle\text{C-Eu}_2\text{O}_3\rangle$ tr., BEI, $\times 2000$;
- g) 57 mol % ZrO_2 -15 mol % CeO_2 -28 mol % Eu_2O_3 , Py + $\langle\text{F-CeO}_2\rangle$ + $\langle\text{C-Eu}_2\text{O}_3\rangle$, BEI, $\times 2000$;
gray phase - $\langle\text{F-CeO}_2\rangle$, gray porous phase - Py, light phase (small grain inclusions), crushed phase - $\langle\text{C-Eu}_2\text{O}_3\rangle$, black – pores;
- h) 53 mol % ZrO_2 -20 mol % CeO_2 -27 mol % Eu_2O_3 , $\langle\text{F-CeO}_2\rangle$ + Py + $\langle\text{C-Eu}_2\text{O}_3\rangle$, BEI, $\times 2000$;
- i) 47 mol % ZrO_2 -30 mol % CeO_2 -23 mol % Eu_2O_3 , $\langle\text{F-CeO}_2\rangle$ + Py + $\langle\text{C-Eu}_2\text{O}_3\rangle$, BEI, $\times 2000$;
- j) 44 mol % ZrO_2 -35 mol % CeO_2 -21 mol % Eu_2O_3 , $\langle\text{F-CeO}_2\rangle$ + Py + $\langle\text{C-Eu}_2\text{O}_3\rangle$, BEI, $\times 2000$;
- k) 40 mol % ZrO_2 -40 mol % CeO_2 -20 mol % Eu_2O_3 , $\langle\text{F-CeO}_2\rangle$ + Py + $\langle\text{C-Eu}_2\text{O}_3\rangle$, BEI, $\times 2000$;
- l) 37 mol % ZrO_2 -45 mol % CeO_2 -18 mol % Eu_2O_3 , $\langle\text{F-CeO}_2\rangle$ basis + Py + $\langle\text{C-Eu}_2\text{O}_3\rangle$, BEI, $\times 2000$.

The homogeneity field grain boundaries for $\text{Eu}_2\text{Zr}_2\text{O}_7$ phase, which is in equilibria with T- ZrO_2 and C- Eu_2O_3 at 1500 °C have substantial elongation to $\text{ZrO}_2\text{-Eu}_2\text{O}_3$ side of concentration triangle. The microstructures of the samples containing 80 mol % ZrO_2 -10 mol % CeO_2 -10 mol % Eu_2O_3 , 96 mol % ZrO_2 -2 mol % CeO_2 -2 mol % Eu_2O_3 , 97 mol % ZrO_2 -1.5 mol % CeO_2 -1.5 mol % Eu_2O_3 , 98 mol % ZrO_2 -1 mol % CeO_2 -1 mol % Eu_2O_3 by the section ZrO_2 - (50 mol % CeO_2 - 50 mol %

Eu₂O₃) and 70 mol % ZrO₂-9 mol % CeO₂-21 mol % Eu₂O₃, Py ↑↑ + <T-ZrO₂>, 75 mol % ZrO₂-8.5 mol % CeO₂-16.5 mol % Eu₂O₃ by the section ZrO₂ - (30 mol % CeO₂ - 70 mol % Eu₂O₃) show us that they are crystallized as two-phase compositions and accordingly to XRD, they correspond to two-phase field (Py + T) on the diagram of state. Both phases are distinct by their morphology. By the data of micro-x-ray spectral analysis the smooth gray phase is zirconia only and, obviously, corresponds to tetragonal solid solution T-ZrO₂. The gray and porous phase is enriched with europium and zirconium, thus, it relates to Eu₂Zr₂O₇ (Py), which is confirmed by x-ray analysis.

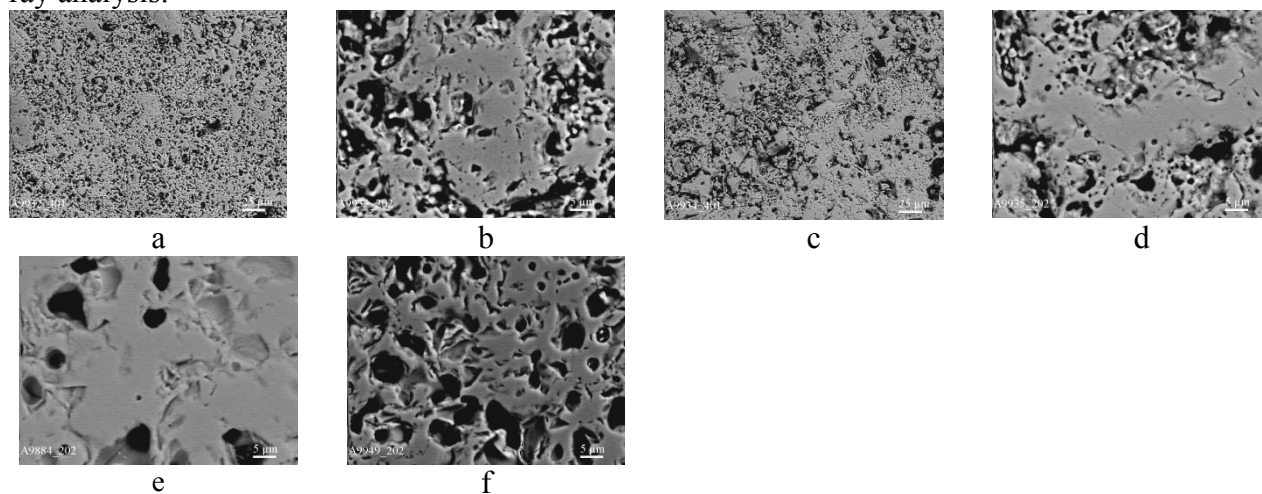


Fig. 1.20 – Microstructure of the samples ZrO₂-CeO₂-Eu₂O₃ along the section ZrO₂ - (10 mol % CeO₂ - 90 mol % Eu₂O₃) at 1500 °C:

- a) 70 mol % ZrO₂-4 mol % CeO₂-26 mol % Eu₂O₃, <F-ZrO₂> + Py, BEI, × 400;
- b) 70 mol % ZrO₂-4 mol % CeO₂-26 mol % Eu₂O₃, <F-ZrO₂> + Py, BEI, × 2000;
light gray - <F-ZrO₂>, gray porous - Eu₂Zr₂O₇ (Py), black – pores;
- c) 75 mol % ZrO₂-3 mol % CeO₂-22 mol % Eu₂O₃, <F-ZrO₂> + Py, BEI, × 400;
- d) 75 mol % ZrO₂-3 mol % CeO₂-22 mol % Eu₂O₃, <F-ZrO₂> + Py, BEI, × 2000;
- e) 55 mol. % ZrO₂-31.5 mol % CeO₂-13.5 mol % Eu₂O₃, Py basis + <F-CeO₂>, BEI, × 2000;
- f) 53.5 mol % ZrO₂-36.5 mol % CeO₂-10 mol % Eu₂O₃, <F-CeO₂> + Py, BEI, × 2000;

The samples composed of 25 mol % ZrO₂-8.5 mol % CeO₂-66.5 mol % Eu₂O₃, 30 mol % ZrO₂-8 mol % CeO₂-62 mol % Eu₂O₃, are located along the boundary of two phase field (Py + C). The peculiarity of the isothermal section of the phase diagram in the ZrO₂-CeO₂-Eu₂O₃ system at temperature 1500 °C is formation of phase equilibria on the basis of the fluorite solid solutions ZrO₂(CeO₂) with other components. There are at least three homogeneity fields of cubic phases. Similarly to two-component system ZrO₂-Eu₂O₃, the solubility gap for homogeneity field for F-ZrO₂ phase has been observed around the Eu₂Zr₂O₇ phase in the ternary system. The boundaries of the homogeneity field for the F-ZrO₂ start in the boundary binary system ZrO₂-Eu₂O₃ (72-90 mol % ZrO₂ and 45-63 mol % ZrO₂). When both solid solutions of the F-type doped with ceria, its solubility does not exceed several per cents. The extension of the F-phase in the phase diagram with high content of zirconia are defined by the samples ZrO₂ - (10 mol % CeO₂-90 mol % Eu₂O₃) iso-concentration line 85 mol % ZrO₂, containing 75 mol % ZrO₂-3 mol % CeO₂-22 mol % Eu₂O₃ – two-phase (F-ZrO₂ + Py), 80 mol % ZrO₂-2.5 mol % CeO₂-17.5 mol % Eu₂O₃ – one-phase (F-ZrO₂), 85 mol % ZrO₂-1.5 mol % CeO₂-13.5 mol % Eu₂O₃ – two-phase (F-ZrO₂ + T*). In the subsystem with low content of ZrO₂, the boundary of the solid solutions based on F-ZrO₂ goes close to the sample 45 mol % ZrO₂-2 mol % CeO₂-53 mol % Eu₂O₃ – which is two-phase (F-ZrO₂ + C-Eu₂O₃) along the iso-concentration line 45 mol % ZrO₂. The solubility limit of ceria in F-ZrO₂ is about 3 and 2 mol%, respectively. The maximal extension demonstrates the homogeneity field of the solid solution based on F-CeO₂. The boundary of the F-phase field is banded to the CeO₂ corner

starting from configuration points in the binary system $\text{ZrO}_2\text{-CeO}_2$ (56-100 mol % CeO_2) and $\text{CeO}_2\text{-Eu}_2\text{O}_3$ (80-100 mol % CeO_2). And marked with the following samples 17 mol % ZrO_2 -75 mol % CeO_2 -8 mol % Eu_2O_3 , 20 mol % ZrO_2 -75 mol % CeO_2 -5 mol % Eu_2O_3 , 13.5 mol % ZrO_2 -80 mol % CeO_2 -6.5 mol % Eu_2O_3 . The lattice parameters of the cubic phase is changing from $a = 0.5409$ nm for pure CeO_2 to $a = 0.5374$ nm for two-phase sample containing 17 mol % ZrO_2 -75 mol % CeO_2 -8 mol % Eu_2O_3 .

Accordingly to micro-x-ray spectral analysis the gray, smooth grains of the phase $\langle\text{F-CeO}_2\rangle$, gray porous structure relates to $\text{Eu}_2\text{Zr}_2\text{O}_7$. The electron microscopy data is confirmed by XRD and petrography. In the section ZrO_2 -(50 mol % CeO_2 -50 mol % Eu_2O_3), the sample containing 60 mol % ZrO_2 -20 mol % CeO_2 -20 mol % Eu_2O_3 includes two isotropic phases F-CeO_2 and $\text{Eu}_2\text{Zr}_2\text{O}_7$ in equal amount. In the sample containing 55 mol % ZrO_2 -31.5 mol % CeO_2 -13.5 mol % Eu_2O_3 by the section ZrO_2 - (70 mol % CeO_2 - 30 mol % Eu_2O_3) amount of the pyrochlore phase increases and morphology of samples changes. SEM images allow resolving of various phases by contrast: the pyrochlore as the substantive phase of light color contains dark inclusions of F-CeO_2 (Fig. 1.20 e). In the sample of boundary composition 53.5 mol % ZrO_2 -36.5 mol % CeO_2 -10 mol % Eu_2O_3 , by the section of Eu_2O_3 - (60 mol % ZrO_2 - 40 mol % CeO_2), the microstructure changes its character – the porosity disappears and one smooth phase remains only forming dark gray texture of F-CeO_2 (Fig. 1.20 f).

From the results of micro-x-ray spectral analysis one can conclude, that the light-gray and a smooth phase represents F-CeO_2 , the light-gray and porous is $\text{Eu}_2\text{Zr}_2\text{O}_7$, and the dark - T-ZrO_2 . In the cross section ZrO_2 -(70 mol % CeO_2 -30 mol % Eu_2O_3), the sample 65 mol % ZrO_2 -25 mol % CeO_2 -10 mol % Eu_2O_3 contain two isotropic F and Py phases in equal proportion as well as traces of the T-ZrO_2 with high refraction index ($n \sim 2.06$). Accordingly the petrography results, the following composition 70 mol % ZrO_2 -21 mol % CeO_2 -9 mol % Eu_2O_3 , includes two isotropic phases non-homogeneously distributed, amount of isotropic phase increases. In the sample 75 mol % ZrO_2 -16.5 mol % CeO_2 -8.5 mol % Eu_2O_3 the light gray and porous (Py) phase including gray inclusions (F-CeO_2) and intergrain dark-gray inclusions (T-ZrO_2). Isotropic phase (F-CeO_2) with numerical non-isotropic inclusions (T-ZrO_2) represents the matrix for composition 80 mol % ZrO_2 -14 mol % CeO_2 -6 mol % Eu_2O_3 . Another isotropic phase of pyrochlore type (Py) is observed in smaller amount. The higher is the zirconia content, the smaller is the grain size. In the sample 85 mol % ZrO_2 -9.5 mol % CeO_2 -5.5 mol % Eu_2O_3 the main phase is the cubic F-CeO_2 with isotropic inclusions of $\text{Eu}_2\text{Zr}_2\text{O}_7$. The non-isotropic phase is more fine-grain. The boundaries of three-phase field ($\text{Py} + \text{F-CeO}_2 + \text{T-ZrO}_2$) are defined by coordinates of samples in the section Eu_2O_3 - (60 mol % ZrO_2 - 40 mol % CeO_2) and along the iso-concentration line 85 mol % ZrO_2 . The isothermal section of the system $\text{ZrO}_2\text{—CeO}_2\text{—Eu}_2\text{O}_3$ at 1100 °C is shown in Fig. 1.21.

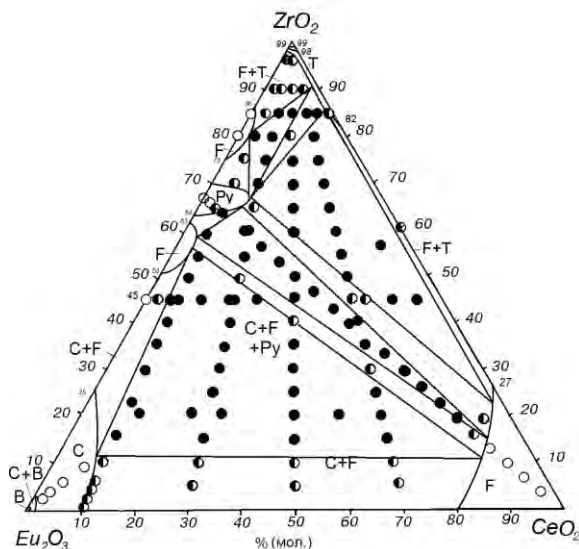


Fig 1.21 - Isothermal section of the system $\text{ZrO}_2\text{—CeO}_2\text{—Eu}_2\text{O}_3$ at 1100 °C

1.2. Phase equilibria in the $\text{ZrO}_2\text{—CeO}_2\text{—Gd}_2\text{O}_3$ systems

Systems with zirconia, ceria and gadolinia should be very promising as an alternative material for the development of thermal barrier coatings and solid oxide fuel cells [1, 2]. In addition, these systems are able to be used widely in nuclear energy engineering to develop safe and reliable technologies for the waste management nuclear industry and the development of new generation reactors [3, 4]. Presently, the search of inert matrices for immobilization of plutonium is intensive. The materials for inert matrix must meet definite requirements, such as high efficiency of neutron absorption, improved thermophysical properties such as low thermal conductivity, low coefficient of thermal expansion, the absence of phase transitions and stability at high temperatures. In addition, high temperature structural ceramics with low thermal conductivity and low thermal expansion is needed for many insulation materials, as well as parts of nuclear reactors. Due to the similarity of physico-chemical properties of plutonium oxide and cerium oxide, CeO_2 is widely used as a surrogate material instead of PuO_2 . Because the units are designed for plutonium ions, in the structural model of pyrochlore, the plutonium ions are substituted by cerium ions. To fix the transuranic elements, ceramic matrix represents the best choice, because there is long-term high thermodynamic stability. Crystal lattice of the pyrochlore phase ($\text{A}_2\text{B}_2\text{O}_7$) containing Zr is one of the ideal object $\text{M}_2\text{Zr}_2\text{O}_7$ (M is a three and/or four-charged cation) and reliable matrix for storage of highly concentrated nuclear wastes. Ordered phase of the pyrochlore type $\text{Gd}_2\text{Zr}_2\text{O}_7$ is also a promising material with thermal conductivity lower than stabilized zirconia has [4]. Thermal properties of rare earth zirconate used mainly in thermal barrier coatings on gas turbine blades to protect metal parts from hot gas streams [5-6]. It should be noted that composition corresponding to $\text{Gd}_2\text{Zr}_2\text{O}_7$ compound exists as disordered fluorite-type phase at high temperatures, while at low temperatures it becomes ordered pyrochlore-type structure in which oxygen vacancies and cations are ordered. The pyrochlore type phase undergoes order-disorder transition at a relatively high temperature of $\sim 1550^\circ\text{C}$.

In addition, refractories based on zirconium dioxide stabilized by gadolinium oxide, have found usage in installations for growing single crystals of gadolinium gallium garnet. Use these refractories provides prevention of possible contamination of single crystals during merging through evaporation stabilizing additives [7, 8]. Development of ceramic technology for refractories based on ZrO_2 meets considerable difficulties because the phase diagram of the system $\text{ZrO}_2\text{—Gd}_2\text{O}_3$ not been studied well. Phase relations in the boundary binary systems $\text{ZrO}_2\text{—Gd}_2\text{O}_3$, $\text{CeO}_2\text{—Gd}_2\text{O}_3$ has been studied in [9, 10, 11-27]. Some of the phase relations in the ternary system $\text{ZrO}_2\text{—CeO}_2\text{—Gd}_2\text{O}_3$ defined in [28]. In spite of the large amount of publication on these systems, the results are contradictory yet. Thus, the study of phase equilibria in the above systems is very important and legitimate, at least to in order to determine the solubility of Ce^{4+} in $\text{Gd}_2\text{Zr}_2\text{O}_7$.

In this work first time phase equilibria are studied in the binary $\text{ZrO}_2\text{—Gd}_2\text{O}_3$, $\text{CeO}_2\text{—Gd}_2\text{O}_3$ systems in the whole interval of concentration and at temperature 1500°C .

1.1. The system $\text{ZrO}_2\text{—Gd}_2\text{O}_3$

In the $\text{ZrO}_2\text{—Gd}_2\text{O}_3$ system at 1500°C , there had been found fields of solid solutions based on tetragonal (T) and cubic (F) modifications of ZrO_2 , monoclinic (B) and cubic (C) modifications of Gd_2O_3 and ordered phase, which crystallized in the cubic structure of pyrochlore type $\text{Gd}_2\text{Zr}_2\text{O}_7$ (Py) (Fig. 1.22). Output chemical and phase composition of the melted and annealed at 1500°C samples, parameters of elementary cells of the phases, which are in equilibria at given temperature, given in the Tables 1.12-1.13.

To determine boundaries of the phase fields the concentration dependences of elementary cells of the phases formed (Fig. 1.23). In the field with high content of ZrO_2 , the solid solutions are formed based on tetragonal ZrO_2 , however the tetragonal modification of T- ZrO_2 cannot be quenched under

given conditions, and monoclinic phase M-ZrO₂ had been found instead. The solubility of Gd₂O₃ in T-ZrO₂ is below than 1 mol. %.

In accordance with the data (Table. 1.12), the boundaries of two-phase field (T+F) had been determined as localized between 1 and 10 mol. % Gd₂O₃ (Fig. 1.23) using the concentration dependence of lattice parameters for elementary cell of the fluorite type solid solutions. The field of the fluorite solid solutions shows a gap in the temperature and concentration intervals where the pyrochlore phase Gd₂Zr₂O₇ exists. The boundaries of the F phase field at 1500 °C vary between 51-57 and 74-90 mol. % ZrO₂. The lattice parameters of the solid solutions are growing from $a = 0.5271$ to $a = 0.5294$ and from $a = 0.5148$ to $a = 0.5208$ nm (Fig. 1.23, Table. 1.12). The homogeneity fields of the F phase are separated by narrow two-phase fields (F+Py) from ordered phase fields Gd₂Zr₂O₇ of the pyrochlore phase. On the diffraction patterns of the samples 72-73 mol. % ZrO₂ and 58-60 mol. % ZrO₂ the pyrochlore phase lines were found as well as fluorite phase one (F).

Boundaries of the homogeneity fields (gadolinium zirconate) pass between 29 and 38 mol. % Gd₂O₃ (1500 °C). Lattice parameters of elementary cells for the cubic solid solutions based on Gd₂Zr₂O₇, are growing from $a=1.0426$ nm for the composition 72 mol. % ZrO₂-28 mol. % Gd₂O₃ to $a=1.0531$ nm for the composition, which contains 60 mol. % ZrO₂-40 mol. % Gd₂O₃ (Fig. 1.2, Table. 1.12). The samples containing 25 mol. % ZrO₂-75 mol. % Gd₂O₃ and 51 mol. % ZrO₂-49 mol. % Gd₂O₃ define the boundaries of the two phase fields (C+F) at 1500 °C.

The boundaries of the homogeneity field of the C phase in equilibria with F-ZrO₂ and B-Gd₂O₃ at 1500 °C are elongated from 76 to 92 % Gd₂O₃. The lattice parameter of the solid solution <C-Gd₂O₃> depends on ZrO₂ concentration on fig. 1.2. From the presented data we enable to conclude, that the solubility of ZrO₂ in C-form of Gd₂O₃ achieves 24 mol. % (1500 °C). The lattice parameter of elementary cell decreases from $a=1.0763$ nm for the composition 8 mol. % ZrO₂-92 mol. % Gd₂O₃ to $a= 1.0725$ nm for the composition, containing 25 mol. % ZrO₂-75 mol. % Gd₂O₃ (Table. 1.12). The solid solutions based on cubic C- and monoclinic B- forms of Gd₂O₃ are separated by two phase field (B+C) which continues from 92 to 99 mol. % Gd₂O₃.

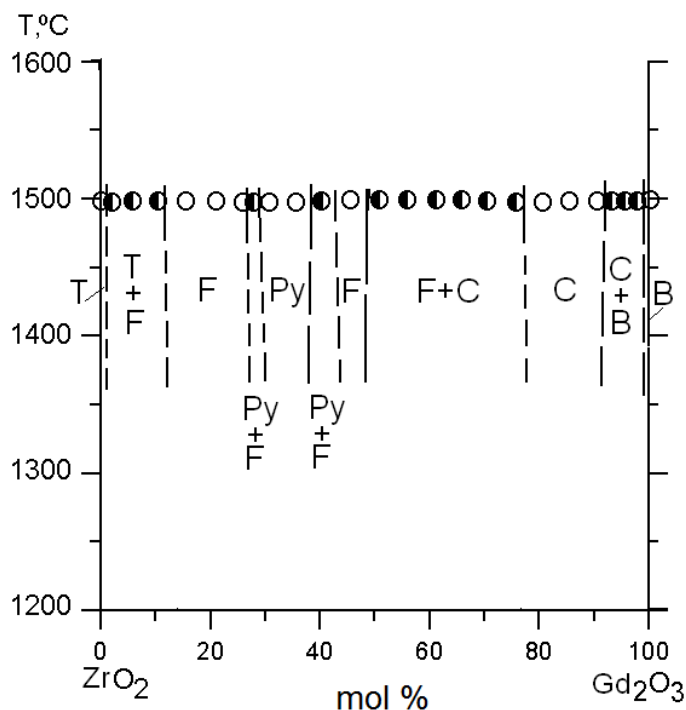


Fig. 1.22 Phase equilibria in the system ZrO₂-Gd₂O₃ at 1500 °C
(○ – one phase, ● - two-phase).

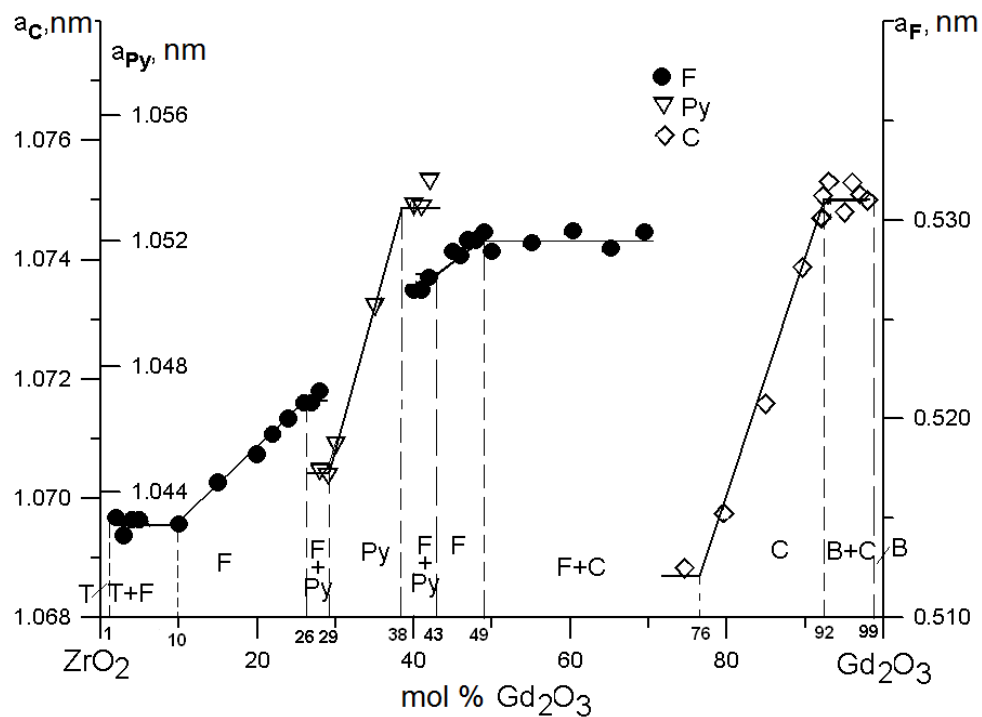


Fig. 1.23 Concentration dependences of the lattice parameters for solid solutions of the fluorite type (F, ●), cubic solutions of C- Gd_2O_3 (C, ◇) and cubic pyrochlore type $\text{Gd}_2\text{Zr}_2\text{O}_7$ (Py, ▽) in the system ZrO_2 - Gd_2O_3 after annealing the samples at 1500 °C.

Table 1.12 Phase compositions and lattice parameters of the phases in the $\text{ZrO}_2\text{-Gd}_2\text{O}_3$ system after annealing at 1500 °C, 150 year (XRD data)

Chemical composition, mol. %		Phase composition and Elementary cell parameters, nm	Cell parameters for various phases, nm ($a \pm 0.0002$)		
ZrO ₂	Gd ₂ O ₃		<C>	<F>	Py
			<i>A</i>	<i>a</i>	<i>a</i>
1	2	3	4	5	6
0	100	 ($a=1.4061$; $\epsilon=0.3566$; $c=0.8760$; $\beta=100.1$)	-	-	-
1	99	bas. ($a=1.4370$; $\epsilon=0.3571$; $c=0.8759$; $\gamma=86.0$) + <C>tr.weak.			
2	98	bas. ($a=1.4328$; $\epsilon=0.3577$; $c=0.8757$; $\gamma=86.1$) + <C>	1.0759		
3	97	basis + <C>↑	-		
4	96	 ($a=1.4207$; $\epsilon=0.3559$; $c=0.9645$; $\gamma=91.3$) + <C>↑	1.0751		
5	95	↓ ($a=1.4218$; $\epsilon=0.3392$; $c=0.0.9704$; $\gamma=87.1$) + <C>bas.↑	1.0763		
6	94	↓↓ + <C>bas.↑↑	1.0748		
7	93	↓ + <C>bas.	-		
8	92	tr↓ + <C>bas.	1.0763		
9	91	<C>	1.0747		
10	90	<C>	1.0759	-	-
15	85	<C>	1.0733	-	-
20	80	<C>	-	-	-
25	75	<C>bas. + <F>	1.0725	05363	
30	70	<C>bas. + <F>↑	1.0685	0.5352	-
35	65	<C> + <F>	1.0698	0.5306	
40	60	<C>↓ + <F>↑	1.0700	0.5308	-
45	55	<C>↓↓ + <F>↑↑		0.5297	-
50	50	<F> + <C>weak		0.5284	
51	49	<F> + <C>weak↓		0.5294	-
52	48	<F>		0.5290	
53	47	<F>	-	0.5291	-
54	46	<F>	-	0.5283	-
55	45	<F>		0.5285	
56	44	<F>		-	
57	43	<F>		-	
58	42	<F> + Py		0.5271	1.0539
59	41	<F> + Py		0.5265	1.0531
60	40	<F> + Py↑		0.5265	1.0531
65	35	Py		-	1.0499
70	30	Py		-	1.0455
71	29	Py		-	1.0416
72	28	Py + <F>		0.5215	1.0426
73	27	-	-	0.5208	-
74	26	<F>		0.5208	

75	25	<F>		0.5185	
76	24	<F>		0.5201	
77	23	<F>		0.5184	
78	22	<F>		0.5193	
79	21	<F>		0.5184	
80	20	<F>		0.5183	
85	15	<F>	-	0.5158	-
90	10	<F> + <T>*tr.	-	0.5148	-
95	5	<F> + <T>*↑	-	0.5136	-
96	4	<F> + <T>*↑ ($a=0.5129$; $\epsilon=0.5235$; $c=0.5223$; $\gamma=81.8$)	-	0.5137	-
97	3	<F>↓ + <T>*↑ ($a=0.5085$; $\epsilon=0.5224$; $c=0.5219$; $\gamma=85.3$)	-	0.5129	-
98	2	<F>↓↓ + <T>*↑↑ ($a=0.5141$; $\epsilon=0.5291$; $c=0.5218$; $\gamma=80.9$)	-	0.5137	-
99	1	<F>tr + <T>*bas. ($a=0.5301$; $\epsilon=0.5221$; $c=0.5218$; $\gamma=88.1$)	-	-	-
100	0	<T>* ($a=0.5147$; $\epsilon=0.5203$; $c=0.5315$; $\beta=99.28$)	-	-	-

Table 1.13 Phase composition and lattice parameters for the phases in the system $\text{ZrO}_2\text{-Gd}_2\text{O}_3$ after melting (XRD data)

Chemical composition, mol. %		Phase composition	Parameters of elementary cells, nm					
ZrO ₂	Gd ₂ O ₃		<F>	Py	<X>*			
			<i>a</i>	<i>a</i>	<i>a</i>	<i>b</i>	<i>c</i>	β
1	2	3	4	5	6	7	8	9
99	1	<M>+<F> _{weak}	-	-	-	-	-	-
98	2	<M>+<F>↑	0.5125	-	-	-	-	-
95	5	<M>↓+<F>	0.5137	-	-	-	-	-
90	10	<F>+<M> _{weak}	0.5153	-	-	-	-	-
85	15	<F>+<M> _{weak}	0.5172	-	-	-	-	-
80	20	<F>+<M> _{weak}	0.5184	-	-	-	-	-
75	25	<F>+Py	0.5202	-	-	-	-	-
70	30	<F>+Py↑	0.5217	-	-	-	-	-
67.5	32.5	<F>+Py↑	0.5233	-	-	-	-	-
65	35	<F>+Py	0.5233	-	-	-	-	-
62.5	37.5	<F>+Py	0.5261	1.0504	-	-	-	-
60	40	<F>+Py	0.5265	-	-	-	-	-
55	45	<F>+Py	0.5281	-	-	-	-	-
50	50	<F>+<C>	0.5303	-	-	-	-	-
45	55	<F>+<C>	0.5313	-	-	-	-	-
40	60	<F>+<C>	0.5324	-	-	-	-	-
35	65	<F>+<C>	0.5317	-	-	-	-	-
30	70	<X>*+<F>	-	-	-	-	-	-
25	75	<X>*+<F>	-	-	-	-	-	-
20	80	<X>*+<F>	-	-	-	-	-	-
15	85	<X>*+<F> _{weak}	-	-	-	-	-	-
10	90	<X>*	-	-	-	-	-	-

Continuation of the table 1.1								
5	95	$\langle X \rangle^*$	-	-				
2.5	97.5	$\langle X \rangle^*$	-	-				
0	100	$\langle X^* \rangle$	-	-	1.44 09	0.357	0.8489	93.63

*) High temperature phase $X\text{-Gd}_2\text{O}_3$ cannot be quenched under given conditions, instead of this the B- Gd_2O_3 has been revealed instead.

* Under given conditions ($T=1500\text{ }^\circ\text{C}$, 150 h., in air) the tetragonal phase of $T\text{-ZrO}_2$ cannot be fixed on quenching, the monoclinic phase has been found $M\text{-ZrO}_2$ instead.

designations: $\langle B \rangle$ – solid solutions based on monoclinic Gd_2O_3 ; $\langle T \rangle$ – solid solutions based on tetragonal modification of ZrO_2 ; $\langle C \rangle$ – solid solutions based on cubic form of Gd_2O_3 ; $\langle F \rangle$ – solid solutions based on cubic form of ZrO_2 ; Py – ordered phase $\text{Gd}_2\text{Zr}_2\text{O}_7$ of pyrochlore type. Other designations: bas. – basis phase, which is the main component of the phase mixture, weak traces – weak lines on diffraction patterns, \uparrow – amount increases, \downarrow – amount decreases.

The homogeneity field of $\langle B\text{-Gd}_2\text{O}_3 \rangle$ is rather small. In accordance with XRD data, in the sample with 1 mol. % ZrO_2 -99 mol. % Gd_2O_3 , the traces of C phase were found. The solubility of ZrO_2 in the B-form of Gd_2O_3 is almost 1 mol. % (1500°C). The lattice parameters of the elementary cell of B phase varies from $a=1.4061$, $b=0.3566$, $c=0.8760$ nm, $\gamma=100.1$ in pure Gd_2O_3 to $a=1.4370$, $b=0.3571$, $c=0.8759$ nm, $\gamma=86.0$ for boundary solid solutions.

The specific microstructures corresponding to different phase fields on the diagram of the $\text{ZrO}_2\text{-Gd}_2\text{O}_3$ system at $1500\text{ }^\circ\text{C}$ are presented in Fig. 1.24. At high temperatures ($> 2300\text{ }^\circ\text{C}$), and high content of Gd_2O_3 the solid solutions in the systems are formed based on high-temperature cubic (X) form of gadolinia, however as a result of melting under given conditions followed by slow cooling of the samples, the $X\text{-Gd}_2\text{O}_3$ phase cannot be fixed with quenching, and instead of it the low temperature monoclinic (B) phase of Gd_2O_3 is formed. The specific microstructures of melted and quenched samples in the systems $\text{ZrO}_2\text{-Gd}_2\text{O}_3$, are shown in Fig. 1.25.

The melted samples containing from 67.5 to 55 mol. % ZrO_2 are characterized by co-existence of two phases which are distinguished by contrast. In these samples, the pyrochlore phase primary precipitations have been observed (intergrain phase) together with other phase of F- ZrO_2 coarse crystals. The grain size of F- ZrO_2 varies by length from $45.83\text{ }\mu\text{m}$ до $16.66\text{ }\mu\text{m}$.

The microstructure of undereutectic composition containing 30 mol. % ZrO_2 includes grains of F- ZrO_2 , which are represented by sintered agglomerates substantially elongated, and eutectic filled intergrain spaces. The microstructure of the overeutectic composition is presented in Fig. 1.24, 1.25 e. This sample containing 20 mol. % ZrO_2 includes of light matrix grains of polyhedral shape of Gd_2O_3 by the XRD data, and eutectic filled intergrain spaces.

Thus, phase equilibria if the $\text{ZrO}_2\text{-Gd}_2\text{O}_3$ system from melting temperatures to $1500\text{ }^\circ\text{C}$ were studied. For this system, formation of boundary solid solutions based on various crystalline forms of input oxide components and the pyrochlore-type phase $\text{Gd}_2\text{Zr}_2\text{O}_7$ (Py) is very specific. The results confirmed elongated phase fields, revealed in this paper, especially in the gadolinia rich part of the phase diagram: homogeneity field of solid solutions based on C- Gd_2O_3 and two phase field (C+B) at temperature $1450\text{ }^\circ\text{C}$, respectively. Study of the phase equilibria in the system at high temperatures ($> 2300\text{ }^\circ\text{C}$) has shown the composition 25 mol % ZrO_2 -75 mol % Gd_2O_3 corresponds to eutectic coordinates.

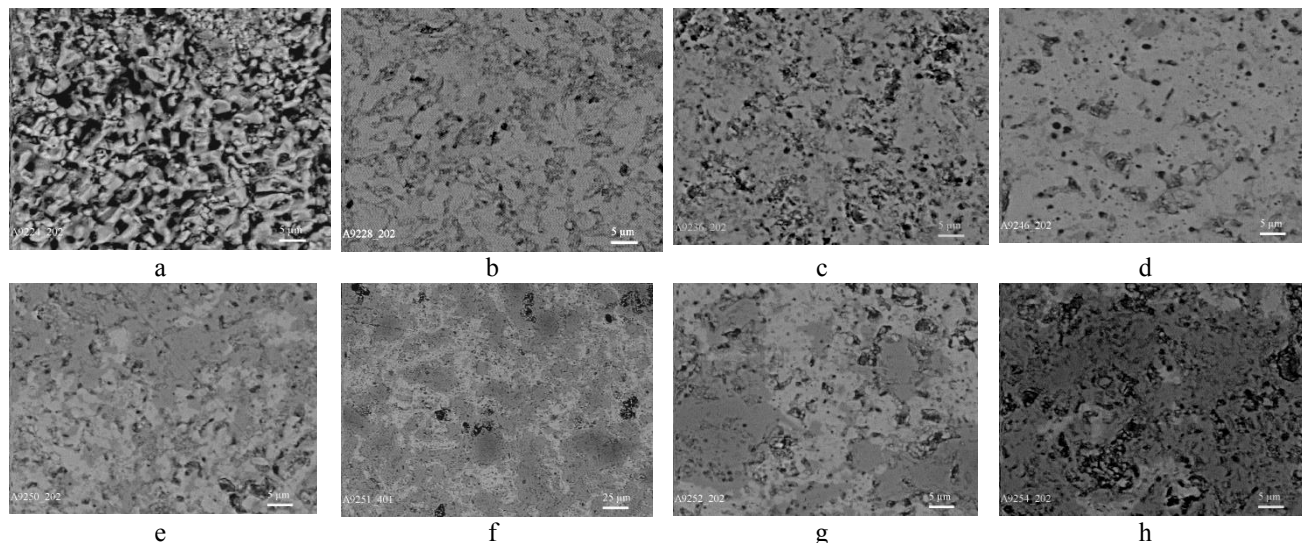


Fig. 1.24 - Microstructure of the samples in the $\text{ZrO}_2\text{-Gd}_2\text{O}_3$ system after annealing at 1500 °C:

- a) 2 mol % ZrO_2 - 98mol % Gd_2O_3 , $\langle B \rangle_{\text{bas}} + \langle C \rangle$, BEI, $\times 2000$;
b) 4 mol % ZrO_2 -96 mol % Gd_2O_3 , $\langle B \rangle + \langle C \rangle \uparrow$, BEI, $\times 2000$;
c) 8 mol % ZrO_2 -92 mol % Gd_2O_3 , $\langle B \rangle \downarrow + \langle C \rangle_{\text{bas.}}$, BEI, $\times 2000$;
dark phase - $\langle C\text{-Gd}_2\text{O}_3 \rangle$, light phase - $\langle B\text{-Gd}_2\text{O}_3 \rangle$, black phase – pores;
d) 25 mol % ZrO_2 -75 mol % Gd_2O_3 , $\langle F \rangle + \langle C \rangle_{\text{bas.}}$, BEI, $\times 2000$;
e) 35 mol % ZrO_2 -65 mol % Gd_2O_3 , $\langle F \rangle + \langle C \rangle$, BEI, $\times 2000$;
f) 40 mol % ZrO_2 -60 mol % Gd_2O_3 , $\langle F \rangle \uparrow + \langle C \rangle \downarrow$, BEI, $\times 400$;
g) 40 mol % ZrO_2 -60 mol % Gd_2O_3 , $\langle F \rangle \uparrow + \langle C \rangle \downarrow$, BEI, $\times 2000$;
h) 45 mol % ZrO_2 -55 mol % Gd_2O_3 , $\langle F \rangle_{\text{bas.}} + \langle C \rangle \downarrow$, BEI, $\times 2000$;
Light phase – $\langle C\text{-Gd}_2\text{O}_3 \rangle$, dark phase - $\langle F\text{-ZrO}_2 \rangle$, a – pores.

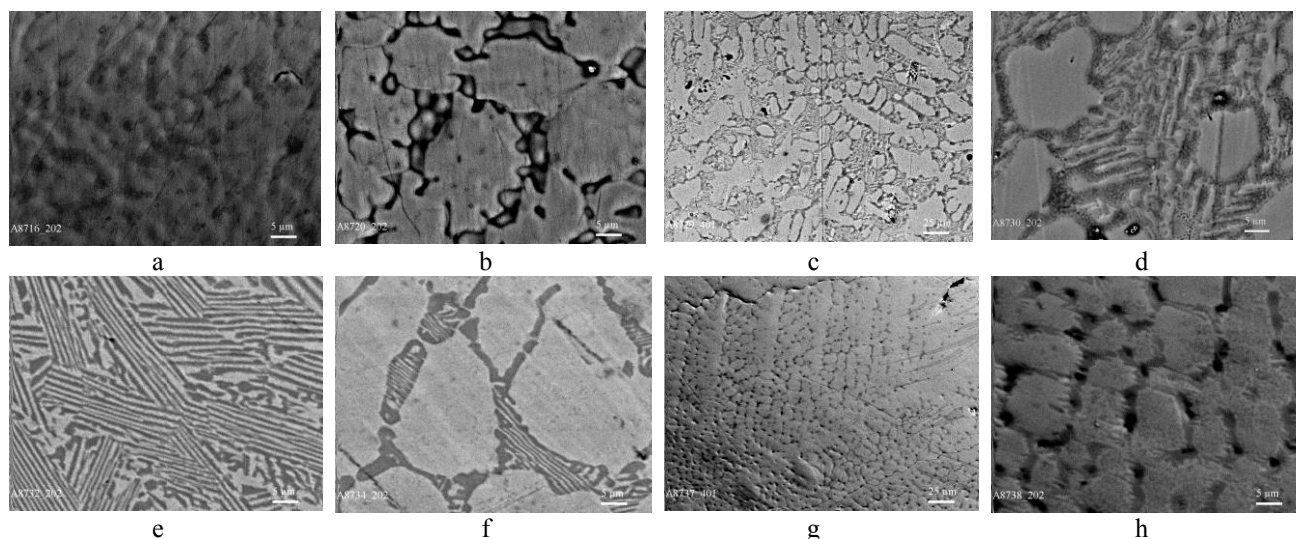


Fig. 1. 25 - Microstructure of the melted samples in the $\text{ZrO}_2\text{-Gd}_2\text{O}_3$ system

- a) 62.5 mol % ZrO_2 - 37.5mol % Gd_2O_3 , $\langle F \rangle + \text{Py}$, BEI, $\times 2000$;
b) 55 mol % ZrO_2 -45 mol % Gd_2O_3 , $\langle F \rangle + \text{Py}$, BEI, $\times 2000$;
c) 30 mol % ZrO_2 -70 mol % Gd_2O_3 , $\langle F \rangle$ in eutectics, BEI, $\times 400$;
d) 30 mol % ZrO_2 -70 mol % Gd_2O_3 , $\langle F \rangle$ in eutectics, BEI, $\times 2000$;
e) 25 mol % ZrO_2 -75 mol % Gd_2O_3 , eutectics, BEI, $\times 2000$;
f) 20 mol % ZrO_2 -80 mol % Gd_2O_3 , $\langle \text{Gd}_2\text{O}_3 \rangle$ in eutectics, BEI, $\times 2000$;
g) 15 mol % ZrO_2 -85 mol % Gd_2O_3 , $\langle \text{Gd}_2\text{O}_3 \rangle$, BEI, $\times 400$;
h) 15 mol % ZrO_2 -85 mol % Gd_2O_3 , $\langle \text{Gd}_2\text{O}_3 \rangle$, $\times 2000$.

1.2. The system $\text{CeO}_2\text{-Gd}_2\text{O}_3$

Study of the solid state reaction of CeO_2 (fluorite type, F) and Gd_2O_3 (monoclinic modification of rare earth oxides (B) at temperature 1500 °C has shown that in the $\text{CeO}_2\text{-Gd}_2\text{O}_3$ system three types of solid solutions are formed: cubic structure of fluorite type F- CeO_2 and C- Gd_2O_3 , as well as monoclinic form of B- Gd_2O_3 , which are divided by two phase fields (F+C) and (C+B), respectively (fig. 1.26). The output chemical and phase composition of the samples, annealed at 1500 °C, periods of crystalline lattices of the equilibrium phases at this temperature, are presented in Table 1.14.

The specific microstructures of the phases formed at 1500 °C in the system $\text{CeO}_2\text{-Gd}_2\text{O}_3$ are shown in Figs. 1.27. The boundaries of the homogeneity fields of the solid solutions based on F- CeO_2 , C- and B- Gd_2O_3 were determined with the aid of compositions, containing 0-15, 65-85 and 98-100 mol % Gd_2O_3 at 1500 °C (Table. 1.14).

From the data presented, the solubility of Gd_2O_3 in F- CeO_2 achieves 15 mol % at 1500 °C. The lattice parameters increase from $a=0.5409$ nm for pure CeO_2 to $a=0.5420$ nm for the sample containing 15 mol % Gd_2O_3 . The solubility of CeO_2 in monoclinic B- gadolinia is around 2 mol % CeO_2 (1500 °C). The lattice parameters for the B phase vary from $a=1.4061$, $b=0.3566$, $c=0.8760$ nm, $\gamma=100.1$ in pure Gd_2O_3 to $a=1.4380$, $b=0.3572$, $c=0.8783$ nm, $\gamma=86.9$ in boundary solid solution. With increase of ceria concentration the lines of C-forms of Gd_2O_3 decrease on the diffraction patterns. The lattice parameters of C-phase change from $a = 1.0783$ nm in the sample with 15 mol % $\text{CeO}_2\text{-85 mol \% Gd}_2\text{O}_3$ to $a = 1.0804$ nm in solid solution with 35 mol % $\text{CeO}_2\text{- 65 mol \% Gd}_2\text{O}_3$. The x-ray diffraction studies were confirmed with electron microscopy data (Fig. 1.27). Specific microstructures of two phase samples (B+C) obtained at 1500 °C are presented in (Fig 1.27 c-d). Phases differ by contrast in accordance with micro-x-ray spectral analysis: light matrix phase corresponds to monoclinic B gadolinia, gray inclusions contain more ceria, i.e. belong to cubic C modification of Gd_2O_3 . Determined, that with increase of ceria content B phase will become more finegrained. Light grain size of <B- Gd_2O_3 > change by length from $\sim 6.66\text{-}0.83$ μm to $1.25\text{-}0.166$ μm in the samples containing 1 mol % $\text{CeO}_2\text{-99 mol \% Gd}_2\text{O}_3$ and 5 mol % $\text{CeO}_2\text{-95 mol \% Gd}_2\text{O}_3$, respectively. Microstructures, specific for two phase field (C+F) at 1500 °C presented in Figs. 1.27. e-h. The sample 55 mol % $\text{CeO}_2 - 45$ mol % Gd_2O_3 includes two structure components. The light gray matrix C- Gd_2O_3 with dark inclusions of F- CeO_2 of non-isometric shapes and sizes $6.94\text{-}1.38$ μm .

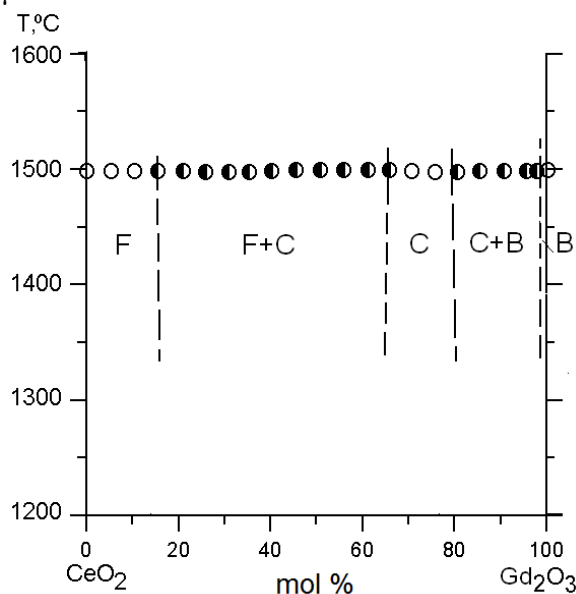
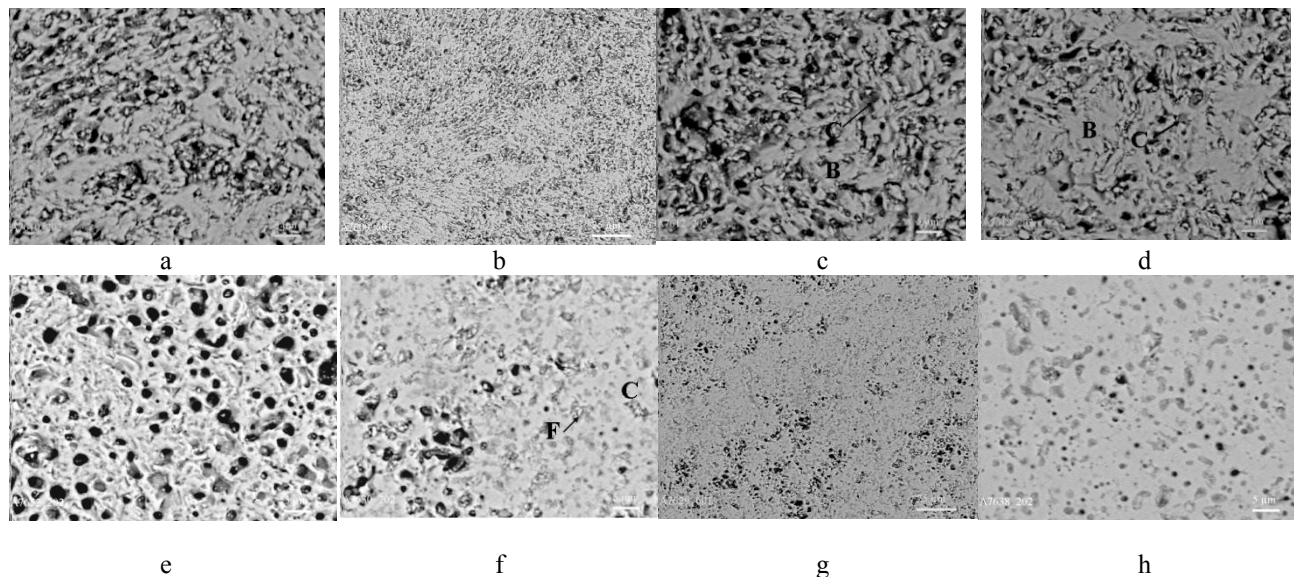


Fig. 1.26. Phase equilibrium in the system $\text{CeO}_2\text{-Gd}_2\text{O}_3$ at 1500 °C
(○ – one phase, ● - two phase samples).



Figs. 1. 27. Microstructures in the system $\text{CeO}_2\text{-Gd}_2\text{O}_3$ at 1500 °C:

- a) 1 mol % CeO_2 - 99 mol % Gd_2O_3 , B- Gd_2O_3 bas., BEI, $\times 2000$;
- b) 1 mol % CeO_2 - 99 mol % Gd_2O_3 , B- Gd_2O_3 bas., BEI, $\times 600$;
- c) 2 mol % CeO_2 - 98 mol % Gd_2O_3 , B- Gd_2O_3 + C- Gd_2O_3 , BEI, $\times 2000$;
- d) 5 mol % CeO_2 - 95 mol % Gd_2O_3 , B- Gd_2O_3 + C- Gd_2O_3 , BEI, $\times 2000$;
- light matrix - <B- Gd_2O_3 >, gray inclusions - <C- Gd_2O_3 >, black – pores;
- e) 35 mol % CeO_2 - 65 mol % Gd_2O_3 , C- Gd_2O_3 + F- CeO_2 , BEI, $\times 2000$;
- f) 35 mol % CeO_2 - 65 mol % Gd_2O_3 , C- Gd_2O_3 + F- CeO_2 , BEI, $\times 600$;
- g) 45 mol % CeO_2 - 55 mol % Gd_2O_3 , C- Gd_2O_3 +F- CeO_2 , BEI, $\times 2000$;
- h) 55 mol % CeO_2 - 45 mol % Gd_2O_3 , C- Gd_2O_3 + F- CeO_2 , BEI, $\times 600$;
- i) 90 mol % CeO_2 - 10 mol % Gd_2O_3 , F- CeO_2 , BEI, $\times 2000$;
- j) 90 mol % CeO_2 - 10 mol % Gd_2O_3 , F- CeO_2 , BEI, $\times 600$,
- light matrix - <C- Gd_2O_3 >, gray inclusions - <F- CeO_2 >, black – pores.

Table 1.14 Phase compositions and lattice parameters of the phases after annealing in the CeO₂-Gd₂O₃ system at 1500 °C, for 150 h. (XRD data)

Chemical composition, mol %		Phase composition	Lattice parameters, nm ($a \pm 0.0002$)					
CeO ₂	Gd ₂ O ₃		<F>	<C>				
			a	a	a	B	c	β
1	2	3	4	5	6	7		
0	100		-	-	1.4061	0.3566	0.8760	100.1
1	99	bas.	-	-	1.6026	0.3568	0.8825	96.0
2	98	bas. + <C>weak	-	-	1.4380	0.3572	0.8783	86.9
3	97	 + <C>tr.↑	-	1.0807	1.4276	0.3472	1.0628	87.7
4	96	 + <C>↑	-	1.0804	1.4211	0.3472	1.0755	91.3
5	95	↓ + <C>↑	-	-	1.4212	0.3466	1.0742	87.2.
10	90	↓ + <C>↑	-	1.0804	1.3905	0.3392	0.9566	83.8
15	85	↓ + <C>bas.	-	1.0783	-	-	-	-
20	80	<C>bas.	-	1.0813	-	-	-	-
25	75	<C>	-	1.0785	-	-	-	-
30	70	<C>	-	1.0805	-	-	-	-
35	65	<C> + <F>	0.5403	1.0804	-	-	-	-
40	60	<C> + <F>	0.5402	1.0804	-	-	-	-
45	55	<C> + <F>	0.5406	1.0811	-	-	-	-
50	50	<C> + <F>	0.5403	1.0805	-	-	-	-
55	45	<C> + <F>	0.5409	1.0812	-	-	-	-
60	40	<C>↓ + <F>	0.5420	1.0831	-	-	-	-
65	35	<C>↓ + <F>bas.	0.5416	-	-	-	-	-
70	30	<C>tr.↓ + <F>bas.	0.5420	-	-	-	-	-
75	25	<F>bas. + <C>weak.↓↓	0.5414	-	-	-	-	-
80	20	<F>bas. + <C>weak.↓↓	0.5420	-	-	-	-	-
85	15	<F> + <C>tr.	0.5420	-	-	-	-	-
90	10	<F>	0.5423	-	-	-	-	-
95	5	<F>	0.5410	-	-	-	-	-
100	0	<F>	0.5409	-	-	-	-	-

Marking: is a solid solution based on monoclinic Gd₂O₃; <C> is a solid solution based on cubic rare earth oxides such as Gd₂O₃; <F> is a solid solution based on cubic phase CeO₂ of fluorite type. Other symbols: bas. is the main phase, weak means low intensity peaks, tr. means traces of the phase, ↑ means increasing of the phase amount, ↓ means decreasing of the phase amount.

2. Transparent ceramics manufacturing

Yttrium aluminum garnet $\text{Y}_3\text{Al}_5\text{O}_{12}$ (YAG, cubic) ceramics doped with luminescent centers of rare earth ions (RE^{3+}), such as Nd^{3+} and Yb^{3+} , are well studied materials for high-power laser applications because of their high quantum efficiency and high enough mechanical and thermal properties. Recently, operation of a 100 kW JHPSSL Nd:YAG laser was demonstrated using high purity ceramics materials [1]. Alternatively to cubic garnets, the transparent ceramic matrices based on rare earth oxides and their compounds are considered perspective for advanced laser systems. Pure rare-earth oxides of yttria sub-group or their solid solutions with cubic symmetry of lattice (C-type REO) and, therefore, arbitrarily oriented grains in ceramics are widely studied. For instance, solid solutions based on Y_2O_3 - La_2O_3 system (such as $\text{La}_x\text{Y}_{2-x}\text{O}_3$, where $x=0.05\div0.20$) doped with scintillating additives (Nd, Eu, Sm, Tb, Er, Yb) have been subject of research. Many excellent characteristics were achieved for these laser media, but all of them did not result in breakthrough properties as compared to ones of garnets.

Besides high symmetry cubic crystals, the non-cubic anisotropic crystals attract interest to be more effective laser matrices than their isotropic competitors because they enable to harvest excitation energy from two directions of irradiations, but emit monochromatically mostly in one selected direction. The fabrication of laser-grade anisotropic ceramics through the conventional particulate processes is not realistic because of resulting randomly oriented grains and grain boundaries and, therefore, additional optical scattering. Fabrication of transparent polycrystalline ceramics from non-cubic materials requires precise crystal orientation control so that optical scattering losses at the grain boundaries are prevented [2]. The manufacturing of transparent anisotropic ceramics by using a new crystal orientation process of particles deposition in strong magnetic field (DSMF) is grounded on the property of large magnetic anisotropy induced by 4f electrons of RE^{3+} ions (scheme in Fig. 2.1). In the case of ideal alinement of anisotropic grains strictly along one axis, the DSMF offers a key approach to extremely high-power laser materials such as RE:FAP and patterning process for multi-function integrated monolithic solid-state lasers [3]. For example, they have first proposed realization of transparent anisotropic laser ceramics by using a new crystal orientation process based on large magnetic anisotropy induced by 4f electrons of rare earth oxides. Applying the slip casting in a 1,4 T magnetic field followed by heat treatment, there have been successfully fabricated laser-grade rare-earth-doped calcium fluorapatite ceramics with a loss coefficient of $1,5 \text{ cm}^{-1}$ [2].

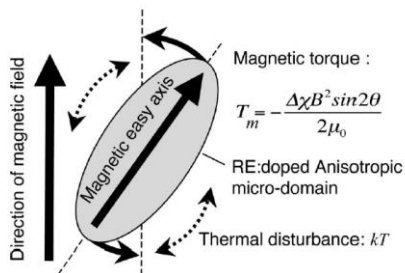


Fig. 2.1. Schematic of the RE-assisted magnetic orientation method for fabrication of RE-doped anisotropic laser ceramics. The magnetic anisotropy $\Delta\chi$ is enhanced by RE doping [$\Delta\chi = 10^{-4} - 10^{-6}$ (RE doped), $\Delta\chi = 10^{-6} - 10^{-7}$ (undoped)] [2].

From the literature review we have learned the main requirements to *rare-earth-doped anisotropic ceramic materials* can be formulated as follows:

- *large stimulated emission;*
- *big absorption cross sections;*
- *long fluorescence life time [4];*
- *high quantum efficiency;*
- *excellent optical characteristics: superior transparency higher than 80%;*
- *superior mechanical and thermo-mechanical properties;*

- *fabrication of transparent polycrystalline ceramics from non-cubic materials requires precise crystal orientation control so that;*
- *optical scattering losses at the grain boundaries are prevented;*
- *crystal orientation of diamagnetic and paramagnetic materials, as well as that of magnetic materials, can be controlled by imposing a high magnetic field of $1\div 10$ T [5-8] as dependent on magnetic susceptibility difference.*

For instance, the $\text{Sr}_5(\text{PO}_4)_3\text{F}$, has been chosen as host material, due to its favorable spectroscopic properties such as high emission and absorption cross-sections, large induced crystal field splitting. In $\text{Sr}_5(\text{PO}_4)_3\text{F}$ lattice, two inequivalent cation sites are present: Sr(1) with C_s symmetry is surrounded by six oxygen atoms and one fluorine atom, whereas the Sr(2) with C_3 symmetry is coordinated to nine oxygen. Among lanthanides ions, it is well known that Eu^{3+} is suitable as a probe for determination of local structure in the host matrix because of their simple multiplet pattern and straight forward symmetry behavior of the energy levels. RE^{3+} can substitute for Sr^{2+} ions at both sites in terms of the similar radius of them. Generally, the substitution of RE^{3+} for Sr^{2+} ions depends on the local charge compensation.

In the framework of present project, it has been supposed that the materials based on orthorhombic phase of LaYO_3 type doped with scintillating additives (Nd_2O_3 , Yb_2O_3) is prospective for research. The crystal structure of LaYO_3 (LaYbO_3) ceramics have been investigated by Rietveld refinements performed on X-ray data. They showed the room-temperature structure to be best described by the orthorhombic Pnma space group [$a = 0.5894$ nm, $b = 0.6092$ nm, $c = 0.8496$ nm, $\alpha = 90^\circ$, $\beta = 90^\circ$, $\gamma = 90^\circ$ unit volume of 0.30506 nm³, Z4, and theoretical density, $D(\text{LaYO}_3)=6.01$ g/cm³, $D(\text{LaYbO}_3)=8.04$ g/cm³] in agreement with electron diffraction experiments. LaYO_3 perovskite demonstrates difference in magnetic susceptibility similar to its crystallography analog of LaYbO_3 of $(2\div 5)\cdot 10^{-6}$. Such a value of magnetic anisotropy appears to be enough for dipole's orientation in suspension under strong magnetic field of 1-10 T.

Properties of the samarium doped LaYO_3 nanocrystalline phosphor powders were studied in [9]. The ceramic matrix has been obtained by polymer complex solution method. Crystallization from the amorphous state (with some residuals of carbon) resulted in nanoparticles with crystalline structure corresponding to distorted perovskite type structure for the first time. Luminescence properties of Sm^{3+} doped LaYO_3 particles exhibited characteristic orange-to-red emission coming from the intra-4f-shell $4G_{5/2} \rightarrow 6H_J$ electron transitions with emission decay of 1.5 ms. Energy level positions are derived from emission and excitation spectra [9].

Ceramics fired at 1600 °C for 4 h attain ~97% of theoretical density and their microstructures consist of randomly distributed equiaxed grains with an average size of ~8 μm. Conventional transmission electron microscopy shows densification to occur in the absence of a liquid phase and reveals domain-free grains. Conductivity measurements show that the doped- LaYO_3 is a *p*-type semiconductor at high oxygen partial pressures, but becomes a pure oxide-ion conductor at low oxygen partial pressures [10], which is good to define sintering medium.

The fabrication of textured ceramics has been carefully developed recently, due to a growing necessity of manufacturing advanced ceramics materials that have to meet definite requirements concerning their properties. A controlled development of crystalline texture in ceramics makes it feasible to improve some optical, electrical, piezoelectric and mechanical properties of those materials. There are few methods of producing textured ceramics elaborated so far, including template grain grow (TGG) or hot forging. Magnetic alignment is one of the most recent and well researched method [5]. The idea is to make the ceramic particles in a suspension aligned during the colloidal processing due to the influence of a high magnetic field. The strong texture can be developed during subsequent sintering of the shaped elements. The shaping itself is conducted usually by slip casting. This way of fabricating textured ceramics is becoming popular because it does not require large templates or high uniaxial pressure. α -Alumina, commonly used in ceramics processing, belongs to the rhombohedral crystalline system. It exhibits anisotropic susceptibility, but this anisotropy had been more or less ignored due to its very low value. The development of

superconducting magnet has extended the potential applications of strong magnetic fields for particle alignment.

2.1 Synthesis of nanosize powders

The sub-project is about manufacturing of optically transparent polycrystalline ceramic materials based on high-melting oxides such as isotropic yttria-alumina garnet ($\text{Nd:Y}_3\text{Al}_5\text{O}_{12}$) and anisotropic RE:LaYO_3 ($\text{RE} = \text{Nd, Yb}$). This part includes: synthesis of nanosize powders for various solid solutions based on LaYO_3 and $\text{Y}_3\text{Al}_5\text{O}_{12}$ in the particle size range 10-15 nm valid for manufacturing dense nanocrystalline ceramics. Note that the sub-micron in size and near-spherical particles in shape are good for dense transparent isotropic ceramics such as $\text{Y}_3\text{Al}_5\text{O}_{12}$, but for anisotropic one such as LaYO_3 , the nanopowders of 10 nm are principal to get high transparency.

The literature search and review of the papers describing optically transparent ceramics has been carried out. More than 1000 papers and abstracts for last 20 years have been collected and reviewed, to understand the main technical approaches to achieve highly transparent ceramics of laser application. The main conclusions done are as follows:

- The Nd:YAG ceramic laser rods show currently comparable or even better emission characteristics than the similar (size, doping concentration) single crystal rods.
- Fabrication of high transparency ceramics requires 100% density to form a pore-free microstructure.
- The densification of ceramics is determined by the microstructure of the green body (such as the grain size and morphology, particle size distribution (PSD), the average size of agglomerate and pore), rather than individual particles.
- A well sinterable powder with a small particle size, narrow PSD, and low-agglomeration, is crucial for the fabrication of RE:LaYO_3 ($\text{RE} = \text{Nd, Yb}$) or Nd:YAG transparent ceramics.
- The co-precipitation is the most effective route to synthesize Nd:Y₂O₃ powders and others.

Synthesis of RE:LaYO_3 ($\text{RE} = \text{Nd, Yb}$) or Nd:YAG nanopowders has been carried out by the hydroxide co-precipitation method. Powders of La_2O_3 , 99.99%, Y_2O_3 , 99.99%, Nd_2O_3 , 99.99%, Yb_2O_3 , 99.99% and $\text{Al}(\text{NO}_3)_3 \cdot 9\text{H}_2\text{O}$ were dissolved in 1N HNO_3 solution, respectively. These solutions were mixed at the stoichiometric ratio to form the Nd:YAG, Nd:LaYO₃ or Yb:LaYO₃ precursors. The solution was stirred under ultrasonic irradiation. Co-precipitation of rare earth hydroxides was carried out in the reactor with permanent stirring by dropping of 0.1 N solution to cold ammonia solutions (ammonium hydrocarbonate, sulphate). For complete precipitation the pH was maintained near 9. The precipitates were dried through several steps: the mixed precipitate was dried in a vacuum drying chamber at 80 °C for 24 h to remove the main portion of crystalline water, and then temperature was raised to 200 °C for 3 h to remove the rest of crystalline water. Final firing has been done at 600 °C for 2-3 hours until complete crystallization of precipitate. Firing to get high degree of crystallinity of particles has been done above 1200 °C for 2-20 hours. This heat treatment is especially important to get particles orientable in strong magnetic field. After annealing the powders were grinded manually in mortar followed by homogenizing in Teflon ball mill charged with zirconia 3 mm balls in the media of absolute alcohol with additives of polyethyleneimine solution. The nanopowders of neodymia (ytterbia) doped LaYO_3 were characterized in their properties using: specific surface area measurements (BET and BJH methods, by ASAP 2000), particle size distribution by laser granulometry (Malvern Nanosizer), particle shape and structure by electron microscopy. Stoichiometry and concentration of luminescent dopants (neodymia, and ytterbia) has been determined by x-ray fluorescent method using Rigaku Primini spectrometer. Full technological scheme from chemicals to sintered ceramics is presented in fig. 2.2.

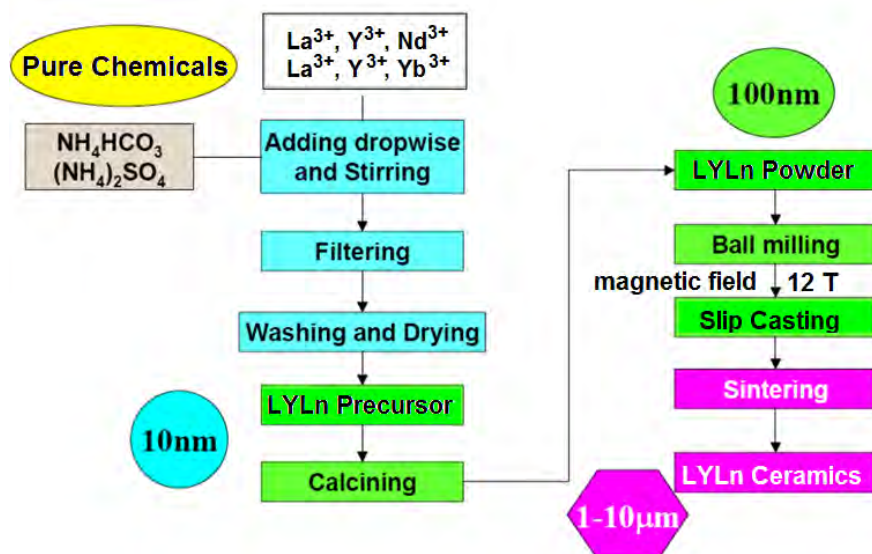


Fig. 2.2 Technological scheme for manufacturing of transparent ceramics

Characterization of Nd:Y₂O₃ nanopowders.

The precipitates of Nd:Y₂O₃ after drying and water removal were XRD-amorphous. The specific surface area was about 60 ±5 m²/g independently on concentration of neodymium. The particle size distribution measuring has shown mean particle size of 15-20 nm and agglomerate sizes increasing from 35 to 70 nm. The transmission electron microscopy data has shown the Nd:Y₂O₃ nanoparticles are almost spherical in shape, weakly agglomerated (Table 2.1).

Table 2.1 Characteristics of particulate samples based on Nd:Y₂O₃.

Powder sample #	Content of Nd at %	Specific surface area, m ² /g	Mean particle size, nm	Agglomerate size, nm	Time of de-agglomeration, hour
Y001	0.06	58.2	18	37	24
Y002	0.1	55.8	20	48	24
Y003	0.2	59.4	18	45	24
Y004	0.6	62.3	16	53	24
Y005	1.0	60.7	15	45	36
Y006	1.2	59.6	18	59	36
Y007	1.4	64.4	15	66	48
Y008	1.6	61.9	16	72	48

<p>agglomerates</p>	<p>particles</p>	<p>50 nm</p> <p>Microscopy image of Nd:Y₂O₃ nanoparticles</p>
---------------------	------------------	---

Fig. 2.3 Examples of the particle size distributions (agglomerates and true particles) and their view.

Particle size distribution has been controlled by Malvern ZetaSizer and shown mean particle size range 10-22 nm assembled to agglomerates of 40-120 nm in size. Agglomeration was found to depend on drying conditions. To get homogeneous suspensions, durable grinding has been provided for 24-48 hours in alcohol medium. Powders were mixed with 0.5 wt.% tetraethyl orthosilicate (TEOS) added as sintering aid. Preliminary pressed at 100-380 MPa samples were subjected to hydrostatic compression at 200-500 MPa. The best green density of 56% theoretical has been achieved.

Table 2.2. Characteristics of particulate samples based on Nd:YAG

Powder sample #	Content of Nd at %	Specific surface area, m ² /g	Mean particle size, nm	Agglomerate size, nm	Time of de-agglomeration, hour
YAG001	0.06	93	14	44	24
YAG002	0.1	85	15	53	24
YAG003	0.2	103	11	51	24
YAG004	0.6	88	15	49	24
YAG005	1.0	77	17	66	48
YAG006	1.1	73	19	73	48
YAG007	1.2	74,5	17	79	48
YAG008	1.3	62	22	87	48

Characterization of Ln:LaYO₃ nanopowders.

The precipitates of Ln:LaYO₃ after drying and water removal were XRD-amorphous. The specific surface area was about $80 \div 110 \pm 5$ m²/g independently on concentration of dopant for all dopants used. The particle size distribution measured for 1.0-10 at.% doped perovskites has shown mean particle size of 10-20 nm and agglomerate sizes increasing from 45 to 170 nm. The results of laser granulometry are presented in Fig. 2.4 (a-c). The field emission scanning electron microscopy data has shown the Nd:LaYO₃ nanoparticles are almost spherical in shape, and agglomerated (Fig. 2.5).

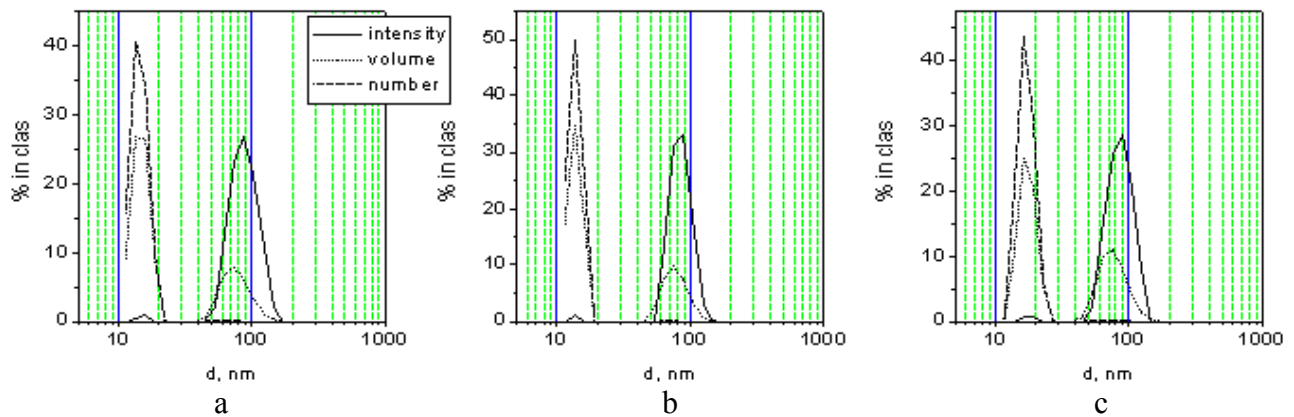


Fig. 2.4 Particle size distribution of the Nd:LaYO₃ (a), Eu:LaYO₃ (b), Yb:LaYO₃ (c).

Annealing of as-prepared powders has been carried out at 1200 °C for 10-20 hours to allow amorphous particles to be crystallized and growth by coalescence. Before using slip casting in magnetic field, the particles must be stable, single crystalline and easy for suspending. The typical XRD pattern of Nd:LaYO₃ is presented in Fig. 2.6. To get homogeneous suspensions, durable grinding has been provided for 24-48 hours in alcohol medium in fluoroplastic drum with zirconia balls. The as-annealed powders of Nd:LaYO₃ with average particle size of 220 nm is shown in Fig. 2.7.

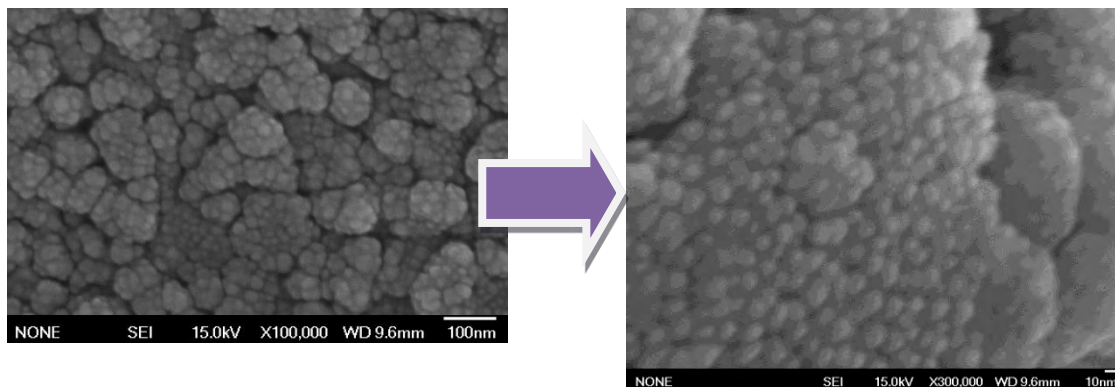


Fig. 2.5. Agglomerates of the Nd:LaYO₃ nanoparticles and internal structure of agglomerates with particle sizes of 10-20 nm assembled in agglomerates of 100-170 nm size.

Table 2.3 Characteristics of particulate samples based on Ln:LaYO₃.

Powder sample #	Content of Ln at %	Specific surface area, m ² /g	Mean particle size, nm	Agglomerate size, nm	Regime of annealing °C / hours	Time of de-agglomeration, hour
Nd:LaYO ₃						
Nd001	1.0	85.8	12	77	1200 / 10	48
Nd002	3	69.1	15	83	1200 / 10	48
Nd003	5	59.4	18	89	1200 / 10	48
Nd004	10	48.3	21	103	1200 / 10	48
Yb:LaYO ₃						
Yb001	1.0	60.7	13	95	1200 / 20	48
Yb002	3	59.6	13	91	1200 / 20	48
Yb003	5	54.4	16	94	1200 / 20	48
Yb004	10	51.9	17	108	1200 / 20	48

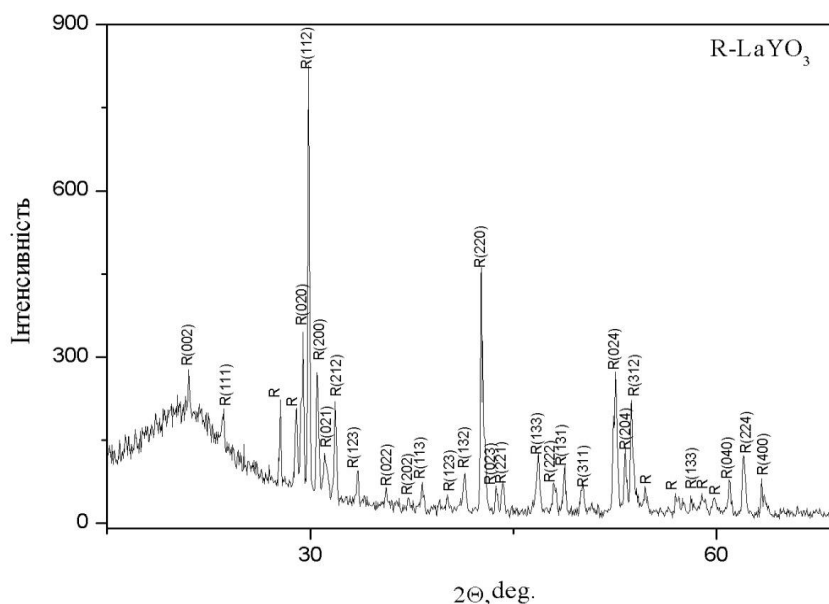


Fig. 2.6. XRD pattern of the composition 49.5% La₂O₃-49.5%Y₂O₃-1%Nd₂O₃

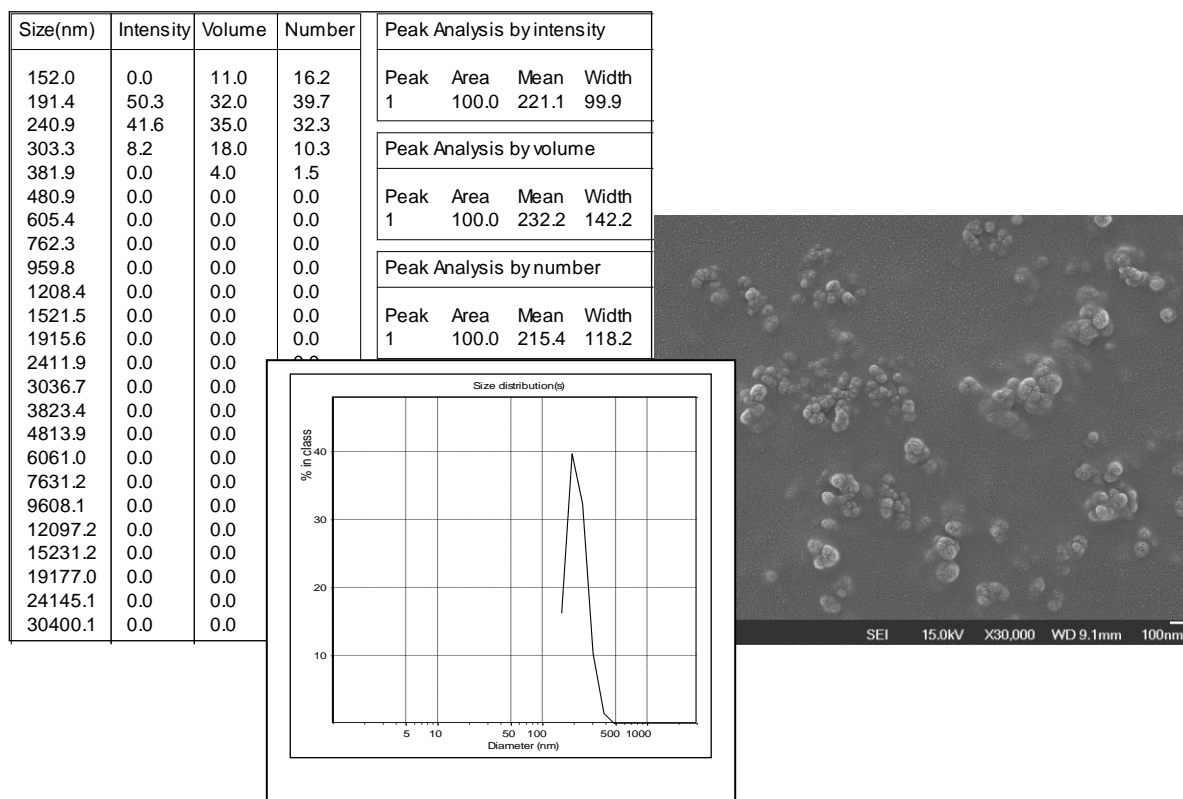


Fig. 2.7 Particle size distribution and FESEM image of as-annealed particles of Nd:LaYO₃.

Initially, a slurry containing Nd:LaYO₃ particles and absolute ethanol was mixed with a small amount of polyethyleneimine (ALON A-6114; Toagohosei Co., Tokyo, Japan) as the dispersant. (*MW* = 10 000 g mol⁻¹, Wako Pure Chemical Industries, Ltd., Tokyo, Japan). The resulting mixture was mechanically ground in ball mill with zirconia balls for 48 hours to convert the aggregated particles to single particles. The suspensions of 5 vol.% solid phase loading were ultrasonically dispersed (GSD600AT; Sonic Technology Co., Ltd., Saitama, Japan) for 10 min before slip casting. The suspensions were outgassed in a vacuum to remove as many air bubbles as possible. The slurry was then poured into a porous mold, and slip casting was carried out in a horizontal static magnetic field of 12 T (JMTD-12T100NC5; Japan Superconductor Tech. Inc., Hyogo, Japan) at room temperature for 12 hours.

Green sampling.

Green density of consolidated ceramics is one of the key parameter to successfully prepare transparent ceramics on sintering. High density green samples in the range of 68-70% of theoretical density have been prepared using tape casting. In the Table 2.3 one can find data concerning wet consolidation of tapes from suspensions. The 120 nm size granules containing ceramic nanoparticles, SAR and polyvinylbuteral form densely packed samples. This density remains almost unchanged after burning out the binder and SAR. Annealing at 450 C resulted in samples ready for sintering. Green square samples of 1x1 cm were cut from the green tape. To develop the rate controlled sintering regime for optical ceramic, the preliminary sintering experiments have been started and are in progress now. For each composition of Nd:Y₂O₃ and Nd:Y₃Al₅O₁₂ phases, from 10 to 12 various constant heating rate regimes without isothermal holding have been recorded up to 1700 °C. The isothermal hold of 2 to 12 hours has been provided then. The relative density for sintered squares is listed in the last column of the Table 2.4.

Table 2.4 Characteristics of sintered samples based on Nd:YAG

Powder sample #	Content of Nd at %	Green density, % of theor.	Sintering temperature, °C	Sintering time, Hours	Sintered density, % of theor.
YAG001	0.06	60.1 64.8 68.9	1700	2/12	96.7/98.1 97.3/98.8 98.2/99.1
YAG002	0.1	59.2 64.3 69.1	1700	2/12	96.1/98.4 97.9/99.0 98.6/99.3
YAG003	0.2	59.5 65.2 69.0	1700	2/12	95.9/97.8 96.8/98.2 98.0/98.9
YAG004	0.6	59.4 65.0 69.3	1700	2/12	96.5/98.9 97.3/99.0 98.5/99.4
YAG005	1.0	58.8 64.9 68.9	1700	2/12	96.1/97.9 97.1/98.6 98.2/99.1
YAG006	1.1	59.0 64.7 69.1	1700	2/12	96.0/97.4 96.8/98.3 98.1/99.2
YAG007	1.2	60.1 64.6 69.2	1700	2/12	95.7/97.1 96.6/98.7 97.8/99.0
YAG008	1.3	59.5 64.8 69.7	1700	2/12	95.7/97.3 97.0/98.4 98.5/99.3

The best density of the sintered ceramics of 99.0-99.4 was achieved for neodymia-doped yttria. The samples were 45-50% transparent. The garnet samples showed residual porosity (0.5-0.7%). The isothermal holds of 2-12 hours are proposed to be used at 1700 °C and less to allow samples to fill the residual porosity and get transparency.

The green samples of Nd:LaYO₃ or Yb:LaYO₃ were prepared by slip casting in strong magnetic field followed by hydrostatic compression at 50 MPa to achieve uniform porosity distribution and higher density. After slip casting, the samples were dried slowly and annealed at 600 °C for 10 hours to remove organic compounds. Preliminary sintering to fix textured structure was carried out at 1200 °C.

Fully dense ceramic pieces based on rare earths can be obtained by two-step sintering and rate controlled sintering techniques. To develop the rate controlled sintering regime for optical ceramic, the kinetic field of responses for sintering experiments have been calculated. For each composition of Nd:LaYO₃, Yb:LaYO₃ phases, from 10 to 12 various constant heating rate regimes without isothermal holding have been recorded up to 1600-1700 °C. The isothermal hold of several hours has been provided if porosity higher than 1% remained after RCS mode. The relative density for sintered samples is listed in the last column of the Table 2.5.

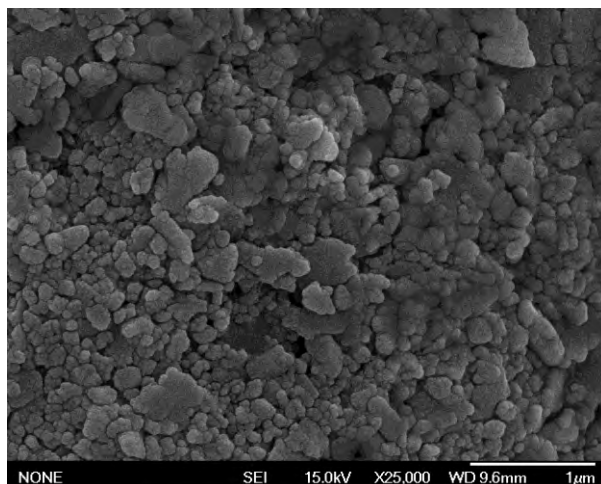


Fig. 2.8 SEM structure of green ceramics.

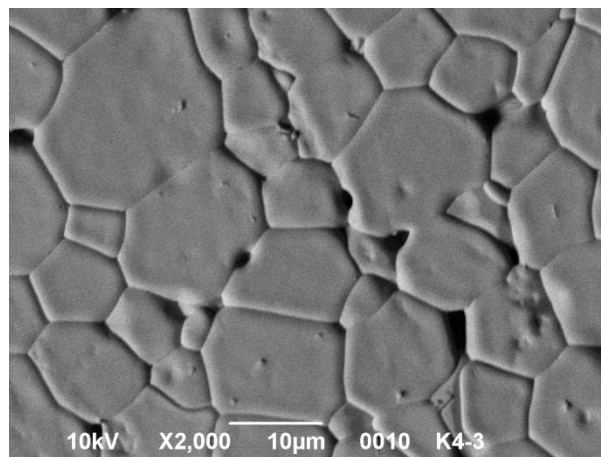


Fig. 2.9 SEM image of thermally etched sintered Nd:LaYO₃ ceramics (density 98.5%)

Table 2.5. Characteristics of sintered samples based on Ln:LaYO₃

Powder sample #	Content of Ln at %	Green density, % of theor.	Cold consolidation mode	Sintering regime, °C or RCS	Transparency of ceramics %	Sintered density, % of theor.
Nd001	1.0	60.1	SC+SMF + CIP	1500 air RCS	55 opaque	98.70 99.61
Nd002	3	59.2	SC+SMF + CIP	1500 air RCS	<50 opaque	98.81 99.48
Nd003	5	58.5	SC+SMF + CIP	1500 air RCS	<50 opaque	97.90 99.18
Nd004	10	59.4	SC+SMF + CIP	1500 air RCS	<55 opaque	96.55 98.97
Yb001	1.0	65.1	CIP SC+SMF + CIP	1500 air RCS	opaque ~45	98.72 99.51
Yb002	3	65.9	CIP	1500 air RCS	opaque <40	98.13 99.47
Yb003	5	64.5	CIP	1500 air RCS	opaque ~45	98.91 99.83
Yb004	10	65.4	CIP	1500 air RCS	opaque ~45	98.50 99.92

CIP – cold isostatic pressing, RCS - rate controlled sintering, SC – slip casting, SMF – strong magnetic field.

Discussion of sintering results.

Samples of all compositions (Table 2.5) were sintered above 1580 °C, i.e. 20 °C higher than decomposition point for pure LaYO₃. Here we supposed that the dopants increase the decomposition temperatures for the perovskite phases. The Nd₂O₃ and Yb₂O₃ dopants substitute in the lattice of LaYO₃ three-valent ions of La³⁺ and Y³⁺. Following phase diagram research, the homogeneity field of R phase is directed to the Nd₂O₃ corner of the diagram of the La₂O₃-Y₂O₃-Nd₂O₃ system, respectively. This means that the ionic substitution in the sites A and B occurs

equally. In the $\text{La}_2\text{O}_3\text{-Y}_2\text{O}_3\text{-Yb}_2\text{O}_3$ system, ions of Yb^{3+} substitute Y^{3+} ions in the B site only. It has been revealed that the phase Nd:LaYO_3 is not stable at 1600 °C: the mixture of other phases than Nd:LaYO_3 has been found. By the stability reasons for textured structure of R phase, the sintering temperature of the Nd:LaYO_3 should not exceed 1500-1530 °C. Unfortunately, this temperature is not enough to get fully dense transparent ceramics even starting from nanosize powders and applying different oxygen partial pressures. In the case of the phase Yb:LaYO_3 , the sintering temperature can be much higher than 1600 °C, because small size ytterbium ion makes LaYO_3 more stable at high temperatures.

The main accent in research has been focused on optimization of pore size evolution to find the best sintering regimes. The idea concerns minimizing the average pore size and maximizing the number of pores at current porosity to get fully dense nanoceramics at moderate temperatures. Using undersintered samples, we applied the BJH method to control the pore size distribution and the number of pores in the porosity range of 10-20% in the samples obtained at various ramp-and-hold regimes of sintering. Open porosity only was found at 20% total porosity was found independently on heating mode. The heating rates higher than 12 °C/min resulted in premature pinching off of channel pores at total porosity 17% and formation of isolated coarse-size pores. The same effect has been revealed at lower heating rates than 0.3 °C/min. The best pore size distribution (narrow and minimal average pore size of 35 nm) was found for multistep sintering regime, which exploited rapid heating to residual porosity of 22%, then switching to three times slower heating rate until sintering in porosity 17%, then decreasing heating rate two times until porosity 8.5% followed by isothermal sintering until porosity less than 0.1%. The best transparency achieved for Nd:YAG ceramics was 67%. This figure was supposed to be improved using RCS regime and sintering under controlled oxygen partial pressure conditions. The series of sintering experiments has been continued under controlled oxygen partial pressure. It has been revealed that oxygen influences non-linearly on sintering rate: at low relative density the densification rate increases with oxygen partial pressure decrease and at high relative density faster densification and slower grain growth occurs at lower oxygen partial pressure. For the first stage the highest densification rate corresponds to $p\text{O}_2=10^{-1}$ atm. and for the second stage where almost all porosity is closed, the best partial pressure is equal to $p\text{O}_2=10^{-12}$ atm corresponding to near full density (99.95%). Thus, to get dense and transparent garnet and perovskite ceramics, it is useful to control densification rate (rate-controlled algorithm) and keep variable oxygen partial pressure. The as prepared both Nd:YAG and Nd:LaYO_3 ceramics are of 99.95% dense. The 0.06 neodymia doped garnet samples showed good transparency of 70-72% after RCS combined with two-step sintering and isothermal holds for 2-12 hours at 1700 °C (Fig. 2.10).

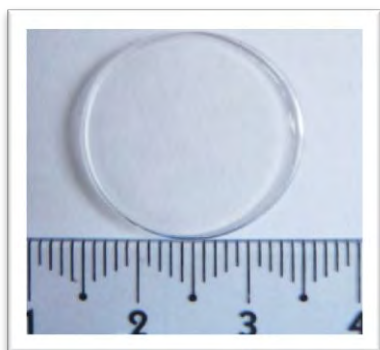


Fig. 2.10 The 006Nd:YAG RCS transparent sample.

The Yb:LaYO_3 phase textured under strong magnetic field has demonstrated the best density of the sintered ceramics in the range 99.0-99.9 after the rate controlled sintering. The samples were found semi-transparent (general transparency is less than 45%), but along c-axis perpendicular to tablet plane it is much higher but difficult to be measured (thin tablets). New batch of samples prepared under strong magnetic field is required to measure optical and luminescent properties.

In spite of high relative density achieved for all samples (many samples are denser than 99% of theoretical value), they remain semitransparent and opaque because of several reasons: refraction in non-isotropic solids is variable and grains in non-isotropic ceramics are too big to allow ceramics to be transparent. The semitransparent samples, however, were obtained right after slip casting in magnetic field. We believe, the semi-chaotic/semi-ordered slip casted Nd:LaYO₃ samples become semi-transparent. The randomly packed particles and grains after CIP and sintering remained opaque in spite of pore-less state. This means that experimentally we are on the right way to get textured transparent optical material. To achieve higher transparency, the more durable sintering regime (50 and more hours) will be required.

Conclusions

1. With the aid of X-ray phase analysis, petrography and electron microscopy phase equilibria in ternary ZrO₂-CeO₂-La₂O₃, ZrO₂-CeO₂-Eu₂O₃, ZrO₂-CeO₂-Gd₂O₃ systems and boundary binary ZrO₂-Gd₂O₃, CeO₂-La₂O₃, CeO₂-Eu₂O₃, CeO₂-Gd₂O₃ systems have been studied in the whole interval of concentrations at temperatures 1500-600 °C.
2. The phase diagram of the ZrO₂-Gd₂O₃ system has been developed. In the ZrO₂-Gd₂O₃ system at 1500 °C there had been found fields of solid solutions based on tetragonal (T) and cubic (F) modifications of ZrO₂, monoclinic (B) and cubic (C) modifications of Gd₂O₃ and ordered phase, which crystallized in the cubic structure of pyrochlore type Gd₂Zr₂O₇ (Py). Lattice parameters were calculated for all phases formed. The state of liquidus of the system has been confirmed from microstructure analysis of the melted/crystallized samples.
3. The isothermal sections of the ZrO₂-CeO₂-La₂O₃ system were studied at 1450, 1250, 1100 °C and of the ZrO₂-CeO₂-Gd₂O₃ system at 1450 and 1100 °C.
4. There has been found that in the ZrO₂-CeO₂-La₂O₃ system at 1500-1100 °C the following fields of solid solutions exist: monoclinic (M) and tetragonal (T) ZrO₂, hexagonal (A) La₂O₃, cubic, fluorite-type (F) CeO₂ and ordered phase La₂Zr₂O₇ of the pyrochlore type.
5. In the system ZrO₂-CeO₂-Gd₂O₃ at 1450, 1100 °C, the following solid solutions were studied: monoclinic (B and M), tetragonal (T), cubic (C and F) REO and ZrO₂, respectively, and the pyrochlore-type intermediate phase Gd₂Zr₂O₇ (Py). It was revealed that in the ZrO₂-CeO₂-Gd₂O₃ system the phases of cubic symmetry predominate such as: F – Fm3m, Py – Fd3m, C - Ia3.
6. First phase reactions in the boundary binary systems CeO₂-La₂O₃, CeO₂-Eu₂O₃, CeO₂-Gd₂O₃ were studied at the following temperatures: 1500, 1100, 600 °C. Lattice parameters were studied versus concentrations and refraction indexes has been established for several solid solutions.
7. In the system CeO₂-La₂O₃ at 1500-1100 °C two types of solid solutions form: cubic, fluorite-type F-CeO₂ and hexagonal A-La₂O₃, which are divided by two-phase field (A+F)
8. The solid phase reaction of CeO₂ (fluorite, F) and Eu₂O₃ (monoclinic, B) showed, that in the CeO₂-Eu₂O₃ system at 1500 °C three types of solid solutions are formed: cubic of fluorite type F-CeO₂ and C-Eu₂O₃, as well as monoclinic B-Eu₂O₃, divided by two-phase fields (F+C) and (C+B). B phase of Gd₂O₃ was established to exist until 1000 °C.
9. In the system CeO₂-Eu₂O₃ at temperatures 600-1500 °C in the concentration range from 0 to 15 mol % Eu₂O₃ the cubic solid solution F-CeO₂ formed. For these solid solutions F-CeO₂ grain size remains in the nanoscale range from 41 to 81 nm.
10. First the solid phase reaction between CeO₂ and Gd₂O₃ at temperatures 1500-600 °C the following solid solutions are formed: cubic, fluorite type F-CeO₂ and C- Gd₂O₃, monoclinic B-Gd₂O₃.
11. The solubility of Gd₂O₃ in F- CeO₂ achieved ~10 mol % at 1100 °C and 15 mol % at 1500 °C. At 600 °C two types of solid solutions were found: cubic, fluorite-type F-CeO₂ and C- Gd₂O₃, which divided by two-phase field (F+C).

12. The results can be used for optimization of dopant concentration in the novel composite materials ionic conductors and catalytic systems.
13. The co-precipitation method was used to prepare nanosize powders of Nd:YAG, Nd:LaYO₃ and Yb:LaYO₃ solid solutions. The powders have been prepared and characterized. The nanosize powders of doped Nd:LaYO₃, Nd:Y₃Al₅O₁₂ and Yb:LaYO₃ phases containing various amount of neodymia ranged from 0.06 to 10 at% have been chemically prepared. The particle size distribution has shown mean particle size ranged 10-22 nm assembled to agglomerates of 40-120 nm in size.
14. The as prepared nanopowders were subjected to slip casting technique in strong magnetic field (12T) for anisotropic ceramics, or tape casting technique without fields for isotropic ceramics, annealed, followed by sintered at 1500-1700 °C for 2-12 hours until near full density. The 0.06 neodymia doped garnet samples showed the best transparency of 70-72% after RCS combined with two-step sintering mode. The best density of the sintered ceramics of 99.5-99.9 was achieved for neodymia-doped YAG. The anisotropic ceramics of Yb:LaYO₃ was obtained in near fully dense state, mostly optically semi-transparent or opaque. The best transparency achieved 45%.
15. Further efforts of anisotropic laser ceramics manufacturing are necessary to increase transparency to 80% or higher. This requires much perfect powder synthesis technique and improved other powder manipulation operations mostly control of orientation on slip casting. Sintering technique also needs perfectness of performance to allow reducing the grain growth in anisotropic ceramics and increasing its transparency.

Plan of publications in 2015.

- 1 Andrievskaya E.R., Gusarov V.V., Kornienko O.A., Sameljuk A.V., Sayir A., Phase relation studies in the $\text{ZrO}_2\text{-CeO}_2\text{-La}_2\text{O}_3$ system at 1100 °C // Journal of the American Ceramic Society. – May 2015
- 2 Andrievskaya E.R., Kornienko O.A., Sameljuk A.V., Sayir A. Phase Relation Studies in the $\text{CeO}_2\text{-Er}_2\text{O}_3$ System at 1100-1500 °C // Journal of the European Ceramic Society. – February 2015
- 3 Andrievskaya E.R., Kornienko O.A., Sameljuk A.V., Sayir A. Phase Relation Studies in the $\text{CeO}_2\text{-Eu}_2\text{O}_3$ System at 600-1500 °C // Journal of Materials Science and Engineering A & B, David Publishing Company – February 2015
- 4 Andrievskaya E.R., Kornienko O.A., Sameljuk A.V., Sayir A. Phase Equilibria in the ternary $\text{ZrO}_2\text{-CeO}_2\text{-Eu}_2\text{O}_3$ System at 1500 °C // Journal of the European Ceramic Society - March 2015
- 5 Chudinovich O.V., Andrievskaya E.R., Ragulya A.V., Sayir A. Synthesis of Nd:LaYO_3 and Yb:LaYO_3 nanocrystalline powders. Ceramics International. March 2015
- 6 Andrievskaya E.R., Chudinovich O.V., Kovylyaev V.V., Sayir A. Phase relations in the $\text{La}_2\text{O}_3\text{-Y}_2\text{O}_3\text{-Nd}_2\text{O}_3$ at 1500 °C. Journal of the European Ceramic Society – April 2015
- 7 Ragulya A.V., Andrievskaya E.R., Chudinovich O.V., Sayir A. Fabrication and spectral properties of Yb^{3+} -doped LaYO_3 nanocrystalline transparent ceramics. Optical materials – May 2015

Perspectives of research.

Present results achieved through this project proved prospectiveness of the following works:

The future trends of our research are grounded on understanding the following advantages. Advanced ceramic approaches enable producing of composite laser ceramics with waveguide, laminar-structured, gradient doping for new pumping architectures [A.Ikesue, Y.L.Aung, Ceramic laser materials, Nature Photonics **2** (2008) 721-727.]. This is why some experts predict that in near future most solid-state lasers may be built with ceramic materials [Research Opportunities in High Energy and High Average Power Lasers High Average Power Lasers / Study for the Air Force Office of Scientific Research, 2009.]. Moreover, near pore-free transparent ceramics even with non-cubic structure (anisotropic) can be obtained by ceramic processing as textured materials as new host for solid-state lasers which cannot be grown by traditional melt methods [G.L. Messing, A.J. Stevenson, Toward pore-free ceramics, Science **322** (2008) 383–384. T. Taira, Domain-controlled laser ceramics toward Giant Micro-photonics, OPTICAL MATERIALS EXPRESS **5** (2011) 1040-1050.].

Preliminary experiments were helpful to reveal several challenges of obtaining the textured and transparent ceramics based on anisotropic (non-cubic) phases such as LaYO_3 : i) synthesis of highly

crystalline and submicron size particles valid for colloidal orientation in strong magnetic field; this search has been finished during the present project, nevertheless the control of stoichiometry for LaYO_3 doped with REO is still open because of water sorption by REO ii) search of sintering mode (including controlled oxygen partial pressure) valid to get near fully dense transparent ceramic is in progress. Neodymium oxide was found to worsen stability of the LaYO_3 phase. We came to conclusion that rare earth ions with smaller ionic size than Nd^{3+} must be used as laser dopants, such as Eu^{3+} and Yb^{3+} .

Complex oxide phases $\text{LnLn}'\text{O}_3$ ($\text{Ln}, \text{Ln}'=\text{Rare Earth Ions}$) with perovskite structure possess unique combination of electrical, magnetic and optical properties. They are promising materials as high-K dielectrics materials. The proposed systems have not been studied as potential optical materials.

Study of the phase equilibria in the ternary systems $\text{Ln}':\text{LaLnO}_3$, where $\text{Ln}=\text{Ho}, \text{Tm}, \text{Lu}$, but $\text{Ln}'=\text{Eu}, \text{Yb}, \text{Dy}$. The physic-chemical properties of compounds formed in the systems as well as ordering and decomposition temperatures of perovskite-like phases (LaLnO_3) doped by Dy^{3+} , Eu^{3+} and Yb^{3+} will be studied. The optimal compositions to produce optical ceramics will be determined and transparent ceramics will be obtained by nonconventional consolidation methods.

1. Study the perovskite-like phase stability depending the temperature and ionic radii of dopant;
2. further manufacturing steps of anisotropic and textured laser ceramics based on LaLnO_3 compounds using slip casting in magnetic field followed by special sintering techniques;
3. study of stability the LaLnO_3 phases against temperature and laser dopant concentration;
4. Microwave sintering of optical ceramics in the atmosphere with controlled partial pressure of oxygen.

The proposed lasers will significantly improve measurement accuracy of distances as well as implement new modes of laser processing of materials, and to create a qualitatively new optical storage media. Potential consumers of ceramic-based microchip lasers are the companies that are developing laser range finders and radar systems, organizations involved in laser processing of materials, research institutes developing optical processing, information transmission and storage systems.

References:

Introduction

1. Stevens R. Introduction to zirconia // Magnesium Electron Publication, №113. - 1986.- 51 p.
2. Hannink R.H.J., Kelly P.M., Muddle B.C. Transformation toughening in zirconia-containing ceramics // J. Am. Ceram. Soc. - 2000. - Vol. 83, №3. - P. 461-487.
3. Raghavan S., Wang H., Porter W. D., Dinwiddie R. B. and Mayo M.J. Thermal properties of zirconia co-doped with trivalent and pentavalent oxides // Acta mater. – 2001. – Vol. 49. P. 169–179.
4. Zhu D. and Miller R. Development of Advanced Low Conductivity Thermal Barrier Coatings // Int. J. Applied Ceramic Technology. – 2004. – Vol. 1, No. 1. – P. 86-94.
5. Evans A.G. et al. Mechanisms controlling the durability of thermal barrier coatings.// Progress in Materials Science. - 2001.- Vol. 46. P. 505-553.
6. Vassen R., Stoeber D. Conventional and new materials for thermal barrier coatings // functional gradient materials and surface layers prepared by fine particles technology / ed. M.-I. Baraton, I. Uvarova / NATO-ASI Series II: Mathematics, Physics and Chemistry. - Dordrecht: Kluwer Academic Publishers.- 2001. - Vol. 16. P. 199-218.
7. Maguire E., Gharbage B., Marques F.M.B., Labrincha J.A. Cathode materials for intermediate temperature SOFCs // Solid State Ionics. - 2000. - Vol. 127. - P. 329-335.
8. Ozawa M., Effect of aging temperature on CeO₂ formation in homogeneous precipitation // J. Mater. Sci. – 2004. – Vol. 39. – P. 4035-4036.
9. Singh J., Wolfe D.E., Miller R.A., Eldridge J.I., Dong-Ming ZHU, Tailored microstructure of zirconia and hafnia-based thermal barrier coatings hemispherical reflectance by EB-PVD // J. Mater. Sci. – 2004. – Vol. 39. – P. 1975-1985.
10. Kharton V.V., Figueiredo F.M., Navarro L., Naumovich E.N., Kovalevsky A.V., Yaremchenko A.A., Viskup A.P., Garneiro A., Marques F.M.B., Frade J.R., Ceria-based materials for solid oxide fuel cells // J. Mater. Sci. – 2001. – Vol. 36. – P. 1105-1117.
11. Cao X.Q., Vassen R., Tietz F., Stoeber D., New double-ceramic-layer thermal barrier coatings based on zirconia-rare earth composite oxides // J. Europ. Ceram. Soc. – 2006. – Vol. 26. – P. 247-251.
12. Sato K., Yugami H., Hashida T., Effect of rare-earth oxides on fracture properties of ceria ceramics // J. of Materials Science. – 2004. - Vol. 39. – P. 5765-5770.
13. Ranløv J. Comment on “The characterization of doped CeO₂ electrodes in solid oxide fuel cells” by B.G. Pound, / J. Ranløv, F. W. Poulsen, M. Mogensen // Solid State Ionics – 1993. – Vol. 61. - P. 277-279.
14. Chavan S.V. Phase relations and lattice thermal expansion studies in the Ce_{0.50}RE_{0.50}O_{1.75} (RE = rare-earths) / S.V. Chavan, A.K. Tyagi // Materials Science and Engineering: A – 2005 - Vol. 404 – P. 57-63.
15. Wang Ch., Experimental and computational phase studies of the ZrO₂-based systems for thermal barrier coatings // Ph.D. Thesis, University of Stuttgart, 2006.
16. Harrison P. G., Kelsall A., and Wood J. V., Chemical Microengineering in Sol–Gel Derived Fluoride and Lanthanide Modified Ceria Materials // J. Sol–Gel Sci. Technol. – 1998. – Vol. 13. – P. 1049-1055.
17. Bevan D. J. M., Barker W. W., Martin R. L., and Parks T. C. Mixed Oxides of the type MO₂ (Fluorite)-M₂O₃ // In: Proceedings of the Fourth Conference on Rare Earth Research, Phoenix, Ariz., 1964. Edited by L. Eyring. Phoenix, AZ, Gordon and Breach, New York, 1965. - Vol. 3. – P. 441.
18. Prabhakaran Sree Kumari Anjana Microwave dielectric properties of (1-x) CeO_{2-x} RE₂O₃ (RE=La, Nd, Sm, Eu, Gd, Dy, Er, Tm, Yb, and Y) (0 ≤ x ≤ 1) ceramics / Prabhakaran Sree Kumari Anjana, Tony Joseph, Mailadil Tomas Sebastian // Journal of Alloys and Compounds. – 2010. - Vol. 490. – P. 208-213.
19. Stefano Maschio, Eleonora Aneggi, Alessandro Trovarelli, Valter Sergo. Influence of erbia or europia doping on crystal structure and microstructure of ceria-zirconia (CZ) solid solutions // Ceramics International. – 2008. - Vol. 34. – P. 1327-1333.
20. Inaba H. Ceria-based solid electrolytes / Inaba H., Tagawa H. //Solid State Ionics - 1996 – Vol. 83 – P.1-16.
21. Godikemeiker M. Electrochemical characteristics of cathodes in solid oxide fuel cells based on ceria electrolytes / Godikemeiker M., Sasaki K., and Guackler L.J., // Journal Electrochem. Soc. – 1997 –Vol. 144, P. 1635-1646.
22. Hiroshi Yamamura. AC Conductivity for Eu₂Zr₂O₇ and La₂Ce₂O₇ with Pyrochlore-Type Composition / Hiroshi Yamamura, Hanako Nishino, Katsuyoshi Kakinuma // Journal of the Ceramic Society of Japan – 2003 – Vol. 111, № 12 - P. 907-911.
23. Dirstine R.T., Blumenthal R.N., Kuech T.F. Ionic conductivity of calcia, yttria and rare-earth-doped cerium dioxide // Journal Electrochemical Society – Vol. 126 -№ 2 - 1979 – P. 264-269
24. Андриевская Е.Р. Фазовые равновесия в системах оксидов гафния, циркония и иттрия с оксидами редкоземельных элементов // Монография. Киев. – 2010. – изд. Наукова думка. 470 с.
25. Traverse J.P. Etude du Polymorphisme des sesquioxides de terres rares / Traverse J.P.: These. Grenoble. - 1971. - 150 p.
26. Balaji P. Phase relations, lattice thermal expansions in Ce_{1-x}Sm_xO_{2-x/2} systems and stabilization of cubic RE₂O₃ (RE: Eu, Sm) / Balaji P. Mandal, V. Grover, A. K. Tyagi // Materials Science and Engineering A - 2006 – Vol. 430 - P. 120-124.

27. Hiroshi Yamura. Crystal Phase and Electrical Conductivity in the Pyrochlore-Type Composition Systems, $\text{Ln}_2\text{Ce}_2\text{O}_7$ (Ln = La, Nd, Sm, Eu, Gd, Y and Yb) / Hiroshi Yamura, Hanako Nishino, Katsuyoshi Kakinuma, Katsuhiko Nomura // Journal of the Ceramic Society of Japan - 2003 – Vol. 111, №12, P. 902-906.

System $\text{ZrO}_2\text{-CeO}_2\text{-Eu}_2\text{O}_3$

28. Диаграммы состояния систем тугоплавких оксидов: Справочник. Вып. 5. Двойные системы. Ч.3 / Ин-т химии силикатов им. И.В. Гребенщикова – Л.: Наука, 1987. - С. 264.
29. Kuto T., Obayashi H. Oxygen Ion conduction of fluorite-Type $\text{Ce}_{1-x}\text{Ln}_x\text{O}_{2-x/2}$ (Ln= lanthanide Element) // J. Electrochem. Soc. – Vol. 122 – 1975 – P. 142-147.
30. Hiroshi Yamamura, Hanako Nishino, Katsuyoshi Kakinuma and Katsuhiko Nomura. Crystal Phase and Electrical Conductivity in the Pyrochlore-Type Composition Systems, $\text{Ln}_2\text{Ce}_2\text{O}_7$ (Ln = La, Nd, Sm, Eu, Gd, Y and Yb) // Journal of the Ceramic Society of Japan. - 2003. – Vol. 111, N 12. - P. 902-906.
31. Masaki N., Guillermo N.R.D., Ootobe H., Nakamura A., Izumiyama Y., Hinatsu Y. ^{151}Eu -Mössbauer spectroscopic study of the fluorite-type oxide solid solutions, $\text{Eu}_y\text{M}_{1-y}\text{O}_{2-y/2}$ (M = Zr, Ce) ($0 \leq y \leq 1.0$), in: P. Vincenzini, V. Buscaglia, (Eds.) // Proceedings of Mass and Charge Transport in Inorganic Materials: Fundamental to Devices, Techna Srl (2000). – P. 1233-1240.
32. Masaki N.M., Ootobe H., Nakamura A., Guillermo N.R.D., Izumiyama Y., Harada D., Hinatsu Y. ^{151}Eu -Mössbauer spectroscopic and XRD study on some fluorite-type solid solution systems $\text{Eu}_y\text{M}_{1-y}\text{O}_{2-y/2}$ (M = Zr, Hf, Ce). // Hyperfine Interact. – 2003. - (C). – P. 305-308.
33. Ashok Kumar Baral, V. Sankaranarayanan. Ionic Transport Properties in Nanocrystalline $\text{Ce}_{0.8}\text{A}_{0.2}\text{O}_{2-\delta}$ (with A = Eu, Gd, Dy, and Ho) Materials // Nanoscale Res Lett. – 2010. – Vol. 5 – Issue 3 - P. 637–643.
34. Masakia N.M., Nakamura A., Furuuchib F., Hinatsu Y. ^{151}Eu -Mössbauer spectroscopic and X-ray diffraction study of the $\text{Eu}_2(\text{Ce}_{1-x}\text{Zr}_x)_2\text{O}_7$ and $\text{LnEuZr}_2\text{O}_7$ (Ln = lanthanide) systems // Journal of Physics and Chemistry of Solids. – 2005. – Vol. 66. – P. 312–317.
35. Pepin J.G., Vance E.R., McCarthy G.I. Subsolidus phase relations in the systems $\text{CeO}_2\text{-RE}_2\text{O}_3$ (RE_2O_3 = C-type rare earth sesquioxide) // J. Solid State Chem. – 1981. – Vol. 38, N 3. P. 360-367.
36. Longo V., Roitti S., Solid state phase relations in the system $\text{CeO}_2\text{-ZrO}_2$ // Ceramurgia Int. - 1971. - Vol. 1, № 1. - P. 4-10.
37. Tani E., Yoshimura M., Somiya S., Revised phase diagram of the system $\text{ZrO}_2\text{-CeO}_2$ bellow 1400 °C // J. Am. Ceram. Soc. - 1983. - Vol. 66, № 7. - P. 506-510.
38. Duran P., Gonzales M., Moure C., Jurado J.R., Pascual C., A new tentative phase equilibrium diagram for the $\text{ZrO}_2\text{-CeO}_2$ system in air // J. Mater. Sci. - 1990. - Vol. 25. - P. 5001-5006.
39. Андриевская Е.Р., Редько В.П., Лопато Л.М., Взаимодействие оксида церия с оксидами гафния, циркония и иттрия при 1500 °C // Порошковая металлургия. -2001. - № 7/8. – С. 109-118.
40. Panova T.I., Glushkova V.B., Nefedova M.Yu., Investigation into the phase formation in the $\text{ZrO}_2\text{-CeO}_2$ system // Glass Physics and Chemistry. – 2005. – Vol. 31, № 2. – P. 240-245.
41. Андриевская Е.Р. Взаимодействие оксида церия с оксидами циркония и иттрия при 1250 °C / Андриевская Е.Р., Самелюк А.В., Лопато Л.М.// Порошковая металлургия. -2002. - № 1/2. – С. 71-81.
42. Duwez P. Odell F. Phase relationships in the system zirconia-ceria / Duwez P., Odell F. // J. Am. Ceram. Soc. – 1950. - Vol. 33, № 9. – P. 274-283.
43. Rouanet A. Zirconia-cerium oxide system at high temperature / Rouanet A. // C.R. Hebd. Seances Acad. Sci. – 1968. – Ser. C, Vol. 266. - P. 908-911.
44. Roitti S. Investigation of phase equilibrium Diagrams among oxides by means of electrical conductivity measurements. Application of the method to the system $\text{CeO}_2\text{-ZrO}_2$ / Roitti S., Longo V.// Ceramurgia Int. – 1972. – Vol. 2, № 2. – P. 97-102.
45. Longo V. X-ray characterization of $\text{Ce}_2\text{Zr}_3\text{O}_{10}$ / Longo V., Minichelli D. // J. Am. Ceram. Soc. - 1973. - Vol. 56, № 11. - P. 600.
46. Yoshimura M. Phase relations in the system $\text{ZrO}_2\text{-CeO}_2\text{-Iron oxide}$ in air / Yoshimura M., Bowen H.K. // J. Am. Ceram. Soc. Bull. - 1977. - Vol. 56, № 3. - P. 301-305.
47. Stubican V.S. Phase equilibria in some zirconia systems / Stubican V.S., Hellmann J.R. // Advances in Ceramics. Science and Technology of Zirconia. Ed. By Heuer A.H. and Hobbs L.W. The Am. Ceram. Soc. – Columbus, OH. – 1981. – Vol. 3. – P. 25-36.
48. Yoshimura M. The confirmation of phase equilibria in the system $\text{ZrO}_2\text{-CeO}_2$ bellow 1400 °C / Yoshimura M., Tani E., Somiya S. // Solid State Ionics - 1981. - № 3/4. - P. 477-481.
49. Meriani S. A new single-phase tetragonal $\text{CeO}_2\text{-ZrO}_2$ / Meriani S.// Mater. Sci. Eng. – 1985. – Vol. 71. – P. 369-370.
50. Meriani S. Metastable tetragonal $\text{CeO}_2\text{-ZrO}_2$ solid solution / Meriani S. // J. Phys. Supp. – 1986. – Vol. 47, № 2. – P. 485-489.
51. Meriani S. Features of the ceria-zirconia system / Meriani S. // Mater. Sci. Eng. – 1989. – Vol. 109. – P. 121-130.
52. Hannink R.H. Metastability of the martensitic transformation in a 12 mol % ceria-zirconia alloy:I. Deformation and fracture observation / Hannink R.H., Swain M.W. // J. Am. Ceram. Soc. - 1989. - Vol. 72, № 1. - P. 90-98.

53. Swain M.W. Metastability of the martensitic transformation in a 12 mol % ceria-zirconia alloy:II. Grinding Studies / Swain M.W., Hannink R.H.I. // J. Am. Ceram. Soc. - 1989. - Vol. 72, № 8. - P. 1358-1364.
54. Yashima M. Zirconia-ceria solid solutions synthesis and temperature-time-transformation diagram of the 1:1 composition / Yashima M., Morimoto K., Ishizawa N., Yoshimura M. // J. Am. Ceram. Soc. - 1993. - Vol. 76, № 7. - P. 1745-1750.
55. Yashima M. Diffusionless cubic-tetragonal phase transition in the $\text{ZrO}_2\text{-CeO}_2$ system / Yashima M., Morimoto K., Ishizawa N., Yoshimura M. // Science and technology of zirconia. Ed. by Badwal S.P.S., Bannister M.J., Hannink R.H.I. Technomic Publishing Company, Lancaster, PA. - 1993. - Vol. 76, № 7. - P. 108-116.
56. Kim D.J.. Raman spectroscopy of tetragonal zirconia solid solutions / Kim D.J., Jung H., Yang I.S. // J. Am. Ceram. Soc. - 1993. - Vol. 76, № 8. - P. 2106-2108.
57. Yashima M. Raman scattering study of cubic-tetragonal phase transformation in $\text{Zr}_{1-x}\text{Ce}_x\text{O}_7$ solid solution / Yashima M., Arashi H., Kakihana M., Yoshimura M. // J. Am. Ceram. Soc. - 1994. - Vol. 77, № 4. - P. 1067-1071.
58. Yashima M. Synthesis of metastable tetragonal (t') zirconia-ceria solid solutions by the polymerized complex method / Yashima M., Ohtake K., Kakihana M., Yoshimura M. // J. Am. Ceram. Soc. - 1994. - Vol. 77, № 10. - P. 2773-2776.
59. Yashima M. Low-temperature phase equilibria by the flux method and the metastable phase diagram in $\text{ZrO}_2\text{-CeO}_2$ system / Yashima M., Takashina H., Kakihana M., Yoshimura M. // J. Am. Ceram. Soc. - 1994. - Vol. 77, № 7. - P. 1869-1874.
60. Du Y. Thermodynamic Evaluation of the $\text{ZrO}_2\text{-CeO}_2$ system / Du Y., Yashima M., Koura T., Kakihana M., Yoshimura M. // J. Ser. Metall. Mater. - 1994. - Vol. 31, № 3. - P. 327-332.
61. Zhu H.Y. X-ray diffraction study of the $t \rightarrow m$ phase in 12 mol % -ceria-doped zirconia at low temperatures / Zhu H.Y. // J. Am. Ceram. Soc. - 1994. - Vol. 77, № 9. - P. 2458-2460.
62. Dariol G. Solubility of erbium, praeodimium and vanadium in ZrO_2 , $\text{ZrO}_2\text{-CeO}_2$ and $\text{ZrO}_2\text{-Y}_2\text{O}_3$ / Dariol G., Poletto A., Ricciardiello F. Genel, Podda L Kucich. // Key Engineering Materials. - 1997. - Vols. 132-136. - P. 771-774.
63. Rouanet A., Contribution a l'etude des systemes zirconia - oxydes des lanthanides au voisinage de la fusion: Memoire de these // Rev. Intern. Hautes Temp. et Refract. 1971. Vol. 8. - P. 161-180.
64. Perez M., Jorba Y., Contribution a Letude Des Systems Zircone-Oxides De Terres Rares // Annual Chim. - 1962. - Vol. 7, № 7-8. - P. 479-511.
65. Зоз Е.И., Фомигач Е.Н., Калашник А.А., Елисева Г.Г., О структуре и свойствах цирконатов и гафнатов РЗЭ // Ж. Неорган. химии. - 1982. - Т. 27, № 1. - С. 95-99.
66. Пальгугев С.Ф. Электропроводность и числа переноса в системе $\text{CeO}_2\text{-ZrO}_2$ / Пальгугев С.Ф., Волченкова З.С. // Ж. Физической химии. - 1960. - Т. 34. - С. 211-213.
67. Леонов А.И. Влияние газовой среды на взаимодействие двуокиси циркония с окислами церия / Леонов А.И., Андреева А.Б., Келер Э.К. // Изв. АН СССР Неорганические материалы. - 1966. - Т. 11. - С. 137-144.
68. Meriani S. Zirconia-ceria ceramics research and development / Meriani S. // Proc. 12th Int. Technical Colloquium on Ceramics Processing. - Remini. - 1987. - Ceramurgia. - 1987. - Vol. 16. - P. 206.
69. Meriani S. Powder data for metastable ZrCe_4O_7 ($x = 0.84$ to 0.40) solid solutions with tetragonal symmetry / Meriani S., Spinolo G. // Powder Diffr. - 1987. - Vol. 2, № 4. - P. 255-256.
70. Coyle T.W. Transformation toughening in large-grain-size CeO_2 -doped ZrO_2 / Coyle T.W., Coblenz W.S., Bender B.A. // J. Am. Ceram. Soc. - 1988. - Vol. 71. - P. 88.
71. Urabe K. Characteristic Microstructure of CeO_2 and Y_2O_3 -doped tetragonal zirconia polycrystals / Urabe K., Nakajima H., Ikawa H., Ugadawa S. // Advances in Ceramics. - 1988. - Vol. 24, Science and Technology of zirconia III. Ed. By Somiya S., Yamamoto N., Yanagida H. Am. Ceram. Soc. Columbus, OH. - P. 345-355.
72. Duh J.G. Synthesis and sintering behaviour in $\text{CeO}_2\text{-ZrO}_2$ ceramics / Duh J.G., Dai H.-T., Hsu W.-Y. // J. Mater. Sci. - 1988. - Vol. 23. - P. 2786-2791.
73. Duh J.G. Fabrication and sinterability in $\text{Y}_2\text{O}_3\text{-CeO}_2\text{-ZrO}_2$ / Duh J.G., Lee M.Y. // J. Mater. Sci. - 1989. - Vol. 24. - P. 4467-4474.
74. Yoshioka T. Preparation of Spherical ceria-doped tetragonal zirconia by the spray-pyrolysis method / Yoshioka T., Dosaka K., Sato T., Okuwaki A., Tanno S., Miura T. // J. Mater. Sci. Lett. - 1992. - Vol. 11, № 3. - P. 51-55.
75. Theunissen G.S.A. Effect of dopants on the sintering behaviour and stability of tetragonal zirconia ceramics / Theunissen G.S.A., Winnubst A.J.A., Burggraaf A.J. // J. Europ. Ceram. Soc. - 1992. - Vol. 9. - P. 251-263.
76. Scardi P. Thermal expansion anisotropy of ceria-stabilized tetragonal zirconia / Scardi P., Maggio R.Di., Lutterotti L., Maistrelli P. // J. Am Ceram Soc. - 1992. - Vol. 75, № 10. - P. 2828-2832.
77. Kubota Y. Elastic Modulus and fracture toughness of CeO_2 containing tetragonal zirconia polycrystals / Kubota Y., Ashizuka M., Hokazano H. // J. Ceram. Soc. Jpn. - 1994. - Vol. 102, № 2. - P. 175-179.
78. Lin Jyung-Dong Crystallite size and microstrain of thermally aged low-ceria and low-yttria-doped zirconia / Lin Jyung-Dong, Duh Jena-Gong. // J. Am. Ceram Soc. - 1998. - Vol. 81, № 4. - P. 853-860.
79. Kang Z.S. Lattice oxygen transfer in fluorite-type oxides containing Ce, Pr, and / or Tb / Kang Z.S., Eyring L. // J. Solid State Chemistry. - 2000. - Vol. 155. - P. 129-137.
80. Lefevre J. Some structural modifications of fluorite-type phase in the systems based on ZrO_2 or HfO_2 // Annual. Chim. - 1963. - Vol. 8, № 1-2. - P. 254-256.

81. Klee W.E., Weitz G. Infrared spectra of ordered and disordered pyrochlore-type compounds in the series $\text{RE}_2\text{Ti}_2\text{O}_7$, $\text{RE}_2\text{Zr}_2\text{O}_7$ and $\text{RE}_2\text{Hf}_2\text{O}_7$ // J. Inorg. And Nucl. Chem. – 1969. – Vol. 31, № 8. – P. 2367-2372.
82. Жидовинова С.В. Сравнительная характеристика фазообразования при взаимодействии окислов РЗЭ и иттрия с окислами циркония и гафния // Автореферат дис. ... канд. хим. наук: Ин-т электрохимии УНЦ АН СССР. – Свердловск, 1974. – 16с.
83. Зоз Е.И., Фомичев Е.Н., Калашник А.А., Елисеєва Г.Г. О структуре и свойствах цирконатов и гафнатов РЗЭ // Ж. Неорган. химии. – 1982. – Т. 27, № 1. – С. 95-99.
84. Andrievskaya E.R., Lopato L.M. The systems $\text{ZrO}_2(\text{HfO}_2)\text{-Eu}_2\text{O}_3$ // Proc International Conf. “Deformation and Fracture in Structural PM Materials with a Workshop on their Application”. Stará Lesná (Slovakia). – 1996. – Vol. 2. – Košice: IMR-SAS. – 1996. – P. 296-301.
85. Andrievskaya E.R., Lopato L.M. Phase transformations in the ternary systems $\text{HfO}_2(\text{ZrO}_2)\text{-Y}_2\text{O}_3\text{-Eu}_2\text{O}_3$ // Key engineering materials – Switzerland: Trans Tech Publications. – 1997. – Vols. 132-136. – P. 1782-1785.
86. Perez-y-Jorba M. $\text{ZrO}_2\text{-rare earth oxides}$ systems // Annual Chim. – 1962. – Vol. 7, № 7-8. – P. 479-511.
87. Michel D., Rouaux Y., Perez-y-Jorba M. Ceramic eutectics in the system $\text{ZrO}_2\text{-Ln}_2\text{O}_3$ (Ln – Lanthanide): Unidirectional solidification, microstructural and crystallographic characterization // J. Mater. Sci. – 1980. – Vol. 15. – P. 61-66.
88. Andrievskaya E.R. Phase relations and nanocrystalline alloys in the ternary systems $\text{ZrO}_2(\text{HfO}_2)\text{-Y}_2\text{O}_3\text{-La}_2\text{O}_3(\text{Eu}_2\text{O}_3, \text{Er}_2\text{O}_3)$ // Functional gradient materials and surface layers prepared by fine particles technology. – London: Kluwer Academic Publishers. – 2001. – Vol. 16. – P. 305-312.
89. Стегний А.И., Шевченко А.В., Лопато Л.М., Рубан А.К., Дверняков В.С., Пасичный В.В. Термический анализ окислов с использованием солнечного нагрева // Докл. АН УССР. – 1979. – Сер. А, № 6. – С. 484-489.
90. Barry E.S., William B. White characterization of anion disorder in zirconate $\text{A}_2\text{B}_2\text{O}_7$ compounds by raman spectroscopy // J. Am. Ceram. Soc. – 1979. – Vol. 62. – P. 468-469.
91. Глушкова В.Б., Сазонова Л.В. Влияние добавок редкоземельных окислов на полиморфизм двуокиси циркония // Химия высокотемпературных материалов. – Л.: Наука, 1967. – С. 83-90.
92. Давтян И.А., Глушкова В.Б., Келер Э.К. Влияние добавок окиси европия на полиморфизм двуокиси циркония // Изв. АН СССР. Неорган. материалы. – 1966. – Т. 2, № 5. – С. 890-897.
93. Портной К.И., Тимофеева Н.И., Салибеков С.Е. Синтез и исследование сложных оксидов и циркония // Изв. АН СССР. Неорган. материалы. – 1972. – Т. 8, № 2. – С. 406-408.
94. Faucher M., Caro P. Ordre et desordre dans certains composés du type pyrochlore // J. Solid State Chem. – 1975. – Vol. 12, № 1-2. – P. 1-11.
95. Кипарисов С.С., Беляев Р.А., Беляков А.И., Бондаренко В.В., Выскубов В.П., Козлов В.Г., Кузнецов С.А., Мелихова Л.П. Диаграмма состояния системы $\text{Eu}_2\text{O}_3\text{-ZrO}_2$ // Изв. АН СССР. Неорган. материалы. – 1976. – Т. 12, № 9. – С. 1693-1694.
96. Лопато Л.М., Андриевская Е.Р., Шевченко А.В., Редько В.П. Фазовые соотношения в системе $\text{ZrO}_2\text{-Eu}_2\text{O}_3$ // Ж. Неорган. химии. – 1997. – Т. 42, № 10. – С. 1736-1739.
97. Andrievskaya E.R. Phase Equilibria in the Refractory Oxide Systems of zirconia, hafnia and yttria with Rare-earth Oxides // Journal of the European Ceramic Society. – 2008. – Vol. 28, № 12. – P. 2363-2388.
98. Andrievskaya E.R., Lopato L.M., Influence of composition on the T→M transformation in the systems $\text{ZrO}_2\text{-Ln}_2\text{O}_3$ (Ln = La, Nd, Sm, Eu) // J. Mater. Sci. – 1995. – Vol. 36, № 10. – P. 2591-2596.

System $\text{ZrO}_2\text{-CeO}_2\text{-Gd}_2\text{O}_3$

1. Mohamed N. Rahman, Jacob R. Gross, Rollie E. Dutton, Hsin Wang, Phase stability, sintering, and thermal conductivity of plasma-sprayed $\text{ZrO}_2\text{-Gd}_2\text{O}_3$ compositions for potential thermal barrier coating applications // Acta Materialia. – 2006. – Vol. 54. – P. 1615-1621.
2. Sreya Dutta, Santanu Bhattacharya, D.C. Agrawal, Electrical properties of $\text{ZrO}_2\text{-Gd}_2\text{O}_3$ ceramics // Materials Science and Engineering. – 2003. – B100. – P. 191-198.
3. Junhu Wang, Akio Nakamura, Masuo Takeda, Structural properties of the fluorite- and pyrochlore-type compounds in the $\text{Gd}_2\text{O}_3\text{-ZrO}_2$ system $x\text{GdO}_{1.5-(1-x)}\text{ZrO}_2$ with $0.18 \leq x \leq 0.62$ // Solid State Ionics. – 2003. – Vol. 164. – P. 185-191.
4. S.J. Patwe, B.R. Ambekar, A.K. Tyagi, Synthesis, characterization and lattice thermal expansion of some compounds in the system $\text{Gd}_2\text{Ce}_x\text{Zr}_{2-x}\text{O}_7$ // J. of Alloys and Compounds. – 2005. – Vol. 389. – P. 243-246.
5. Junhu Wang, Haruyoshi Ohtobe, Akio Nakamura, and Masuo Takeda, Correlation of crystal structures with electric field gradients in the fluorite- and pyrochlore-type compounds in the $\text{Gd}_2\text{O}_3\text{-ZrO}_2$ system // J. Solid State Chemistry. – 2003. – Vol. 176. – P. 105-110.
6. R.M. Leckie, S. Krämer, M. Rühle, C.G. Levi, Thermochemical compatibility between alumina and $\text{ZrO}_2\text{-Gd}_2\text{O}_{3/2}$ thermal barrier coatings // Acta Materialia. – 2005. – Vol. 53. – P. 3281-3292.
7. А.Г. Караулов, Е.И. Зоз, Т.М. Шляхова, Структура и свойства огнеупоров на основе диоксида циркония, стабилизированного оксидом гадолиния // Огнеупоры и техническая керамика. – 1996. – № 3. – С. 12-16.

8. A.G. Karaulov, E.I. Zoz, Phase formation in the $\text{ZrO}_2\text{-HfO}_2\text{-Gd}_2\text{O}_3$ and $\text{ZrO}_2\text{-HfO}_2\text{-Yb}_2\text{O}_3$ systems // *Refract. And Ceram.* – 1999. – Vol. 40. – P. 479-483.
9. A. Rouanet, Contribution a l'etude des systemes zirconia - oxydes des lanthanides au voisinage de la fusion: Memoire de these // *Rev. Intern. Hautes Temp. et Refract.* 1971. Vol. 8. - P. 161-180.
10. A. Rouanet, M. Foex, Study at High Temperature of Systems formed by Zirconia with Samarium and Gadolinium Sesquioxides // *C.R. Acad. Sci. Paris, Ser. C.* – 1968. - Vol. 267, № 15. – P. 873-876.
11. M. Zinkevich, Ch. Wang, F.M. Morales, M. Rühle, F. Aldinger, Phase equilibria in the $\text{ZrO}_2\text{-GdO}_{1.5}$ system at 1400-1700 °C // *J. of Alloys and Compounds.* – 2005. – Vol. 398. – P. 261-268.
12. Ch. Wang, M. Zinkevich, O. Fabrichnaya, F. Aldinger, Experimental investigation and thermodynamic modeling in the $\text{ZrO}_2\text{-GdO}_{1.5}$ system // *In Calphad XXXIII Program and Abstracts.* – 2004. – P. 88.
13. H.G. Scott, On the continuous transition between two structure types in the zirconia-gadolinia system // *J. Mater.Sci.* - 1978. - Vol. 13. - P. 1592-1593.
14. T. Mogira, S. Emura, A. Yoshiasa, S. Kikkawa, F. Kanamaru, K. Koto, X-ray and Raman Study of Coordination States of Fluorite - and Pyrochlore - Type Compounds in the System $\text{ZrO}_2\text{-Gd}_2\text{O}_3$ // *Solid State Ionics.* - 1990. – Vol. 40. - P. 357-361.
15. Sergey V. Ushakov, Alexandra Navrotsky, Jean A. Tangeman, Kathryn B. Helean, Energetics of defect fluorite and pyrochlore phases in lanthanum and gadolinium hafnates // *J. Am. Ceram. Soc.* – 2007. - Vol. 90, № 4. - P. 1171-1176.
16. Raja Kishora Lenka, Tarasankar Mahata, Pankaj Kumar Sinha, Beant Prakash Sharma, Combustion Synthesis, Powder Characteristics, and Shrinkage Behavior of a Gadolinia - Ceria System // *J. Am. Ceram. Soc.* – 2006. – Vol. 89, № 12. - P. 3871-3873.
17. T.S. Zhang, J. Ma, H. Cheng, S.H. Chan, Ionic conductivity of high-purity Gd-doped ceria solid solutions // *Materials Research Bulletin.* – 2006. – Vol. 41. – P. 563-568.
18. S. Dikmen, P. Shuk, M. Greenblatt, H. Gocmez, Hydrothermal synthesis and properties of $\text{Ce}_{1-x}\text{Gd}_x\text{O}_{2-\delta}$ solid solutions // *Solid State Sciences.* – 2002. – Vol. 4. – P. 585-590.
19. E. Gourba, Ringuedé, M. Cassir, A. Billard, J. Päiväsäari, J. Niinistö, M. Putkonen, L. Niinistö, Characterization of Thin Films of Ceria-Based Electrolytes for Intermediate Temperature – Solid Oxide Fuel Cells (IT-SOFC) // *Ionics.* – 2003. Vol. 9. – P. 15-20.
20. Zhang Tianshu, Peter Hing, Haitao Huang, J. Kilner, Ionic conductivity in the $\text{CeO}_2\text{-Gd}_2\text{O}_3$ system ($0.05 \leq \text{Gd}/\text{Ce} \leq 0.4$) prepared by oxalate coprecipitation // *Solid State Ionics.* - 2002. – Vol. 148. - P. 567-573.
21. R. Ball, R. Stevens, Characterization of $\text{Ce}_{0.8}\text{Gd}_{0.2}\text{O}_{1.9}/3\text{Y-TZP}$ composite electrolytes-effects of weight % 3Y-TZP particles // *J. Materials Sci.* – 2003. – Vol. 38. – P. 1413-1423.
22. E.V. Tsipis, V.V. Kharton, I.A. Bashmakov, E.N. Naumovich, J.R. Frade, Cellulose-precursor synthesis of nanocrystalline $\text{Ce}_{0.8}\text{Gd}_{0.2}\text{O}_{2-\delta}$ for SOFC anodes // *J. Solid State Electrochem.* – 2004. – Vol. 8. – P. 674-680.
23. M.G. Chourashiya, J.Y. Patil, S.H. Pawar, L.D. Jadhav, Studies on structural, morphological and electrical properties of $\text{Ce}_{1-x}\text{Gd}_x\text{O}_{2-(x/2)}$ // *Materials Chemistry and Physics.* – 2008. – Vol. 109. – P. 39-44.
24. J. Liu, W. Weppner, Electronic Conductivity Measurement of Gadolinia Doped Ceria by DC-Partial-Polarization // *Ionics.* – 1999. – Vol. 5. – P. 115-121.
25. Emma Rossinyol, Eva Pellicer, Anna Prim, Sònia Estradé, Jordi Arbiol, Francesca Peiró, Albert Cornet, Joan Ramon Morante, Gadolinium doped Ceria nanocrystals synthesized from mesoporous silica // *J. Nanopart. Res.* – 2008. – Vol. 10. – P. 369-375.
26. V.P. Gorelov, S.V. Zayats, V.V. Ivanov, S.Yu. Ivin, Yu. Kotov, A.I. Medvedev, N.I. Moshkalenko, A. M. Murzakaev, O.M. Samatov, V.R. Khrustov, Gadolinium-Doped Ceria Ceramics with Submicron Structure for Electrochemical Applications // *Glass Physics and Chemistry.* – 2005. - Vol. 31, № 4. – P. 471-476.
27. V. Grover, A.K. Tyagi, Phase relations, lattice thermal expansion in $\text{CeO}_2\text{-Gd}_2\text{O}_3$ system, and stabilization of cubic gadolinia // *Materials Research Bulletin.* – 2004. Vol. 39. – P. 859-866.
28. V. Grover, A.K. Tyagi, Phase relations studies in the $\text{CeO}_2\text{-Gd}_2\text{O}_3\text{-ZrO}_2$ system // *Solid State Chemistry.* – 2004. - Vol. 177. – P. 4197-4204.
29. Wang Ch., Zinkevich M., Aldinger F. Phase diagrams and thermodynamics of rare-earth-doped zirconia ceramics // *Pure Appl. Chem.* - 2007. - Vol. 79, №. 10. - P. 1731-1753.

Optically transparent ceramics

1. S. J. McNaught, H. Komine, S. B. Weiss, R. Simpson, A. M. F. Johnson, J. Machan, C. P. Asman, M. Weber, G. C. Jones, M. M. Valley, A. Jankevics, D. Burchman, M. McClellan, J. Sollee, J. Marmo, and H. Injeyan, in 2009 Conference on Lasers and Electro-Optics and Quantum Electronics and Laser Science Conference (CLEO/QELS 2009) (IEEE, 2009).
2. Jun Akiyama,* Yoichi Sato, and Takunori Taira Laser ceramics with rare-earth-doped anisotropic materials // *OPTICS LETTERS*, Vol. 35, No. 21, November 1, 2010
3. [Taira, T.](#) Domain-controlled laser ceramics toward Giant Micro-photonics *OPTICAL MATERIALS EXPRESS* Volume: 1 Issue: 5 Pages: 1040-1050.

4. S. A. Payne, L. D. Deloach, L. K. Smith, W. L. Kway, J. B. Tassano, W. F. Krupke, B. H. T. Chai, and G. Loutts // *J. Appl. Phys.* 76, 497 (1994).
5. T. S. Suzuki, Y. Sakka, and K. Kitazawa, *Adv. Eng. Mater.* 3, 490 (2001).
6. K. Inoue, K. Sassa, Y. Yokogawa, Y. Sakka, M. Okido, and S. Asai, *Mater. Trans., JIM* 44, 1133 (2003).
7. J. Akiyama, M. Hashimoto, H. Takadama, F. Nagata, Y. Yokogawa, K. Sassa, K. Iwai, and S. Asai, *Mater. Trans., JIM* 46, 203 (2005).
8. X. Mao, S. Wang, S. Shimai, and J. Guo, *J. Am. Ceram. Soc.* 91, 3431 (2008).
9. V. Đorđević, M.G. Nikolić, Ž. Antić, M. Mitrić and M.D. Dramićanin $\text{LaYO}_3\text{:Sm}^{3+}$ Nanocrystalline Phosphor: Preparation and Emission Properties. *ACTA PHYSICA POLONICA A* Vol. No. 2, P. 120 (2011).
10. C.B. Alcock, J.W. Fergus, L. Wang The electrolytic properties of LaYO_3 and LaAlO_3 doped with alkaline-earth oxides *Solid State Ionics* Volume 51, Issues 3–4, April 1992, Pages 291–295

Publications and presentations by the project:

(List publications or presentations resulting from the project to date. Please attach any new publications to the report, and acknowledge AFOSR/EOARD support in all publications.)

1. E.R. Andrievskaya, O.A. Kornienko, A.V. Sameljuk, Ali Sayir, Yoshio Sakka, Phase equilibria in the system $\text{ZrO}_2\text{-CeO}_2\text{-La}_2\text{O}_3$ // Abstract of paper 4th International Conference Materials and Technologies “SMART MATERIALS, STRUCTURES AND SYSTEMS” CIMTEC 2012. Montecatini Terme, Tuscany, Italy, June 10-14, 2012. *A1:P01*.
2. E.R. Andrievskaya, Phase relations and advanced ceramic in the systems Hafnia (Zirconia)-Yttria-Samaria // Abstracts 4th International Workshop on Directionally Solidified Eutectic Ceramics, October 14th-17th, 2012, Washington, USA. - P. 37-38.
3. E.R. Andrievskaya*, O.A. Kornienko, Ali Sayir, Phase relations in the systems based on ceria with rare earth oxides and zirconia // Abstracts 4th International Workshop on Directionally Solidified Eutectic Ceramics, October 14th-17th, 2012, Washington, USA. - P. 39.
4. Andrievskaya E.R. Phase equilibria in the Systems of zirconia, hafnia, yttria with rare-earth oxides // Abstracts International Conference «Powder metallurgy: nowadays and tomorrow», PM 2012, dedicated to 60-th Anniversary of the Frantsevich Institute for Problems in Materials Science, 27-30 November 2012, Kiev, Ukraine, 2012. – Section 1. Fundamentals of particulate materials. Modeling of technologies and properties of the particulate materials. - P. 59.